Ph.D. DISSERTATION

Thermoelectric and Charge Transport Properties in Heavily Doped Semi-Crystalline Polymers

축퇴 도핑된 반결정질 고분자의 열전 및 전하 수송 특성

August 2023

DEPARTMENT OF
ELECTRICAL AND COMPUTUER ENGINEERING
COLLEGE OF ENGINEERING
SEOUL NATIONAL UNIVERSITY

Juhyung Park

Thermoelectric and Charge Transport Properties in Heavily Doped Semi-Crystalline Polymers

축퇴 도핑된 반결정질 고분자의 열전 및 전하 수송 특성

지도교수 곽 정 훈

이 논문을 공학박사 학위논문으로 제출함

2023 년 8 월

서울대학교 대학원

전기정보 공학부

박 주 형

박주형의 공학박사 학위논문을 인준함

2023 년 8 월

위 원 장 : 홍 용 택 (인)
부위원장 : 곽 정 훈 (인)
위 원 : 이 수 연 (인)
위 원 : 강 기 훈 (인)
위 원 : 정 승 준 (인)

Abstract

Thermoelectric and Charge Transport Properties in Heavily Doped Semi-Crystalline Polymers

Juhyung Park
DEPARTMENT OF ELECTRICAL AND COMPUTER ENGINEERING
COLLEGE OF ENGINEERING
SEOUL NATIONAL UNIVERSITY

Harnessing low-grade waste heat, an inevitable byproduct of various industrial and energy conversion processes, is crucial for addressing the escalating concerns of environmental pollution and energy crises. Conjugated polymer-based thermoelectric (TE) devices offer a promising solution to this issue, as they present a sustainable and environmental-friendly approach by directly converting low-grade waste heat into electricity. Nonetheless, enhancing their TE performance remains a challenge due to the intrinsic structural and energetic disorders in these materials, which lead to the power law relationship between Seebeck coefficient (α) and electrical conductivity (σ) showing no local power factor (PF) maximum.

This thesis demonstrates that degenerately doped semi-crystalline polymers, achieved through sequential doping, can overcome the power law relationship between α–σ, achieving local PF maxima. Firstly, I demonstrate an ideal α–σ relationship where the α is inversely proportional to the σ, using two donor-acceptor type (D-A type) semi-crystalline polymers, poly[(4,4′-(bis(hexyldecylsulfanyl)methylene)cyclopenta[2,1-b:3,4-b′]dithiophene)-alt-(benzo[c][1,2,5]thiadiazole)] (PCPDTSBT) and poly[(2,5-bis(2-hexyldecyloxy)phenylene)-alt-(5,6-difluoro-4,7-di(thiophen-2-

yl)benzo[c][1,2,5]thiadiazole)] (PPDT2FBT), which were degenerately doped via sequential doping approach. This technique enables efficient modulation of the electronic structure of the polymer while preserving—or even enhancing—the highly ordered microstructure, allowing for the attainment of *PF*s nearing theoretical maxima and the observation of metallic behavior. Additionally, I revealed that the *PF* maxima of the films appear where their electronic structure transitions from non-degenerate to degenerate by thoroughly studying their structure-property relationship.

In the second part of this thesis, I successfully modulate the electronic structure of poly(3,4-ethylenedioxythiophene):poly(styrenesulfonate) (PEDOT:PSS) films, which is one of the promising TE materials among conjugated polymers, without compromising their highly ordered microstructure by introducing sequential acid-base treatments. This approach enables the fabrication of a solution-processable high-performance TE device with a *PF* of 534.5 μW m^{-1} K^{-2}, accompanied by the inverse relationship between α and σ. Furthermore, it allows the observation of the coherent charge transport characteristics such as the Hall effect, negative temperature dependency of σ, and weak localization. Through a comprehensive analysis of the structure-property relationship using various techniques, it has been demonstrated that the *PF* can be further improved by mitigating conformational disorders induced by dopants.

The innovative methodologies employed herein lay a solid groundwork for advancing the development of high-performance TE devices and deepening our understanding of the intricate structure-property relationships in conjugated polymers. The far-reaching implications of this work encompass the potential for substantial energy savings and minimized environmental footprint through the efficacious harnessing of low-grade waste heat, ultimately propelling both industry and society towards a greener and more sustainable future.

Keyword: low-grade waste heat, polymer thermoelectrics, structure-property relationship, charge transport, disorders
Student Number: 2019-37962

Table of Contents

Abstract i

Table of Contents iii

List of Figures vii

List of Tables xiii

Chapter 1. Introduction 1

1.1 Organic thermoelectrics 3

1.2 Structural and energetic disorders in conjugated polymers ... 5

1.3 Sequential molecular doping 7

1.4 Seebeck coefficient–electrical conductivity relationship 8

1.5 Outline of this thesis 10

Chapter 2. Background Theory 11

2.1 Thermoelectric effects 11

2.2 Seebeck coefficient–electrical conductivity relationship 12

2.2.1 Kang–Snyder model 13

2.2.2 Semi-localized model 14

2.3 Temperature-dependent electrical conductivity 16

2.3.1 Variable range hopping (VRH) model 16

2.3.2 Fluctuation induced tunneling (FIT) model 17

Chapter 3. Experimental Methods 19

3.1 Materials 19

3.2 Film preparation 20

3.2.1 PCPDSBT and PPDT2FBT films 20

3.2.2 PEDOT:PSS films 21
3.3 Characterization 23
3.3.1 Thermoelectric properties 23
3.3.2 Temperature-dependent electrical conductivity 24
3.3.3 Hall effect and magnetoconductance 24
3.3.4 Other characterization method 24

Chapter 4. Heavily Doped Semi-Crystalline Polymers for High Performance Thermoelectrics 26

4.1 Introduction 26
4.2 Characterization of TE properties 29
4.3 TE properties–charge transport relationships 36
4.4 Characterization of morphological properties 42
4.5 Spatial distribution of dopants in doped films 48
4.6 The *PF* maximum in the $s = 1$ system 50
4.7 Charge transport in heavily doped polymers 53
4.8 Summary 57

Chapter 5. High TE Performance in PEDOT:PSS Films with Improved Structural Connectivity 58

5.1 Introduction 58
5.2 Optimization of the TE performance 61
5.3 Analysis of the TE relationships using transport model 72
5.4 Temperature-dependent electrical characterizaions 77
5.5 Analysis of the magnetoconductance 84
5.6 Summary 92

Chapter 6. Conclusion 93

Bibliography 94

Publications **106**

한글 초록 **108**

감사의 글 **110**

List of Figures

Figure 1.1 Sources of low-grade waste heat and their potential heat-to-electricity conversion through thermoelectric generators via Seebeck effect. 1

Figure 1.2 Chemical structure of p-type conjugated polymers. Figure adapted with permission; doi:10.1016/j.progpolymsci.2022.101548 4

Figure 1.3 A schemtaic illustration of crucial microstructural attributes in conjugated polymers is presented. The mesoscale aspect of a device comprises both ordered and amorphous areas. Tie chains facilitate connectivity between ordered sections. Reprinted with permission from (*Macromol. Rapid Commun*. 2018, *39*, 1–9). Copyright (2018) John Wiley & Sons, Inc 5

Figure 1.4 Schematic illustration of doping methodologies for conjugated polymers. (a) co-processing, and (b) sequential doping 7

Figure 1.5 Relationships between TE properties of the doped polythiophene-based semiconducting polymers. Seeback coefficient and power factor as a function of σ. The dashed line represents an empirical fit of α and PF with respect to σ. Reprinted with permission from (*Adv. Energy Mater*. 2015, 5, 1401072). Copyright (2014) John Wiley & Sons, Inc . 9

Figure 2.1 Schematic illustration of Seebeck effect. 11

Figure 3.1 Cyclic voltammograms of PCPDTSBT and PPDT2FBT. The highest occupied molecular orbital (HOMO) energy levels were determined as −5.10 eV and −5.45 eV for PCPDTSBT and PPDT2FBT, respectively. 20

Figure 4.1 Molecular structure of semi crystalline polymers. (a) PCPDTSBT and (b) PPDT2FBT 29

Figure 4.2 Characterization of doped semi-crystalline polymers. UV-vis absorption spectra of the (a) PCPDTSBT–Mix, (b) PCPDTSBT–OC, and (c) PPDT2FBT–OC as a function of the $FeCl_3$ concentration, and their (e) UPS spectra as well as corresponding work functions. 30

Figure 4.3 Thermoelectric characterization of doped semi-crystalline polymers. (a) Schematic illustration of the thermoelectric device. (b) Thermoelectric properties of (c) PCPDTSBT–OC and (d) PPDT2FBT-OC, and (e) PCPDTSBT-Mix. 33

Figure 4.4 α–σ relationship of degenerately doped polymers. (a,b) α–σ relationship of the films and fits to the Kang–Snyder model..... 37

Figure 4.5 Mott–Schottky analysis for extracting carrier concentration. (a) Scheme of the MIS device structure. (b) Capacitance–voltage characteristics of the pristine PPDT2FBT and PCPDTSBT films. The inset shows the C_p^{-2}–V plot to extract the carrier concentration. (c) The carrier concentration of PCPDTSBT and PPDT2FBT calculated from the Cp^{-2}–V plot..... 37

Figure 4.6 MIS admittance spectroscopy of doped polymers. C_p–V characteristics of (a) PCPDTSBT-Mix, (b) PCPDTSBT-OC, and (c) PPDT2FBT-OC to extract the carrier concentration. 40

Figure 4.7 Two-dimensional GIWAXS patterns of doped polymers. (a) PCPDTSBT-Mix, (b) PCPDTSBT-OC, and (c) PPDT2FBT-OC at various dopant concentrations. 42

Figure 4.8 GIWAXS line-cut profiles. (a) PCPDTSBT-Mix, (b) PCPDTSBT-OC, and (c) PPDT2FBT-OC. 43

Figure 4.9 GIWAXS parameters obtained from the (010) peak position. π-π stacking distance and coherence length of the (a) PCPDTSBT-Mix, (b) PCPDTSBT-OC, and (c) PPDT2FBT-OC at various dopant

concentrations. 44
Figure 4.10 AFM height images. (a) PCPDTSBT-Mix, (b) PCPDTSBT-OC, and (c) PPDT2FBT-OC as a function of the $FeCl_3$ concentration. 47
Figure 4.11 Spatial distribution of dopants in doped films. (a) SPC histograms, (b) SPC maps, and (c) height images of PCPDTSBT-Mix, PCPDTSBT-OC, and PPDT2FBT-OC at the maximum dopant concentration. The size of all the AFM images is 5 μm × 5 μm.....48
Figure 4.12 Effect of the transport parameter *s* on *PF*. (a) The markers are the *PF*s of PCPTDTSBT-Mix, PCPDTSBT-OC, and PPDT2FBT-OC. The solid and dashed lines present the simulated PFs from the Kang–Snyder model with $s = 1$ and $s = 3$, respectively. (b) The weighted mobility from the experimental data is marked with circles. The curves are the calculated weighted mobility values (solid lines) consisting of the degenerate limit (dashed lines) and the non-degenerate limit components (dotted lines). The vertical lines across the graphs, light blue for PCPDTSBT-OC and light red for PPDT2FBT-OC, show that the *PF* maximum coincides with the area of transition from the non-degenerate regime to the degenerate regime. 51
Figure 4.13 Charge transport properties of doped polymers. (a) Temperature dependence of the electrical conductivity σ and (b) the reduced activation energy $W(T)$ of the samples at the maximum dopant concentration, and their (c) activation energy E_a and (d) the transport barrier W_γ. Inset images show the $\ln\sigma$ vs T^{-1} and $\ln\sigma_{E0}$ vs $T^{-1/2}$ plots, respectively. (e,f) Schematic images of film morphology of (e) the overcoated films and (f) the mixed films. 55
Figure 5.1 Optimization of TE performance through super-acid treatments. (a) sheet resistance and thickness, (b) σ and α, and (c) $\alpha^2\sigma$ of PEDOT:PSS-

TFSA films according to the number of treatments. 62

Figure 5.2 Effects of the acid-base treatments on the electronic structure of the films. UV–Vis–NIR absorption spectra of the pristine and PEDOT:PSS–TFSA films with different TDAE treatment time. The spectral intensity around at 620 nm, 900 nm, and 1300 nm indicates the neutral, polaron and bipolaron states in the PEDOT chains, respectively. 63

Figure 5.3 Thermoelectric and structural properties of TDAE-treated PEDOT:PSS–TFSA films. (a) Schematic illustrations of PEDOT and PSS networks in the pristine, PEDOT:PSS–TFSA, and TDAE-treated PEDOT:PSS–TFSA films. (b) Two-dimensional GIWAXS patterns of the films along with the TDAE-treatment time. (c) Illustrative structure of the TE devices and measurement. Thermoelectric performance of the PEDOT:PSS–TFSA films in terms of (d) σ, α, and (e) *PF* as a function of the TDAE-treatment time. 64

Figure 5.4 Effects of the acid-base treatments on the electronic structure of the films. (a) The SPC histogram and (b) work functions of the pristine and PEDOT:PSS–TFSA films with different TDAE treatment time. The work functions were extracted by fitting the SPC spectra using Gaussian function. 66

Figure 5.5 Effects of the acid-base treatments on the chemical structure of the films. S2p XPS spectra of the pristine and PEDOT:PSS–TFSA films with different TDAE treatment time. Two S2p peaks were observed in the regions of 162–166 eV and 167–172 eV, which are corresponding to thiophene of PEDOT and sulfonic acid of PSS. After TFSA immersion treatment, the relative peak intensity of PEDOT to PSS noticeably increase, indicating the removal of PSS from PEDOT:PSS film. 66

Figure 5.6 Morphological characteristics of the PEDOT:PSS films. 2 μm by 2 μm AFM topography and phase images of the PEDOT:PSS films. 67

Figure 5.7 Line-cut profiles obtained from 2D GIWAXS patterns of (a) q_{xy} and (b) q_z direction of the PEDOT:PSS and PEDOT:PSS–TFSA films as function of TDAE treatment time. The pristine PEDOT:PSS film showed characteristic peaks at $q \approx 0.27$ Å^{-1}, 0.51 Å^{-1}, 1.19 Å^{-1}, and 1.80 Å^{-1} at q_z direction, which are corresponding to lamellar stacking of PEDOT and PSS, amorphous halo of PSS, and π-π stacking of PEDOT [(020) planes of PEDOT], respectively. 69

Figure 5.8 Illustration of packing arrangement. Lamellar stacking of PEDOT:PSS-TFSA (left image) and of TDAE treated PEDOT:PSS-TFSA where TDAE is located between PEDOT and PSS (right image). 71

Figure 5.9 Seebeck coefficient and power factor of the TDAE-treated PEDOT:PSS–TFSA films as a function of electrical conductivity. (a) The α–σ and (b) $\alpha^2\sigma$–σ relations of the films are obtained by fitting experimental data to the SLoT and K–S models with various σ_{E0} and s. The vertical line represents the transition point at which the power law of the α–σ changes..... 73

Figure 5.10 Change in localization energy W_H as a function of TDAE de-doping time. The values of W_H of the PEDOT:PSS films were extracted by the SLoT model. When the W_H converges to zero, the transport function of SLoT model equals to the $s = 1$ case of the K–S model..... 75

Figure 5.11 Characterization of charge transport properties of PEDOT:PSS–TFSA films depending on TDAE treatment. (a) Schematic illustration of the Hall bar measurement and (b) its optical micrograph image of the device. The longitudinal (V_{xx}) and transverse voltages (V_{xy}) were recorded simultaneously by applying a constant dc current (I). (c) The

temperature-dependent σ as a function of de-doping time. The FIT model well fits the experimental data at T below the critical temperature. (d) The Hall voltage when the B field was ramped up to 8 T and then down to −8 T at various temperatures from 20 K to 300 K. The scale bar represents 1 μV. 77

Figure 5.12 Zabrodskii plot of the PEDOT:PSS films. The slope of the fit line equals to the value of $-1/m$, which gives the information of the dimension m of the VRH mechanism. 79

Figure 5.13 Hall effect measurements for the PEDOT:PSS films. (a-f) The extracted Hall voltages of the TDAE-dedoped PEDOT:PSS–TFSA films for 3, 5, 7, 10, 20, and 30 min, respectively, when B field was ramped up to 8 T and down to −8 T at various temperatures from 20 K to 300 K. 80

Figure 5.14 Characterization of charge transport properties of PEDOT:PSS–TFSA films depending on TDAE treatment. (a) The transport coefficient σ_{E0} of the films when $s = 1$. (b) The tunneling barrier T_1 and Hall carrier mobility μ_H as a function of the TDAE de-doping time. 81

Figure 5.15 Electrical parameters of PEDOT:PSS films extracted from Hall effect measurement. (a) Temperature-dependent electrical mobility μ_H and (b) carrier concentration $(eR_H)^{-1}$. 82

Figure 5.16 Weak localization in the magnetoconductance of the PEDOT:PSS–TFSA films as a function of the TDAE treatment time. Effect of B field applied perpendicular to the substrate on differential conductance ($\Delta G = G(B) - G(0)$) of the TDAE-treated PEDOT:PSS–TFSA films at a various temperature; (a) 0 min, (b) 7 min, and (c) 30 min, respectively. 84

Figure 5.17 Weak localization in the magnetoconductance of the TDAE-treated

PEDOT:PSS–TFSA films. Effect of B field applied perpendicular to the substrate on differential conductance ($\Delta G = G(B) - G(0)$) of the TDAE-treated PEDOT:PSS–TFSA films at a various temperature; (a) 3 min, (b) 5 min, (c) 10 min, and (d) 20 min, respectively. 85

Figure 5.18 Inelastic scattering characteristics of the PEDOT:PSS–TFSA films as a function of TDAE treatment time. Temperature-dependent (a) characteristic field B_φ, (b) phase-breaking time τ_φ, and (c) inelastic scattering length λ_φ. The values of B_φ were extracted by fitting the differential conductance ΔG versus B of the PEDOT:PSS films using 2D HLN model. The scattering parameter p was determined by interpreting the T dependency of the phase-breaking time τ_φ. 87

Figure 5.19 Scattering parameter of the PEDOT:PSS–TFSA films as a function of TDAE treatment time. (a) Scattering parameter p extracted by fitting the τ–T relationship. The electron-electron scattering mechanism was observed for all the films. (b) inelastic coherence length λ_φ as a function of de-doping time. 87

Figure 5.20 Sources for the increased density of scattering centers. (a) Normalized Raman spectra, and (b) N1s XPS spectra of the PEDOT:PSS–TFSA films with different TDAE treatment time. The peaks corresponds to the protonated amines (401.6 eV) were observed for the pristine and PEDOT:PSS–TFSA film. As the TDAE treatment time increases, the peaks shifted to lower binding energy. When the TDAE treatment time exceeds 7 min, the peaks at 398.3 eV, which corresponds to the neutral amines, abruptly increases (marked by dotted rectangular). 88

Figure 5.21 C-AFM images of the PEDOT:PSS–TFSA films as a function of TDAE treatment time. The electrical concentration between PEDOT domains abruptly degrades as the TDAE treatment time exceeds 7 min.

.....91

List of Tables

Table 4.1 Thermoelectric properties of various doped conducting polymers. 34

Table 4.2 Thermoelectric properties of PCPDTSBT-OC, PCPDTSBT-Mix, and PPDT2FBT-OC. 35

Table 4.3 Carrier concentrations of PCPDTSBT-OC and PPDT2FBT-OC derived from admittance spectroscopy. 41

Table 4.4 Packing parameters derived from GIWAXS. 45

Table 5.1 Information on the diffraction peak parameters derived from GIWAXS data. The values of crystal coherence length were calculated using the Scherrer formula. 70

Table 5.2 SLoT modelling and material parameters for the $\eta(c)$ and $W_H(c)$ relationships. 75

Table 5.3 Calculated σ_0, T_0, and T_1 of PEDOT:PSS–TFSA films as a function of TDAE de-doping time. 83

Chapter 1. Introduction

The escalating demands for sustainable and efficient energy conversion techniques are critical in the face of increasing energy consumption and environmental concerns[1]. Exploiting waste heat, an inevitable byproduct of numerous industrial and energy conversion processes (e.g. power plants, and transportation) has surfaced as a viable solution to tackle these challenges[2]. Waste heat is defined as the unconverted or untapped thermal energy, resulting in energy losses and inefficiencies. In contemporary industrial settings, over 60% of the total energy is lost as waste heat across diverse manufacturing and processing facilities (**Figure 1.1,** left)[3]. While high-temperature waste heat can be readily captured and repurposed, low-temperature waste heat (primarily below 200°C) presents difficulties for recovery and reuse through conventional energy conversion technologies such as steam turbines[4] and organic Rankin cycles[5] due to its inferior quality and energy density. Such low-grade waste heat, accounts for 45% of the total waste heat produced[6]. In addition, countless real-life low-grade waste heat sources, such as body heat[7] and microelectronic devices, are being wasted, emphasizing the need for effective waste heat recovery solutions.

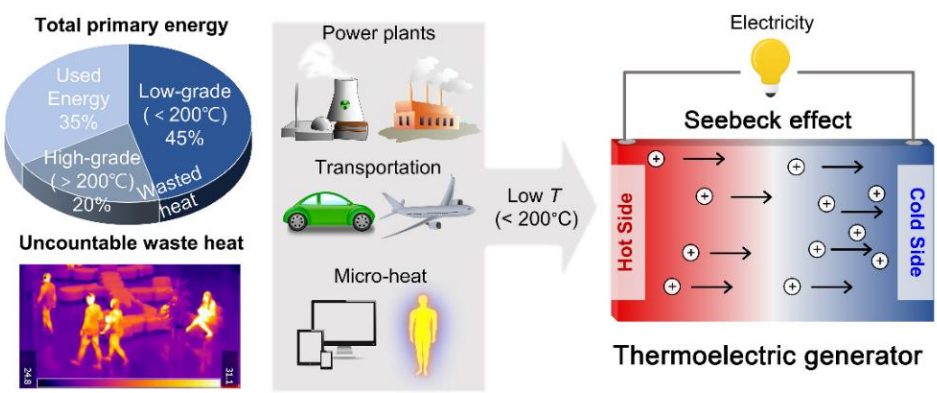

Figure 1.1 Sources of low-grade waste heat and their potential heat-to-electricity conversion through thermoelectric generators via Seebeck effect.

Thermoelectrics (TE) has emerged as a promising technology for waste heat recovery, offering the potential to convert waste heat directly into electrical energy via the Seebeck effect (**Figure 1.1**, right)[8]. Thermoelectric generators (TEGs), are solid-state devices that exploit this phenomenon to transform waste heat into useful electricity, thereby enhancing the overall energy efficiency of systems and reducing greenhouse gas emissions. Compared to other energy harvesting techniques[9], TE devices exhibit several advantageous features, such as compact size, scalability, absence of moving parts, and low maintenance requirements. These properties make TE devices particularly suitable for a wide range of applications, including wearable devices that can harvest body heat for energy supply[10], small-scale electronic devices[11] to large industrial processes[12]. Historically, inorganic semiconductors based on bismuth telluride have been widely used in TE devices due to their high efficiency[13, 14]. However, the high cost and scarcity of tellurium, a key element in these materials, along with their toxicity, heaviness, and brittleness, which make them less suitable for use with heat sources like the human body, have necessitated the exploration of alternative materials that can provide comparable performance at a lower cost and with more abundant resources[15]. To overcome this challenge, researchers have focused on developing novel materials[16] with optimized properties, such as carbon-based materials[17-19], organic materials[20] and organic-inorganic hybrids[21, 22]. These efforts have led to significant improvements in *ZT* values and the discovery of new materials with promising thermoelectric performance.

1.1 Organic thermoelectrics

Organic materials, particularly conjugated polymers, have recently emerged as a promising material for TE applications[20, 23-25]. These polymers are a class of organic materials defined by an extended π-conjugated system, which enables efficient charge transport due to electron delocalization along the polymer backbone[26]. Various classes of p-type conjugated polymers[27] have shown promise for organic TEs, including widely investigated poly(3,4-ethylenedioxythiophene) (PEDOT)-based polymers[28-44], classic semicrystalline polythiophene-based polymers like poly(3-heylthiophene) (P3HT)[45-47], and poly(2,5-bis(thiophen-2-yl)thieno-[3,2-b]thiophene) (PBTTT)[48], as well as donor–acceptor (D–A) copolymers such as benzothiadiazole (BT)-based copolymers[49] and diketopyrrolopyrrole (DPP)-based copolymers[50] (**Figure 1.2**). These materials offer several advantages over their inorganic counterparts, such as low-cost production[51], lightweight nature, flexibility[52], solution-processability[42, 53], and biocompatibility[43], making them highly attractive for various energy conversion applications, including waste heat recovery. Their unique features further enable the fabrication of conformable, lightweight devices suitable for wearable[54] and implantable applications[43]. Moreover, conjugated polymers have tunable electrical properties, allowing for optimization of their TE performance through molecular engineering and doping strategies[55]. Additionally, these materials exhibit intrinsically low thermal conductivity, which contributes two improved TE efficiency, which is generally evaluated by a dimensionless figure of merit, $ZT = \alpha^2\sigma T/\kappa$, where α, σ, T and κ are the Seebeck coefficient, electrical conductivity, absolute temperature, and thermal conductivity, respectively. Based on these enormous potentials conjugated polymers, multidisciplinary efforts, including advancements in material synthesis[56, 57], doping engineering[47, 58-60], device

engineering and device physics[48], are accelerating the development of polymer-based TE devices, leading to continuous progress in this promising field. A major challenge lies in the relatively lower TE performance, particularly power factor (*PF*) (represented as $\alpha^2\sigma$), of the conjugated polymers compared to inorganic counterparts, which necessitates further improvements for various applications such as Internet of Things sensors or wearable energy harvesters.

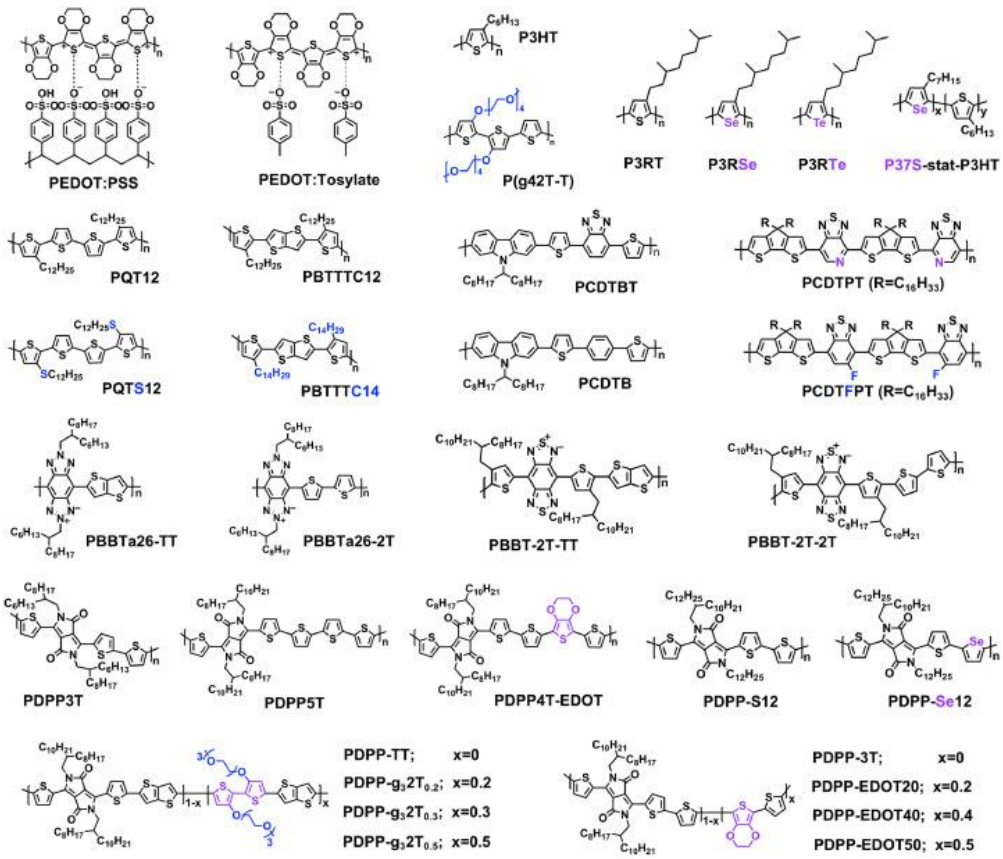

Figure 1.2 Chemical structure of p-type conjugated polymers. Figure adapted with permission; doi:10.1016/j.progpolymsci.2022.101548

1.2 Structural and energetic disorders in conjugated polymers

The TE performance (*i.e.*, σ, α and κ) of conjugated polymers are largely linked to their structural and energetic disorders, as they influence phonon and electronic transport[61]. Structural disorders in conjugated polymers refer to the irregularities in the arrangement and organization of polymer chains, resulting from factors such as chain defects, polydispersity in molecular weight, or the kinetics of solidification from solution or melt states[46, 62-64]. These irregularities can lead to the formation of amorphous regions with different electronic properties compared to more ordered, crystalline regions (**Figure 1.3**). Energetic disorder, on the other hand, is related to the variations in energy levels within the material. It can arise from conformational changes in the polymer backbone or disruptions in intermolecular interactions, which can affect the electronic levels and, consequently, the electronic properties of the material. The bandgap of conjugated polymers, which originates from the interaction between the π and π^* orbitals of the repeat units along the polymer chain, can be influenced by these energetic variations[24, 65-68].

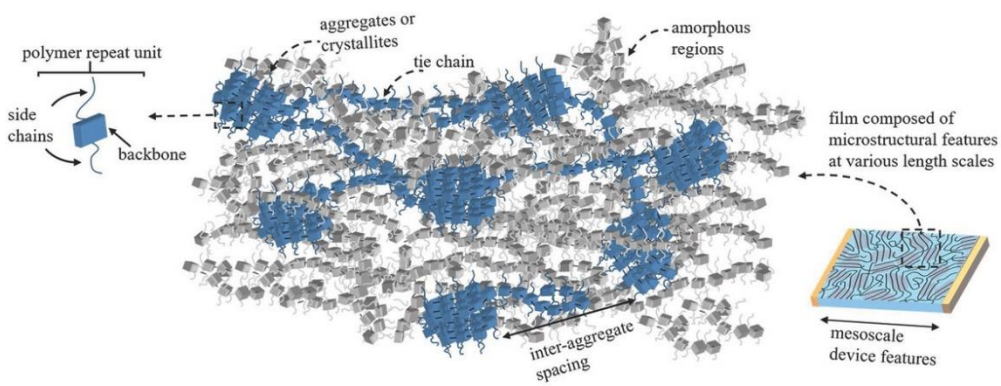

Figure 1.3 A schemtaic illustration of crucial microstructural attributes in conjugated polymers is presented. The mesoscale aspect of a device comprises both ordered and amorphous areas. Tie chains facilitate connectivity between ordered sections. Reprinted with permission from (*Macromol. Rapid Commun*. 2018, *39*, 1–9). Copyright (2018) John Wiley & Sons, Inc

Molecular doping, an inevitable process for controlling electrical and TE properties, can further exacerbate the structural and energetic disorders in conjugated polymers by introducing electron donor (n-doping) or electron acceptor (p-doping) molecules. Unlike atomic substitutional doping in inorganic semiconductors, molecular doping in conjugated polymers promotes polaron formation—localized charge carriers accompanied by lattice distortions—through charge transfer or redox reactions between polymer and dopant molecules, which can disrupt the chain conformation, increasing structural disorder[48, 69, 70]. Furthermore, the larger size of dopant molecules compared to single atoms in inorganic semiconductors can contribute to more pronounced structural alterations by disrupting the regular chain packing and π-π stacking interactions in the polymer matrix[62]. These dopant-induced structural perturbations can concomitantly give rise to energetic disorders within the materials, leading to a substantial broadening of the electronic density of states (DOS)[64]. This may result in the formation of trap states that adversely impact TE and charge transport properties, such as charge carrier mobility (μ). Therefore, it is essential to mitigate structural perturbations during the doping process to maximize the power factor *PF*. In the following section, one such method, sequential doping, which enables to efficiently control the electronic structure of the polymers while preserving their microstructure or even enhancing it, will be introduced.

1.3 Sequential molecular doping

Doping methodologies significantly impact the structural order of doped conjugated polymers. While co-processing, which involves depositing a mixed solution of polymer and dopant, is widely adopted for its simplicity (**Figure 1.4**, left), it often leads to aggregate formation and reduced electrical conductivity due to solubility limitations[58]. Sequential doping, on the other hand, deposits dopant onto a pre-formed polymer film, resulting in enhanced film morphology and more efficient control of doping levels, thus optimizing electronic properties (**Figure 1.4**, right). For instance, Kang et al. demonstrated successful doping of PBTTT using solid-state diffusion of F4TCNQ in crystallized polymer films, maintaining the local crystalline π–π stacked structure and achieving electrical conductivity over 200 times greater (~250 S cm^{-1}) than the solution co-deposition method[70]. Various sequential doping methods including solid-state diffusion[70], ion-exchange[71], and double doping[72] have recently been developed, which facilitates the modulation of electrical properties in conjugated polymers while preserving their structural order, serving as a key strategy to enhance thermoelectric device performance.

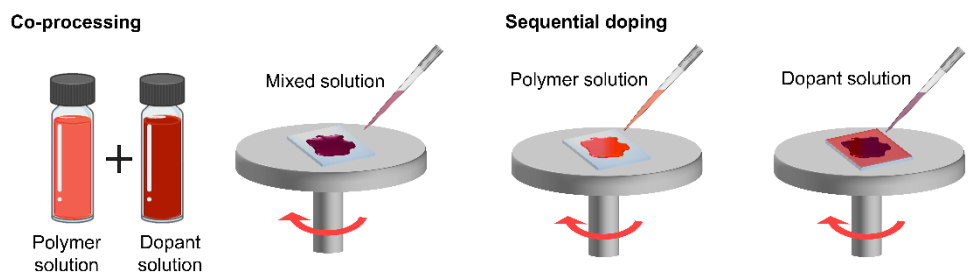

Figure 1.4 Schematic illustration of doping methodologies for conjugated polymers. (a) co-processing, and (b) sequential doping

1.4 Seebeck coefficient–electrical conductivity relationship

The TE performance of a material is closely tied to its charge carrier concentration[8]. However, accurately measuring *n* in semiconducting polymers can be challenging due to the disordered nature and lower σ of the polymer films, which make conventional measurement methods like Hall effect measurements[73] unsuitable for various polymers[63, 64]. Therefore, deciphering the empirical TE relations (*i.e.*, relations of *PF*–σ and α–σ) as a function of doping becomes an important challenge to mitigate above difficulties[68], which allow to establish another strategy to maximize *PF* and provides insight into the charge transport of doped conjugated polymers having significant structural and energetic disorder[74-77].

For most thiophene-based semiconducting polymers (e.g. P3HT, PBTTT, P2TDC$_{17}$-FT4), an empirical power law relation of $\alpha = (k_B/e)(\sigma/\sigma_0)^{-1/s}$, with $s = 3$ or 4, was observed over a wide range of σ where the doping level varies substantially, where σ_0, and s are fitting parameters[62, 68] (**Figure 1.5**). Such a power law leads to a consistent increase in *PF* as a function of σ with no local maximum, which contrasts the typical behavior of inorganic semiconductor that usually shows *PF* maximum where its electronic structure transitions from non-degenerate to degenerate[8]. To understand the physical origin behind this empirical behavior observed in the α–σ relationship in various doped polymers, numerous attempts have been made, and a recent phenomenological model successfully describes the behavior by incorporating an energy-dependent transport function[76]. It has been revealed that the power law relations stem from the disordered nature of the films, where charge transport is heavily influenced by the structural and energetic disorders[78, 79].

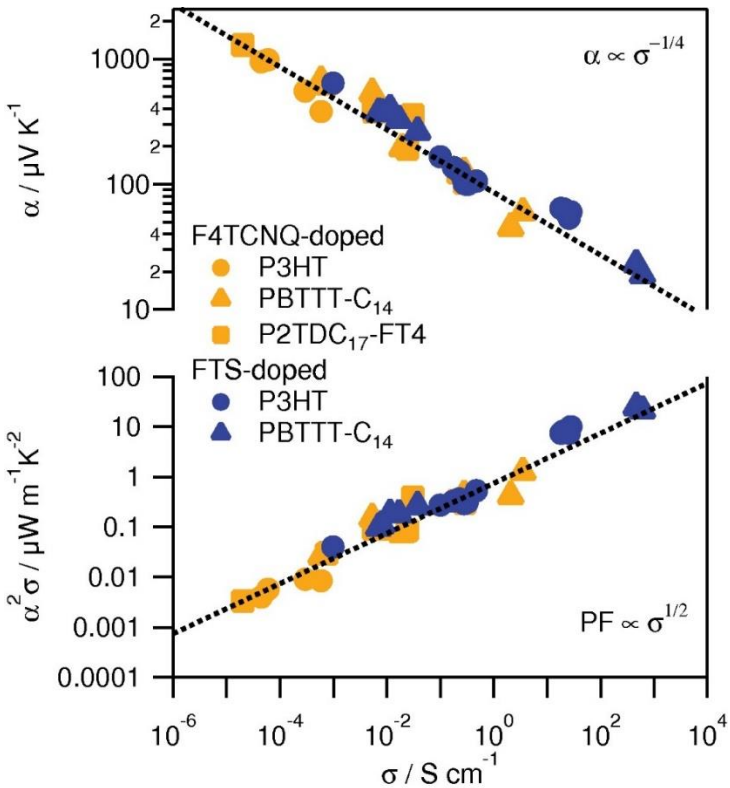

Figure 1.5 Relationships between TE properties of the doped polythiophene-based semiconducting polymers. Seeback coefficient and power factor as a function of σ. The dashed line represents an empirical fit of α and *PF* with respect to σ. Reprinted with permission from (*Adv. Energy Mater*. 2015, 5, 1401072). Copyright (2014) John Wiley & Sons, Inc

One exceptional case deviating from the above-mentioned power law is the PEDOT derivatives, which demonstrates one of the highest σ and *PF* among conjugated polymers[28-38, 40-43, 57, 80, 81]. Unlike other doped semiconducting polymers, the PEDOT system evidently demonstrate *PF* maximum points, accompanied by the α–σ relation with $s = 1$ characteristic[44, 74, 82]. The different s in PEDOT implies the different charge transport mechanism in this system, and this behavior is known to be the consequence of the disorder-free charge transport originating from both the long-range connectivity between PEDOT domains and

degenerate states[57]. Developing the doped polymers behaving like PEDOT and understanding their structural-property relationship is important for realizing the high-performance polymer-based TE devices, which is the aim of this thesis.

1.5 Outline of this thesis

This thesis consists of six chapters. The introductory part, **Chapter 1**, describes the necessity of polymer thermoelectrics, the theoretical basis, and motivation for this research**. Chapter 2** discusses the theoretical background of the thesis, including thermoelectric effects, the relationship between Seebeck coefficient and electrical conductivity, and the charge transport models. In **Chapter 3**, experimental methods for material preparation, device fabrication, and characterization are presented. **Chapter 4** introduces various strategies for achieving degenerately doped semi-crystalline polymers with ideal Seebeck coefficients and electrical conductivity that exhibit the local power factor maximum, and thoroughly analyzes the origins of their high performance. **Chapter 5**, covers the strategies for maximizing the thermoelectric performance of PEDOT:PSS, one of the most promising solution-processable TE materials, and considers their current limitations and potential. **Chapter 6** concludes with the results presented above and discusses the implications of this thesis.

Chapter 2. Background Theory

2.1 Thermoelectric effects

The TE effect encompasses a set of phenomena that enable the direct conversion of thermal energy into electrical energy, and vice versa, through the exploitation of temperature gradients in specific materials. This effect relies on three fundamental principles: the Seebeck effect, the Peltier effect, and the Thomson effect.

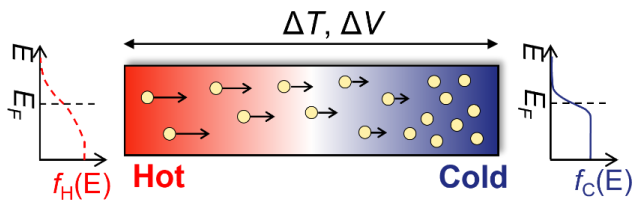

Figure 2.1 Schematic illustration of Seebeck effect.

In the Seebeck effect, a voltage difference (ΔV) is generated when a temperature difference (ΔT) exists between two junctions of dissimilar conductive materials (**Figure 2.1**). This effect can be mathematically represented as $\Delta V = \alpha \Delta T$, where α is the Seebeck coefficient. The Peltier effect is the inverse phenomenon of the Seebeck effect where an electric current I induces heat transfer at the junction of two dissimilar conductive materials. The Peltier effect can be described by the following equation, $Q = \Pi I$, where Q represents the heat absorbed or released, Π denotes the Peltier coefficient. The Thomson effect takes place when ΔT is applied along a conductive material, leading to the absorption or release of heat, which is expressed as, $Q = KI\Delta T$, where K represents the Thomson coefficient. The Π, α and K are inter-related through the second Thomson law, given by $\Pi = T\alpha$ and, $K = T(d\alpha/dT)$, along with the Onsager reciprocal relations, assuming time-reversal symmetry.

2.2 Seebeck coefficient–electrical conductivity relationship

As described above, the Seebeck coefficient of a material usually exhibits an inverse relationship with its electrical conductivity. σ and α can be generally characterized by the transport function $\sigma_E(E)$ describing the capability for electrical conduction at each energy level in the units of σ[83]. By solving the Boltzmann transport equations, the α and σ is expressed with $\sigma_E(E)$ as the following equations:

$$\sigma = \int \sigma_E \left(-\frac{\partial f}{\partial E}\right) dE \tag{1}$$

$$\alpha = \frac{k_B}{q} \int \frac{(E - E_F)}{k_B T} \frac{\sigma_E}{\sigma} \left(-\frac{\partial f}{\partial E}\right) dE \tag{2}$$

Here, f is the Fermi-Dirac distribution function, which is expressed as $f = 1/[1+\exp(E-E_F)/(k_BT)]$, where q, k_B and E_F are a unit charge, Boltzmann constant, and chemical potential of the polymer, respectively. The form of transport function determines the mechanism of charge transport, and various charge transport models can be interpreted using this functional form. Here, two charge transport models (*i.e.*, Kang–Snyder model, and Semi-localized models) that have been widely used for interpreting the α–σ relations of the conjugated polymers are introduced[74, 76].

2.2.1 Kang–Snyder model

The Kang–Snyder model suggests a novel form of transport function, which has power law energy dependency with energy E above the transport edge E_t,

$$\sigma_E(E,T) = \begin{cases} 0\ (E < E_t) \\ \sigma_{E0} \times \left(\frac{E - E_t}{k_B T}\right)^s\ (E \geq E_t) \end{cases} \quad (3)$$

where $\sigma_{E0}(T)$ and s is the transport coefficient, and transport parameter, respectively. The proposed model incorporates a transport edge to characterize charge transport in conducting polymers across a wide energy spectrum, ranging from nearly insulating polymers ($E << E_t$) to heavily doped polymers ($E >> E_t$). The transport edge concept is analogous to a band-edge in crystalline semiconductors, where carriers with $E < E_t$ are fully localized and do not contribute to transport[69]. As a result, if the Fermi level (E_F) is less than the transport edge (E_t), carriers must be thermally excited to participate in transport, with their distribution following the Fermi-Dirac distribution. By replacing the transport function $\sigma_E(E)$ (Eq. 1 and 2) with Eq. 3, the simplified form of σ and α can be obtained:

$$\sigma = \sigma_{E0}(T) \times sF_{s-1}(\eta) \quad (4)$$

$$\alpha = \frac{k_B}{q}\left[\frac{(s+1)F_s(\eta)}{sF_{s-1}(\eta)} - \eta\right] \quad (5)$$

Here, $F_i(\eta)$ is non-normalized complete Fermi-Dirac integral, and $\eta = (E_F - E_t)/(k_B T)$ is the reduced chemical potential which is related to the doping level. The above equations (Eq. 4, 5) enable us to determine σ_{E0}, s and η using experimentally obtained σ and α.

The K–S model has been widely adopted to investigate the thermoelectric response of the doped polymers. One of the great advantages of this model is that it can predict the intrinsic limit of thermoelectric performance that polymers can achieve. This can be enabled by the newly designed transport function, which is

determined to unique value while separating from its dependency on chemical potential. The transport function of the K–S model (Eq. 3) consists of two essential fitting parameters σ_{E0} and s, which captures the temperature and energy dependency of the charge carriers respectively. The first term, $\sigma_{E0}(T)$ represents the intrinsic mobility of the polymers, which is correlated to both thermal activation energy between conductive domains W_γ and connectivity γ:

$$\sigma_{E0}(T) \propto \left[-\left(\frac{W_\gamma}{k_B T}\right)^\gamma\right] \tag{6}$$

Kang and Snyder suggest that finding a constant W_γ can elucidate the fundamental aspect of transport mechanism of the polymers (γ = 1/2 for most conducting polymers), because this value depends on the morphology and structural connectivity of the polymers while separated from its dependence on chemical potential E_F. This feature of W_γ distinguishes the K–S model from commonly used hopping models, which enables to describe the thermally activated behavior of the polymers in terms of percolation across a network of conductive domains rather than the trapping mechanism by localized states within conductive domains[84].

The second term, transport parameter s captures the energy dependency of the charge carriers, which is an exponent that determines the transport mechanism of the system. This parameter well distinguishes the PEDOT-based materials (s = 1), showing metal-like transport, from the most doped semiconducting polymers (s = 3) showing variable range hopping transport (11, 26). It has been demonstrated that the s = 1 polymers have much higher σ_{E0} (typically greater than 10 S cm^{-1}) than that of the s = 3 polymers (0.001 S cm^{-1} to 0.1 S cm^{-1}), indicating that they have an efficient percolation network between conductive domains. It has been known that the value of s is be determined from the microscopic features related to the scattering mechanism such as carrier relaxation time, velocity, and local density of states [75]. The relationship between scattering mechanism and transport parameter s is well derived from the works of Kang and Snyder. Briefly, in case of inorganic

semiconductors, they suggested that the acoustic phonon scattering is dominant for the s = 1 materials, and the ionized impurity scattering is dominant for the s = 3 materials.

2.2.2 Semi-localized model

Recently, Yee et al. presented the semi-localized (SLoT) transport model based on the Boltzmann transport formalisms that modifies the transport function of the K-S model [74]. They mentioned that the K−S model is difficult to capture the localized to delocalized transition of the polymers due to the assumption that the $\sigma_{E0}(T)$ is determined to be unique for a given materials. In addition, the s = 3 fit is inappropriate for describing the electronic bandwidth of the polymers. The SLoT model was designed to resolve these two deficiencies, which is capturing the transition in transport behavior in semiconducting polymers as a function of carrier concentration ratio c, and accurately fit the α–σ behaviors of the doped polymers at all doping levels. The transport function of SLoT model is expressed as:

$$\sigma_E(E,T,c) = \begin{cases} 0\ (E < E_t) \\ \sigma_0 \exp\left(-\dfrac{W_H(c)}{k_B T}\right) \times \left(\dfrac{E - E_t}{k_B T}\right)\ (E \geq E_t) \end{cases} \tag{7}$$

Here, W_H is the localization energy that is related to the spatial and electrostatic effects. The difference from the transport function of the K–S model is that the additional term of $\sigma_0\exp(-W_H(c)/k_BT)$, which represents Arrhenius-like hopping contribution of the charge carriers is defined, and the transport parameter s is fixed to one. As the carrier concentration ratio c becomes larger than the c_d (*i.e.*, the carrier ratios to achieve delocalized transport), the W_H converges to 0, which results in the transport function of the SLoT model equals to that of the s = 1 case in K–S model. As the carrier concentration ratio becomes less than the c_d, W_H (*i.e.,* hopping-like contributions) increases, and the transport function decreases, deviating from the s =

1 fit of the K-S model.

2.3 Temperature-dependent electrical conductivity

Temperature-dependent electrical conductivity $\sigma(T)$ is a crucial property of materials that reflects how their ability to conduct electric charge varies with changes in temperature. In most conjugated polymers, the σ is influenced by the thermally activated motion of charge carriers, such as electrons and holes, within the polymer structure[73, 77, 85]. The $\sigma(T)$ can provide valuable insights into the underlying mechanisms governing charge transport mechanism. Several charge transport models for interpreting the $\sigma(T)$ are introduced below.

2.3.1 Variable range hopping (VRH) model

The variable range hopping (VRH) model is a fundamental concept in condensed matter physics that helps understand the transport properties of disordered materials[86]. Developed by N.F. Mott in the 1960s, it addressed the limitations of the classical Drude model in explaining the temperature dependence of conductivity in disordered systems. The VRH model takes into account the quantum mechanical nature of electrons and their interactions with the disordered environment, leading to the phenomenon of localization, where electrons can be trapped in localized states. Localized electrons can still contribute to σ via a thermally activated hopping process between localized states. The VRH model consists of two main regimes: the Mott regime, where electron-electron interactions are negligible and conductivity is governed by temperature and the density of localized states[86], and the Efros-Shklovskii regime, where electron-electron interactions play a significant role and lead to the formation of a soft Coulomb gap in the density of states[70]. It is essential to note that the equations of VRH models are dependent on the dimensionality of the

system under consideration. For the Mott regime, the temperature dependence of σ can be expressed as $\sigma(T) \propto \exp[-(T_0/T)^{1/(m+1)}]$, where m represents the dimensionality of the system. While in the Efros-Shklovskii regime, it is described by $\sigma(T) \propto \exp[-(T_0/T)^{1/2}]$. These mathematical expressions emphasize the distinctive roles of temperature, electron-electron interactions, and system dimensionality in determining the hopping behavior and the resulting conductivity in disordered materials.

2.3.2 Fluctuation induced tunneling (FIT) model

The Fluctuation Induced Tunneling (FIT) model is a theoretical framework in condensed matter physics that describes charge carrier transport in disordered semiconducting materials[87]. Introduced by Sheng in 1980, the model addresses certain limitations of the VRH model and provides a more comprehensive understanding of the transport mechanisms in these materials.

In the FIT model, charge carrier transport primarily takes place through transfers between large conducting segments[88], rather than hopping between individual localized states, as described in the VRH model. These conducting segments are separated by insulating barriers, and the contact gap between them forms an effective tunneling barrier with an associated capacitance. The model takes into account the temperature dependence of σ, with carriers being thermally activated and moving from one conducting segment to another by tunneling through the insulating barriers. This tunneling process is distinct from the quantum mechanical phenomenon of tunneling and is influenced by local fluctuations in the material structure and potential landscape. The temperature-dependent electrical conductivity in the FIT model is given by the equation: $\sigma(T) \propto \exp[-T_1/(T+T_0)]$. Here, T_1 is the temperature below which conduction is primarily governed by tunneling through the

barrier, while T_0 represents the temperature above which thermally activated conduction across the barrier begins to take place[22].

Chapter 3. Experimental Methods

3.1 Materials

PCPDTSBT (M_n= 26 kDa, dispersity = 2.8) and PPDT2FBT (M_n= 28 kDa, dispersity = 2.2) were synthesized according to a previously reported procedure.[18, 32] Briefly, PCPDTSBT was synthesized via microwave-assisted Stille cross-coupling of 2,6-bis(trimethylstannyl)-4,4′-(bis(hexyldecylsulfanyl)methylene)cyclopenta[2,1-b:3,4-b′]dithiophene and 4,7-dibromobenzo[c][1,2,5]thiadiazole using $Pd_2(dba)_3$ as a catalyst in toluene. PPDT2FBT was also synthesized via Stille coupling with $Pd_2(dba)_3$ as a catalyst in chlorobenzene using a microwave reactor. The number-average molecular weight (M_n) was measured to be 26 kDa (polydispersity index, PDI = 2.8) and 28 kDa (PDI = 2.2) for PCPDTSBT and PPDT2FBT, respectively. Cyclic voltammograms of the polymers are shown in **Figure 3**.1 [EMIM][TFSI] (TCI Chemicals), PVDF-HFP, $FeCl_3$ (Sigma-Aldrich) PEDOT:PSS aqueous solution (Clevios PH 1000, Heraeus), TFSA (TCI chemicals), methanol and TDAE (Sigma-Aldrich) were purchased and used as received.

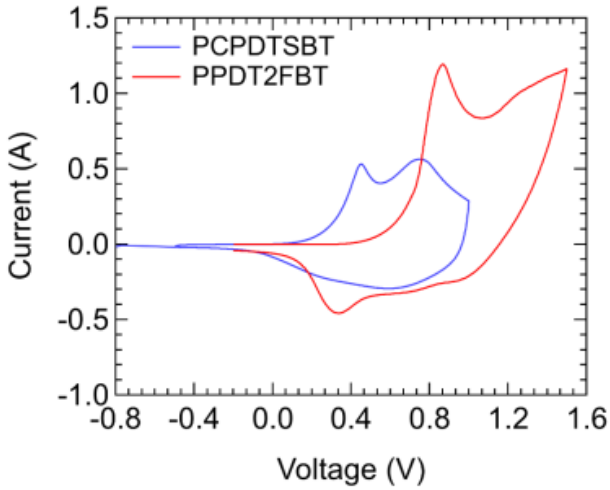

Figure 3.1 Cyclic voltammograms of PCPDTSBT and PPDT2FBT. The highest occupied molecular orbital (HOMO) energy levels were determined as −5.10 eV and −5.45 eV for PCPDTSBT and PPDT2FBT, respectively.

3.2 Film preparation

All substrates (*i.e.*, bare glass, ITO-coated glass, and Si/SiO_2 wafers) were cleaned by sonication in deionized water, acetone, and isopropyl alcohol sequentially for 15 min, followed by drying in a vacuum oven for 12 h.

3.2.1 PCPDSBT and PPDT2FBT films

For the overcoated films, PCPDTSBT and PPDT2FBT were first spin-coated on top of the precleaned substrates from a solution of 8 mg/mL in chloroform at 2000 rpm for 40 s. Then, the films were doped with various concentrations of $FeCl_3$ solution, which was sequentially spin-coated (at 2500 rpm for 40 s) on top of the dried polymer film. The thickness of the prepared films was in the range of 100–

120 nm. Samples doped by the mixing method were prepared by spin-coating the mixed solution of PCPDTSBT and $FeCl_3$ (3–45 mol%) at 2000 rpm for 40 s. The films have a thickness in the range of 60–80 nm. For thermoelectric and cryogenic measurements, Au electrodes were deposited onto the films by thermal evaporation under high vacuum conditions (~3×10^{-7} torr) with a deposition rate of 1.0 Å s^{-1} through a patterned shadow mask. For the MIS devices, an ion-gel solution was prepared by following the previously reported method, and it was spin-coated onto the patterend ITO substrate, resulting in a 150–200 nm of the insulator layer followed by annealing at 140 °C for 6 h. After spin-coating the active layer, the Au electrodes were deposited to form a cross-sectional area of 1.4 × 1.4 mm^2.

3.2.2 PEDOT:PSS films

After UV–ozone surface treatment, a PEDOT:PSS film was deposited by spin-coating at 2300 rpm for 20 s, and then annealed at 100 °C for 10 min. The second PEDOT:PSS layer was sequentially formed under the same conditions, resulting in a total thickness of 50 nm. For the acid treatment, the pristine PEDOT:PSS film was immersed in a TFSA bath for 1 min. After that, the film was immediately rinsed with methanol to remove residual TFSA, followed by annealing at 150 ℃ for 5 min. This procedure was repeated several times to optimize electrical properties. For the base treatment, the as-prepared sample was placed in a pre-heated (100 ℃), home-built vacuum chamber filled with TDAE vapor. The reduction level was controlled by changing the treatment time. To measure the TE properties, Au electrodes (70 nm) were deposited on the films by thermal evaporation under a high vacuum (~3×10^{-7} torr) with a deposition rate of 1.0 Å s^{-1} through a patterned shadow mask. Two

electrodes (17 mm × 8 mm) for the hot and cold sides were separated by 2 mm. Magnetotransport measurements were conducted using a Hall bar architecture, where the conductive PEDOT:PSS layers were patterned in order to accurately measure local potential of probes. The fabrication process for the Hall bars was as follows: A 0.7 mm-thick SiO2 substrate was cleaned by a sonication cleaning processes in deionized water, acetone, and isopropanol. Electrodes were then lithographically formed via a standard lift off process. The electrode consisting of titanium (Ti, 7 nm) and gold (Au, 70 nm) were evaporated through e-gun evaporator at the base pressure of 5×10−6 torr with a rate of 1.0 Å s^{-1}. Channel length (L) and width (W) were 240 μm and 60 μm. Four probes were mounted in between source and drain electrodes, where the distance between two longitudinal probes along the channel length (defined as L*) was designed to be 110 μm. The width of the probe was 15 μm. After completing the electrodes, the PEDOT:PSS layer was spin-coated onto the SiO2 substrates, acid and base treatment were conducted as discussed in the manuscript. Then, parylene-C (1 μm) was then deposited onto the PEDOT:PSS films using parylene coater (PDS2010), which protects the active layer from the subsequent processing steps. Finally, the photolithography and oxygen plasma etching (150 W for 5 mins) were performed to pattern the active layer into the precise hall bar geometry. The second photoresist layer and parylene films were remained as a protection layer for the active channel. All processes were carried out under cleanroom conditions with controlled humidity and temperature. For the magnetotransport measurements using physical property measurement system (PPMS), the ball bonder was used for wiring the hall bar device and the PPMS puck.

3.3 Characterization

3.3.1 Thermoelectric properties

The electrical conductivity was determined from the current–voltage characteristics obtained by the linear four-point probe method with a Keithley 2634B source meter. Thermoelectric properties were obtained using a home-made stage consisting of the two Peltier modules controlled using a Keithley 2200 power supply and a Keithley 2601B source meter. Two individual T-type thermocouples were used to detect the temperature of the hot and cold sides of the film. The generated thermovoltage was measured using a Keithley 2182A nanovoltmeter. The temperature gradient ranged from 1 K to 5 K and the mean temperature was fixed at 300 K. The Seebeck coefficients were extracted by linear fitting of the thermovoltage–temperature difference data points.

3.3.2 Temperature-dependent electrical conductivity

The temperature-dependent electrical conductivity was measured using a four-point probe method with a cryostat by varying the temperature from 20 K to 330 K with a commercial proportional-integral-derivative temperature controller (model 331 Cryogenic Temperature Controller, Lakeshore).

3.3.3 Hall effect and magnetoconductance

The $\sigma(T)$, Hall effect and magnetoconductance were measured using a physical property measurement system (PPMS, model PPMS-14, Quantum Design) with a device fabricated with Hall bar geometry. The longitudinal and transverse voltages were recorded simultaneously while the magnetic field B was swept from 8 T to −8 T at rate of 0.5 T min^{-1}. The Hall coefficient R_H, Hall mobility μ_H, and Hall carrier concentration n_H were extracted using the following equations, $R_H = (dV_H/dB)\times(t/I)$, $\mu_H = |R_H|\sigma$, and $n_H = 1/(eR_H)$, where t is the thickness of the active layer. To extract the actual hall voltage V_H, the B-independent and B-dependent offset voltages due to the contribution of positive magnetoconductance were subtracted from the measured ΔV_{xy}, as reported previously.

3.3.4 Other characterization method

UV-vis spectra were measured using a JASCO V-730 spectrophotometer. GIWAXS data were measured at the 9A U-SAXS beam line at the Pohang Accelerator Laboratory, Pohang, Korea. The film thickness and surface morphology

were characterized in a non-contact mode by AFM (Park systems XE-100 and Veeco, Nanoscope IV). SPC was characterized by KPFM (Bruker Nanoscope V MultiMode 8) using a Pt/Ir-coated cantilever (S CM-PIT-V2). The local currents of the films were measured with the contact mode C-AFM using a same cantilever. The work function of the films was measured using an AXIS ultra-DLD (Kratos) equipped with He I gas (21.22 eV) as a UV source. The work functions of the films were characterized by analyzing the surface potential contrast (SPC) data obtained from KPFM using the similar cantilever. The capacitance–voltage characteristics of the MIS devices were obtained at a frequency of 100 Hz using an Agilent B2912A source–measure unit and a Wayne Kerr 4100 LCR meter. The carrier concentrations were determined from the C^{-2}–V plot based on the Mott–Schottky analysis.

Chapter 4. Heavily doped semi-crystalline polymers for high performance thermoelectrics

4.1 Introduction

Recently, organic thermoelectric devices have attracted substantial attention because they can more efficiently convert low temperature waste heat into electricity than inorganic TE devices. Additionally, the unique properties, such as light weight, flexibility, and easy processability, enable the utilization of organic TE devices in a variety of applications[15, 24, 89-91]. So far, π-conjugated polymers[20, 26, 35, 46, 51], carbon allotropes[17-19] and small molecules[25, 60, 92] have been used as active materials in organic TE devices. Among them, conducting polymers are considered one of the most promising candidates for these active materials because of their easy processability, high electrical conductivity (σ), and low thermal conductivity (κ) compared to other materials.

The performance of TE materials can be described in terms of the dimensionless figure of merit, $ZT = (\alpha^2\sigma T)/\kappa$, where α and T are the Seebeck coefficient and absolute temperature, respectively, or the power factor (PF) $\alpha^2\sigma$. In general, there is a trade-off relationship between α and σ depending on the carrier concentration (n) [8, 57, 65, 93]. Thus, it is essential to determine the α–σ relationship because it can help us understand the charge transport mechanism in conducting polymers and optimize the TE performance[53, 57, 64, 68, 69, 76, 77, 79, 82, 94, 95]. There have been many studies on this relationship; for instance, Glaudell et al. found the empirical relationship in which $\alpha \propto \sigma^{-1/4}$, which successfully fit the experimental data from a variety of doped polymers[68]. However, the physical origins of this model are unclear. Kemerink et al. suggested a modified variable-range-hopping (VRH) model that is suitable for non-degenerately doped

semiconducting polymers[77]. In 2017, Kang and Snyder proposed a charge transport model using an energy-dependent transport parameter *s* and an energy-independent transport coefficient σ_{E0}, which fits well with the α–σ relationship of polymers over almost the entire range of electrical conductivity[76]. The analysis of the relationship based on this model elucidates the fundamental charge transport mechanism and enables the design of an optimized TE device.

In particular, the Kang–Snyder model can be applied for both non-degenerately and degenerately doped semiconductors by changing the parameter *s*. Thus, the energy-dependent parameter *s*, which is affected by the structural and energetic disorder of polymers, is important for determining the charge transport mechanism[69, 76]. For most previously reported conducting polymers, for instance, P3HT, PBTTT, and poly(2,5-bis(thiophene-2-yl)-(3,7-diheptadecanyltetrathienoacene)) (P2TDC$_{17}$-FT4), the parameter $s = 3$, which means that impurity scattering is the major mechanism of charge transport[76]. However, materials with lower *s* values (*i.e.*, $s = 1$) are required for better electrical conductivity as well as higher TE performance, which can be obtained with highly crystalline and/or degenerate polymers[76, 79, 95]. Nevertheless, the $s = 1$ relationship has not been demonstrated except for crystalline PEDOT and its derivatives[76] because of the limited ionization of dopants in doped polymers and/or the poor crystallinity of the doped polymer films due to the need for heavy doping for a high carrier concentration.

Here, I successfully demonstrate degenerately doped semi-crystalline polymers with the α–σ relationship following $s = 1$ using two semi-crystalline π-conjugated polymers, poly[(4,4′(bis(hexyldecylsulfanyl)methylene)cyclopenta[2,1-b:3,4-b′]dithiophene)-alt-(benzo[c][1,2,5]thiadiazole)] (PCPDTSBT) and poly[(2,5-bis(2-hexyldecyloxy)phenylene)-*alt*-(5,6-difluoro-4,7-di(thiophen-2-yl)benzo[c][1,2,5]thiadiazole)] (PPDT2FBT). I doped the films with a strong oxidant,

iron chloride ($FeCl_3$), by the overcoating method to achieve degenerately doped conditions (n up to ~10^{21} cm^{-3}) while maintaining their crystallinity. As a result, *PF*s of 112.01 μW m^{-1} K^{-2} for PPDT2FBT and 49.80 μW m^{-1} K^{-2} for PCPDTSBT were obtained, which are outstanding values among doped semiconducting polymers except for PEDOT derivatives. The effect of the dopant concentration on the film morphology and dopant homogeneity was investigated by grazing incidence wide-angle X-ray scattering (GIWAXS) measurements and Kelvin probe force microscopy (KPFM). In addition, the origins of the high *PF* and charge transport properties in our doped polymers were systemically studied by analysing the α–σ relationship and the weighted mobility μ_w based on the Kang–Snyder model and by measuring the temperature-dependent conductivity of the doped films. The high TE performance with the charge transport mechanism following s = 1 in degenerately doped semi-crystalline polymers can be used to suggest a few strategies to develop high-performance organic TE devices.

4.2 Characterization of TE properties

To achieve high electrical conductivity, I first introduced two semi-crystalline D–A type polymers, PCPDTSBT with sp^2-hybridized C=C double bonds on its side chain and PPDT2FBT with noncovalent Coulomb interactions (S···O, S···F, and C–H···N) and intra- and/or intermolecular noncovalent hydrogen bonds, as shown in **Figure 4.1a and 4.1b**. As reported previously, both polymer films show high crystallinity based on their highly planar backbone structures[57, 96]. The strong p-type acceptor $FeCl_3$ was adopted as the dopant. To prepare $FeCl_3$-doped PCPDTSBT and PPDT2FBT films, dopant solutions in acetonitrile with various concentrations (0.5–60 mM) were coated on top of the pristine polymer films to preserve the well-ordered film morphology. Here, I denote the films as PCPDTSBT-OC and PPDT2FBT-OC, respectively. To compare the morphologies of the films, a sample was prepared by spin-casting the mixture of the PCPDTSBT and dopant solutions, and this film was named PCPDTSBT-Mix. The resulting films have thicknesses of ~70 nm and ~100 nm from mixing and overcoating, respectively. The detailed procedures are described in the experimental section.

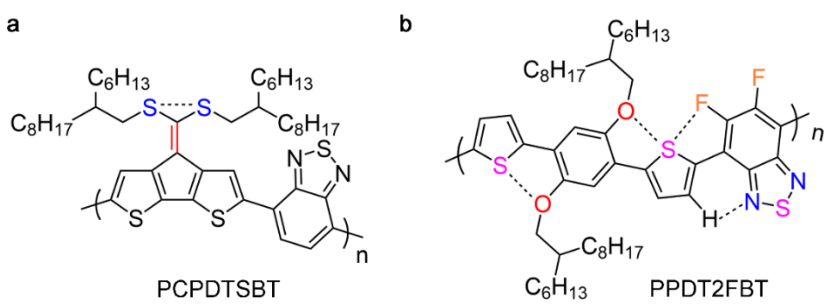

Figure 4.1 Molecular structure of semi crystalline polymers. (a) PCPDTSBT and (b) PPDT2FBT

Generally, molecular doping in a polymer film modulates the σ value by the formation of (bi)polaron states[46, 72, 93]. To observe this phenomenon, I first

measured the UV–vis absorption of the films as a function of the $FeCl_3$ concentration. As shown in **Figure 4.2**, in both the PCPDTSBT-Mix and PCPDTSBT-OC films, the neutral absorption peaks at approximately 830 nm gradually fade, while the polaron absorption over 900 nm increases as the dopant concentration increases, showing that PCPDTSBT can be efficiently doped by $FeCl_3$ regardless of the doping method. This result is also supported by the change in the work function obtained in the cutoff region in the ultraviolet photoelectron spectroscopy (UPS) spectra (**Figure 4.2e**). The work function of the pristine PCPDTSBT film was 4.31 eV. As the $FeCl_3$ concentration increased, the work function of the PCPDTSBT-OC and PCPDTSBT-Mix films increased to 5.09 eV and 4.79 eV, respectively, at the maximum dopant concentration. This gradual increase in the work function indicates that the Fermi level and the HOMO level of the polymer approach each other because of the increased number of the free charge carriers[53, 97]. The PPDT2FBT films also have similar results in terms of the absorption spectra and the work function, as shown in **Figure 4.2c and 4.2e.**

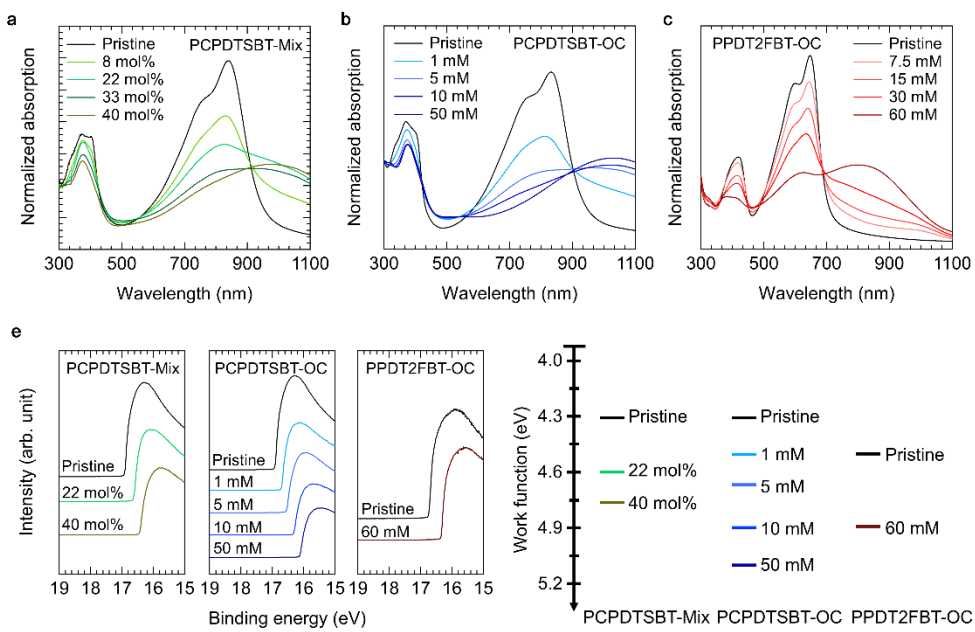

Figure 4.2 Characterization of doped semi-crystalline polymers. UV-vis

absorption spectra of the (a) PCPDTSBT–Mix, (b) PCPDTSBT–OC, and (c) PPDT2FBT–OC as a function of the $FeCl_3$ concentration, and their (e) UPS spectra as well as corresponding work functions.

To investigate the TE properties of the doped polymer films, I measured σ with a four-point probe method and measured α with a customized measurement system as illustrated in **Figure 4.3a**. The detailed measurement configuration is described in the experimental section. **Figure 4.3b** and **3c** show the TE properties of the PCPDTSBT-OC and PPDT2FBT-OC films, respectively. In both overcoated films, the σ values drastically increased as the $FeCl_3$ concentration increased due to the increased number of free carriers, as confirmed by the UV–vis absorption and UPS spectra; in the PCPDTSBT-OC film, σ was 0.002 S cm^{-1} at 0.25 mM and increased to 205.9 S cm^{-1} at 50 mM, which is almost 5 times higher than that of the maximum σ in PCPDTSBT-Mix (41.9 S cm^{-1} at 40 mol%) (**Figure 4.3d**). Additionally, these values are considerably higher than those given in our previous report on the same polymer in which $[B(C_6F_5)_3]$ was mixed as a dopant (7.5 S cm^{-1}) [57]. The PPDT2FBT-OC film also showed a high σ of 125.1 S cm^{-1} at 60 mM, which is 5-orders of magnitude higher than that at 5 mM $FeCl_3$ (0.008 S cm^{-1}). Both $FeCl_3$-overcoated films demonstrated excellent σ values based on the use of a strong dopant and an efficient doping method compared with other doped semiconducting polymers (**Table 4.1**). Moreover, the typical trade-off relationship between σ and α is observed for all the films. The Seebeck coefficient of PCPDTSBT-OC decreases from 793.5 μV K^{-1} at 0.25 mM to 28.8 μV K^{-1} at 50 mM, while that of PPDT2FBT-OC changes from 893.5 μV K^{-1} at 5 mM to 66.0 μV K^{-1} at 60 mM. PPDT2FBT-OC showed slightly higher α values than PCPDTSBT-OC due to its deeper HOMO energy level (*i.e.*, −5.45 eV for PPDT2FBT and −5.10 eV for PCPDTSBT). The maximum *PF*s of PCPDTSBT-OC and PPDT2FBT-OC were 49.80 μW m^{-1} K^{-2} at 5 mM and 112.01 μW m^{-1} K^{-2} at 45 mM, respectively, which are considerably higher

than those of the other doped semiconducting polymer TE devices (**Table 4.1**). The performance of all the devices as a function of the dopant conditions is summarized in **Table 4.2**. It is interesting that the *PF* values of the PCPDTSBT-OC and PPDT2FBT-OC films as a function of the $FeCl_3$ concentration reach a peak at a certain dopant concentration (*i.e.*, 5 mM for PCPDTSBT-OC and 45 mM for PPDT2FBT-OC) much earlier than reaching the maximum point of σ. By contrast, PCPDTSBT-Mix shows the maximum *PF* at the saturated dopant concentration (**Figure 4.3d**) similar to many other doped polymers previously reported[68, 93]. The *PF* maximum is obtainable when the electronic state of the semiconductor changes from non-degenerate to degenerate[79, 98]. To verify the transition related to the *PF* maximum in our cases, I analyzed the α–σ relationship with the Kang–Snyder model.

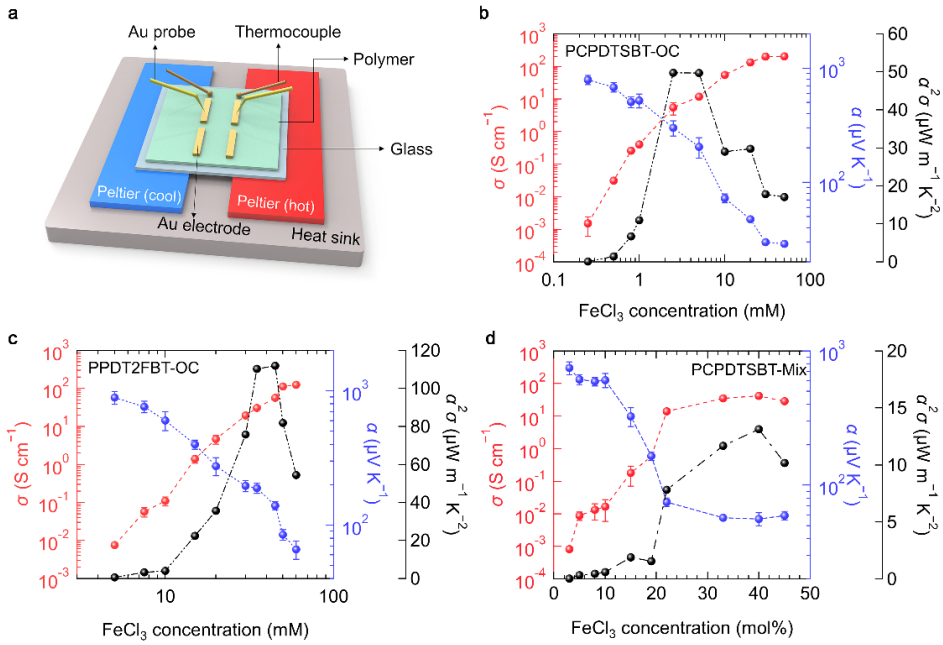

Figure 4.3 Thermoelectric characterization of doped semi-crystalline polymers.

(a) Schematic illustration of the thermoelectric device. (b) Thermoelectric properties of (c) PCPDTSBT–OC and (d) PPDT2FBT-OC, and (e) PCPDTSBT-Mix.

Table 4.1 Thermoelectric properties of various doped conducting polymers.

Polymer	Dopant / Methods	σ (S cm^{-1})	α (μV K^{-1})	PF (μW m^{-1} K^{-2})	Ref.
PPDT2FBT	$FeCl_3$ / Overcoating	57.3	139.8	112.0	This work
PCPDTSBT	$FeCl_3$ / Overcoating	11.9	204.6	49.80	This work
	$FeCl_3$ / Mixing	41.9	56.0	13.14	This work
PBTTT	FTS / Vapor	1000	33	110	[66]
	F_4TCNQ / Vapor	220	39	32	[66]
	EBSA / Dipping	1300	14	25	[65]
	F_4TCNQ / Mixing	3.51	60	1.3	[65]
	F_4TCNQ / Solid-state diffusion	120.4	71.7	61.9	[69]
PDPP3T	$FeCl_3$ / Overcoating	52	217	247	[50]
PDPP-4T	$FeCl_3$ / Mixing	15	150	33.75	[99]
PDPPSe-12	$FeCl_3$ / Dipping	~ 900	~ 57	300	[100]
P3HT	F_4TCNQ / Solid-state diffusion	3.3	66.9	1.48	[69]
	FTS / Vapor	27.7	60	9.97	[68]
	$FeCl_3$ / Overcoating	42	105	46	[50]
CDT-BTZ	F_4TCNQ / Solid-state diffusion	4.4	147.37	9.55	[69]
PCDTFBT	F_4TCNQ / Mixing	6.91	213	31.5	[93]
PCDTPT	F_4TCNQ / Mixing	5.13	211	21.8	[93]
PEDOT:Tos	TDAE / Vapor	90	190	325	[20]

Table 4.2 Thermoelectric properties of PCPDTSBT-OC, PCPDTSBT-Mix, and PPDT2FBT-OC.

Polymer	Films	σ (S cm^{-1})	α (μV K^{-1})	$\alpha^2\sigma$ (μW m^{-1}K^{-2})
PCPDTSBT-OC	0.25 mM	0.002 (± 0.001)	793.5 (± 73.49)	0.097
	0.5 mM	0.03 (± 0.003)	681.6 (± 64.41)	1.46
	0.8 mM	0.26 (± 0.047)	506.3 (± 55.78)	6.72
	1 mM	0.41 (± 0.078)	521.2 (± 73.64)	11.00
	2.5 mM	5.51 (± 2.24)	300.5 (± 45.72)	49.76
	5 mM	11.90 (± 2.49)	204.6 (± 42.12)	49.80
	10 mM	55.45 (± 5.30)	72.3 (± 6.44)	28.99
	20 mM	132.58 (± 6.00)	47.4 (± 2.13)	29.76
	30 mM	200.57 (± 8.90)	29.8 (± 0.34)	17.85
	50 mM	205.93 (± 6.18)	28.8 (± 0.93)	17.07
PCPDTSBT-Mix	3 mol%	0.001 (± ~10^{-6})	748.1 (± 82.54)	0.05
	5 mol%	0.009 (± 0.003)	612.5 (± 53.27)	0.33
	8 mol%	0.013 (± 0.007)	594.6 (± 44.31)	0.47
	10 mol%	0.017 (± 0.011)	605.4 (± 73.64)	0.61
	15 mol%	0.18 (± 0.11)	325.0 (± 52.37)	1.91
	19 mol%	0.58 (± 0.05)	165.4 (± 12.34)	1.57
	22 mol%	13.98 (± 0.59)	74.8 (± 5.31)	7.82
	33 mol%	35.51 (± 0.17)	57.3 (± 2.37)	11.68
	40 mol%	41.89 (± 0.76)	56.0 (± 6.42)	13.14

	45 mol%	28.92 (± 1.25)	59.3 (± 4.23)	10.17
PPDT2FBT-OC	5 mM	0.008 (± ~10^{-6})	893.5 (± 97.46)	0.61
	7.5 mM	0.057 (± 0.016)	762.8 (± 75.34)	3.34
	10 mM	0.11 (± 0.030)	603.2 (± 95.64)	4.00
	15 mM	1.41 (± 0.33)	399.1 (± 31.12)	22.44
	20 mM	4.70 (± 1.23)	275.6 (± 42.37)	35.71
	30 mM	19.68 (± 2.52)	196.3 (± 18.74)	75.82
	35 mM	31.01 (± 1.67)	188.6 (± 16.10)	110.34
	45 mM	57.28 (± 5.31)	139.8 (± 9.97)	112.01
	50 mM	113.56 (± 3.73)	87.9 (± 7.58)	81.87
	60 mM	125.10 (± 5.15)	66.0 (± 10.34)	54.49

4.3 TE properties–charge transport relationships

Analysis of the α–σ relationship using the Kang–Snyder model is useful to understand the charge transport behaviors[69]. The α–σ relationship of various conducting polymers has been well described with this model, which newly defines the form of the transport function $\sigma_E(E)$ using two essential parameters, a transport edge E_t and a transport parameter s (Eq. 3). In this model, s is a parameter that determines the conduction mechanism, and σ_{E0} presents the transport ability.

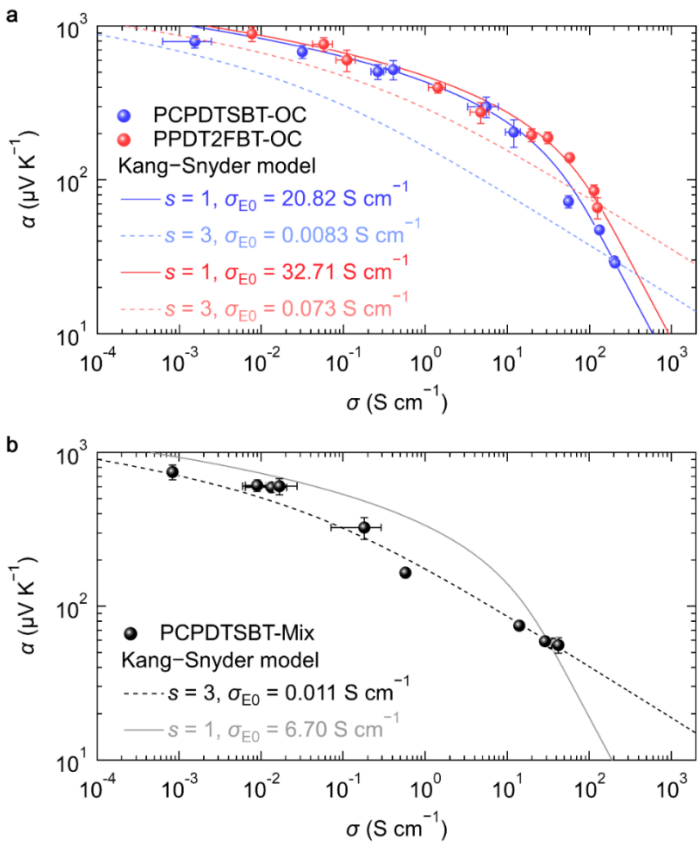

Figure 4.4 *α*–*σ* relationship of degenerately doped polymers. (a,b) *α*–*σ* relationship of the films and fits to the Kang–Snyder model.

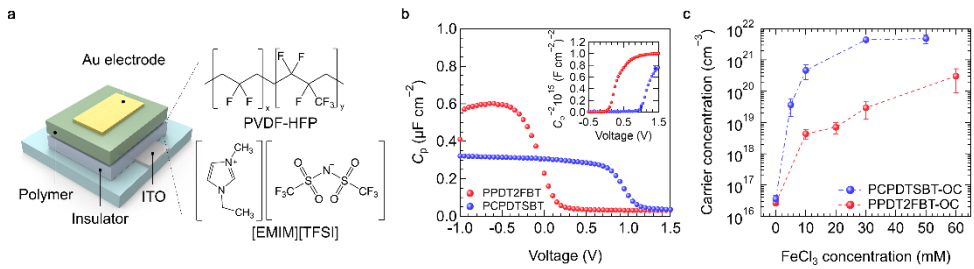

Figure 4.5 Mott–Schottky analysis for extracting carrier concentration. (a) Scheme of the MIS device structure. (b) Capacitance–voltage characteristics of the pristine PPDT2FBT and PCPDTSBT films. The inset shows the C_p^{-2}–V plot to extract the carrier concentration. (c) The carrier concentration of PCPDTSBT and PPDT2FBT calculated from the Cp^{-2}–V plot.

As shown in **Figure 4.4a** and **4.4b**, the Kang–Snyder model fits our experimental data well over the entire conductivity range. Interestingly, the α–σ curves with s = 1 have an excellent fit with the data of the overcoated samples, PCPDTSBT-OC and PPDT2FBT-OC. This result is meaningful because the relationship with s = 1 has been shown only in PEDOT derivatives but has not yet been shown in molecular doped semiconducting polymers which generally follow s = 3 (including the PCPDTSBT-Mix sample) [23]. As described above, the parameter s is associated with the charge transport mechanism. In detail, the α–σ relationship with s = 1 means that phonon scattering mainly affects the charge transport, which can be observed in materials possessing a narrow DOS due to high crystallinity and/or degenerate energy states. In the case of s = 3, charge transport is governed by impurity scattering, as seen in several typical semiconducting polymers with a relatively broad DOS[76, 95]. When $\eta \ll 1$ (*i.e.*, a non-degenerate regime), the shape of the curves is nearly the same as that of $\alpha \propto \ln\sigma$ regardless of parameter s. However, in a degenerate region ($\eta \gg 1$), the α–σ curves with s = 1 take the form of $\alpha \propto \sigma^{-1}$, which is steeper than those with s = 3 possessing $\alpha \propto \sigma^{-1/3}$.

For a more quantitative analysis, I extracted the carrier concentration of the samples using the Mott–Schottky equation via metal-insulator-semiconductor (MIS) admittance spectroscopy. **Figure 4.5a** shows a schematic illustration of the MIS device structure with an architecture of indium-tin-oxide (ITO)/ion-gel insulator/polymer/Au. For the ion-gel insulator, I used a mixture of poly(vinylidene fluoride-co-hexafluoropropylene) (PVDF-HFP) and 1ethyl-3-methylimidazolium bis(trifluoromethylsulfony)imide ([EMIM][TFSI]). The carrier concentration can be calculated from the capacitance–voltage characteristics in the depletion region using the following equation[101-103]:

$$n = \frac{2}{q\varepsilon_0\varepsilon_r\left(\frac{\partial C_p^{-2}}{\partial V}\right)} \quad (8)$$

where ε_0 is the permittivity of free space, ε_r is the dielectric constant of the active layer, and C_p is the specific capacitance of the device. **Figure 4.5b** shows an example of this calculation with the C_p–V and C_p^{-2}–V characteristics of the MIS device using pristine PCPDTSBT and PPDT2FBT as the active layers. The charge carrier concentrations of the PCPDTSBT-OC and PPDT2FBT-OC films as a fucntion of the $FeCl_3$ concentrations were shown in **Figure 4.5c**.

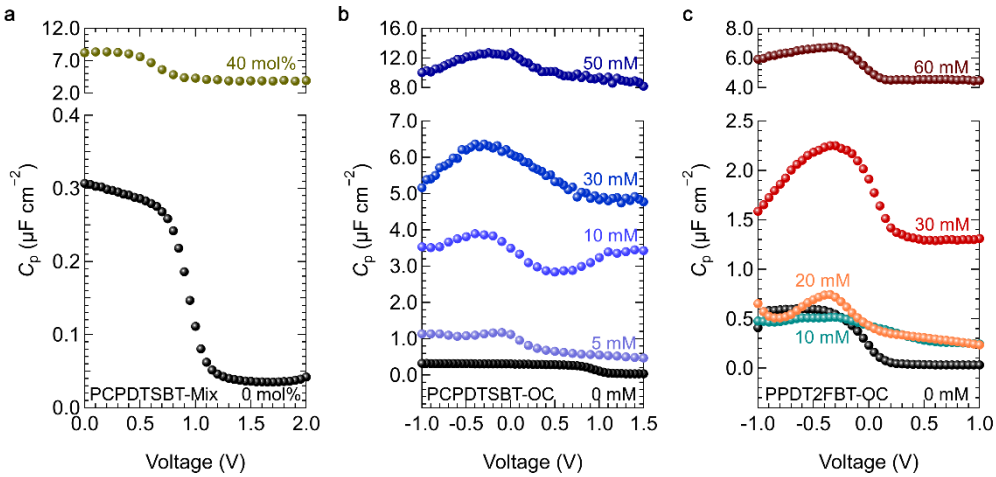

Figure 4.6 MIS admittance spectroscopy of doped polymers. C_p–V characteristics of (a) PCPDTSBT-Mix, (b) PCPDTSBT-OC, and (c) PPDT2FBT-OC to extract the carrier concentration.

The C_p–V characteristics of the other doped films are displayed in **Figure 4.6**. The undoped PCPDTSBT and PPDT2FBT films have n values of 3.6×10^{16} cm^{-3} and 2.6×10^{16} cm^{-3}, respectively. As the $FeCl_3$ concentration increased, the n of PCPDTSBT-OC and PPDT2FBT-OC consistently increased and reached a maximum of 6.0×10^{21} cm^{-3} at 50 mM and 3.1×10^{20} cm^{-3} at 60 mM, respectively, as shown in **Table 4.3.** These are exceptionally high values for doped semiconducting polymers and are comparable to the n of typical metallic conducting polymers, causing the α–σ relationship to follow $s = 1$, as shown above[57, 69, 104]. Therefore, the two overcoated polymer films seem to possess a narrow DOS, a low level of disorder, and/or high crystallinity, which might be the reason for the appearance of the maximum PF. Meanwhile, the PCPDTSBT-Mix film (40 mol%) also showed a high n of 4.7×10^{20} cm^{-3} (**Table 4.3**). Although this value is almost an order of magnitude lower than that of PCPDTSBT-OC, it is still as high as the value of other heavily doped polymers[103]. This result indicates that n is not the sole factor affecting the parameter s. For further investigation of this phenomenon, I

systematically studied the TE properties and the charge transport mechanism in the samples in terms of the arrangement of the polymer chains during the doping process and the dopant distribution, which can also affect the charge transport properties.

Table 4.3 Carrier concentrations of PCPDTSBT-OC and PPDT2FBT-OC derived from admittance spectroscopy.

Polymer	$FeCl_3$ concentration	Carrier concentration (cm^{-3})
PCPDTSBT-OC	Pristine	$3.64 (\pm 1.09) \times 10^{16}$
	5 mM	$3.71 (\pm 2.12) \times 10^{19}$
	10 mM	$4.73 (\pm 2.36) \times 10^{20}$
	30 mM	$3.93 (\pm 0.94) \times 10^{21}$
	50 mM	$5.97 (\pm 0.75) \times 10^{21}$
PCPDTSBT-Mix	40 mol%	$4.74 (\pm 0.34) \times 10^{20}$
PPDT2FBT-OC	Pristine	$2.62 (\pm 0.28) \times 10^{16}$
	10 mM	$4.35 (\pm 1.50) \times 10^{18}$
	20 mM	$7.09 (\pm 2.84) \times 10^{18}$
	30 mM	$2.99 (\pm 1.67) \times 10^{19}$
	60 mM	$3.09 (\pm 2.19) \times 10^{20}$

4.4 Characterization of morphological properties

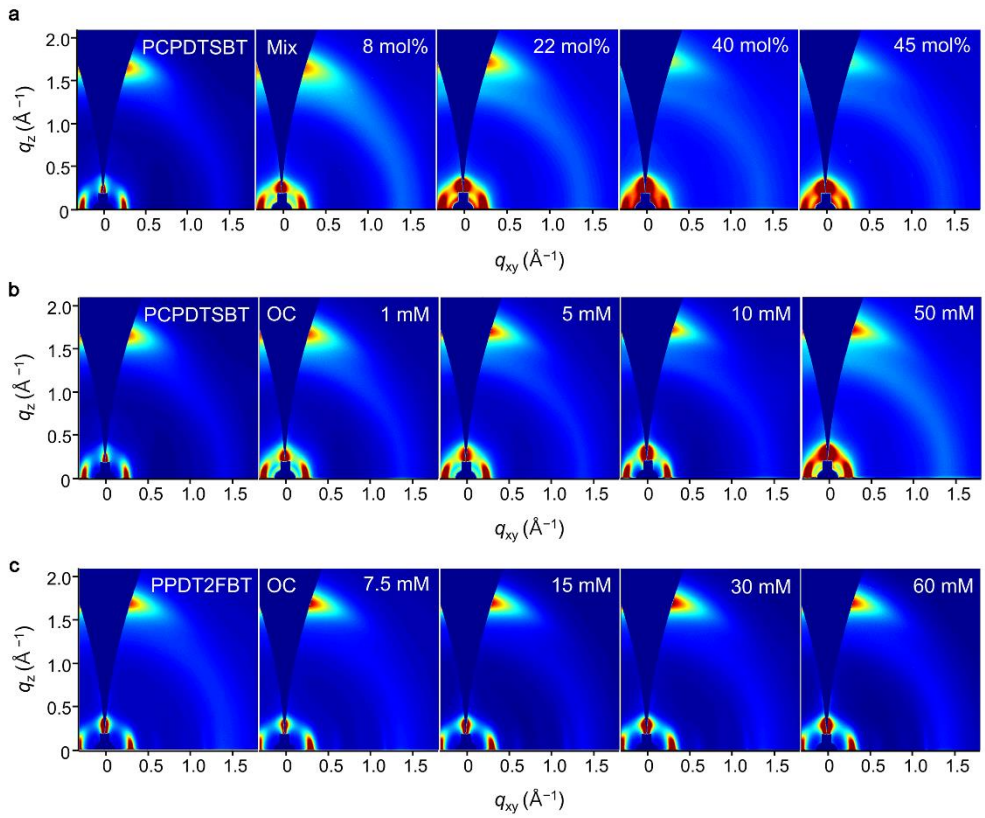

Figure 4.7 Two-dimensional GIWAXS patterns of doped polymers. (a) PCPDTSBT-Mix, (b) PCPDTSBT-OC, and (c) PPDT2FBT-OC at various dopant concentrations.

Because the local structural order of polymer films is highly related to the TE properties[53, 63, 65], I investigated the change in the film morphology and crystallinity due to $FeCl_3$ doping with GIWAXS. The two-dimensional GIWAXS images and corresponding in-plane (IP) and out-of-plane (OOP) line-cut profiles are shown in **Figure 4.7** and **Figure 4.8**, respectively. From the data, I also extracted the d-spacing and the crystalline coherence length (CCL) of the samples (**Figure 4.9** and **Table 4.4**). In the pristine state, both polymers show a pronounced face-on orientation with strong OOP scattering (010) at q_z = 1.67 Å^{-1} (d-spacing = 3.76 Å

and CCL = 24.1 Å) for PCPDTSBT and q_z = 1.68 Å^{-1} (d-spacing = 3.74 Å and CCL = 24.2 Å) for PPDT2FBT, mainly originating from their high planarity. As described in our previous reports on these polymers, chain planarity is extended with strong interchain packing *via* sp^2-hybridized bis(alkylsulfanyl)methylene side chains and sulfur−sulfur (S−S) chalcogen interactions in PCDPTSBT[57]. PPDT2FBT also shows tight π−π stacking owing to its strong interchain interactions *via* noncovalent Coulomb interactions, intra/intermolecular noncovalent hydrogen bonds, and strong dipole–dipole interactions. The tight interchain packing of both polymers results in high charge transport capability[67, 96].

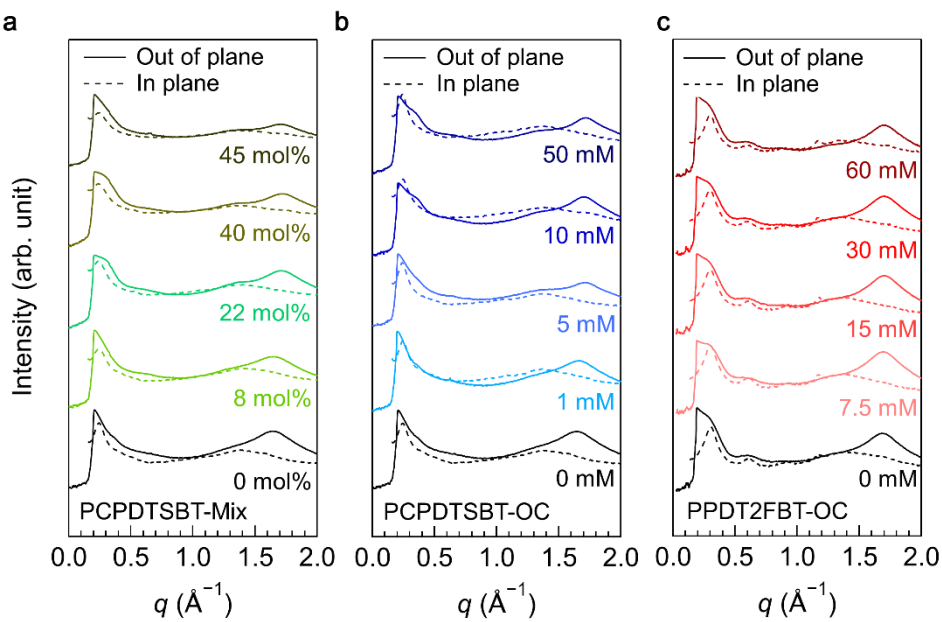

Figure 4.8 GIWAXS line-cut profiles. (a) PCPDTSBT-Mix, (b) PCPDTSBT-OC, and (c) PPDT2FBT-OC.

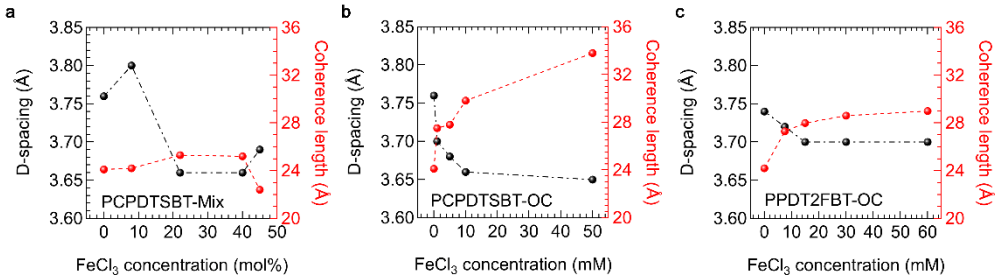

Figure 4.9 GIWAXS parameters obtained from the (010) peak position. π-π stacking distance and coherence length of the (a) PCPDTSBT-Mix, (b) PCPDTSBT-OC, and (c) PPDT2FBT-OC at various dopant concentrations.

Table 4.4 Packing parameters derived from GIWAXS.

Polymers	Doping method	Films	Crystallographic parameters of q_z (010)		
			q_{-1} (Å^{-1})	d-spacing (Å)	CCL (Å)
PCPDTSBT		Pristine	1.670	3.76	24.1
	Overcoating	1 mM	1.699	3.70	27.5
		5 mM	1.707	3.68	27.8
		10 mM	1.715	3.66	29.8
		50 mM	1.719	3.65	33.8
	Mixing	8 mol%	1.652	3.80	24.2
		22 mol%	1.715	3.66	25.3
		40 mol%	1.717	3.66	25.2
		45 mol%	1.702	3.69	22.4
PPDT2FBT		Pristine	1.682	3.74	24.2
	Overcoating	7.5 mM	1.691	3.72	27.3
		15 mM	1.700	3.70	28.0
		30 mM	1.700	3.70	28.6
		60 mM	1.700	3.70	29.0

By doping the films, no noticeable change in the scattering pattern was found in either overcoated film, whereas the (010) peak of the PCPDTSBT-Mix film was disrupted at high dopant concentrations. This shows that the doping method significantly affects the morphology. In the PCPDTSBT-Mix film, the d-spacing and the CCL were maintained as the $FeCl_3$ concentration increases up to 40 mol%. However, when the 45 mol% solution was mixed, the CCL decreased from 24.1 Å (the pristine film) to 22.4 Å, and in turn, σ decreased. This result may be attributed to blending a large amount of dopant, which is likely to disrupt the growth of the crystalline phase and thus hinder charge transport[45, 70]. In contrast, in the PCPDTSBT-OC film, the CCL increases up to 33.8 Å at 50 mM while maintaining the d-spacing , showing that the overcoating method does not disturb the crystallinity of the polymer even up to the degenerate doping level. Consequently, I can infer that the high crystallinity of the PCPDTSBT-OC film is related to the transport parameter $s = 1$ as well as the high σ (>200 S cm^{-1}) and high n (>10^{21} cm^{-3}). The PPDT2FBT-OC film also exhibits changes in the packing parameters by doping similar to the changes observed in PCPDTSBT-OC. The morphology difference can also be found in the atomic force microscopy (AFM) images of the films (**Figure 4.10**). The pristine films of PCPDTSBT and PPDT2FBT have well-ordered semi-crystalline fibril structures and smooth surfaces with low root mean square (RMS) roughness values of 0.71 nm. The overcoated films show no significant change even at a high dopant concentration of 0.99 nm and 1.05 nm for PCPDTSBT-OC at 50 mM and PPD2FBT-OC at 60 mM, respectively. In contrast, PCPDTSBT-Mix with 45 mol% doping shows significant phase segregation with isolated particles that are precipitated due to the solubility limit, resulting in a large RMS roughness (3.30 nm).

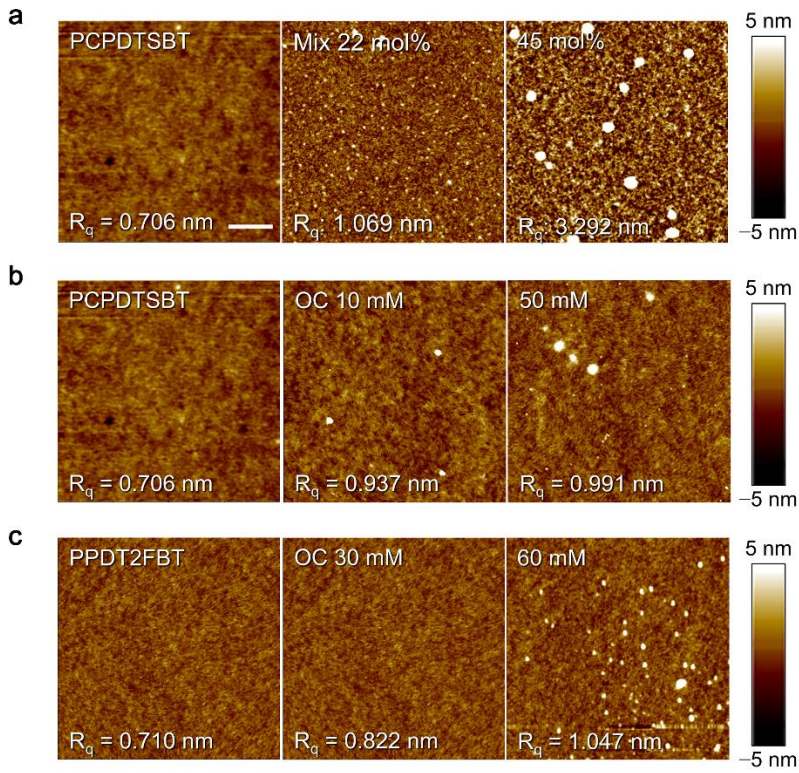

Figure 4.10 AFM height images. (a) PCPDTSBT-Mix, (b) PCPDTSBT-OC, and (c) PPDT2FBT-OC as a function of the $FeCl_3$ concentration.

4.5 Spatial distribution of dopants in doped films

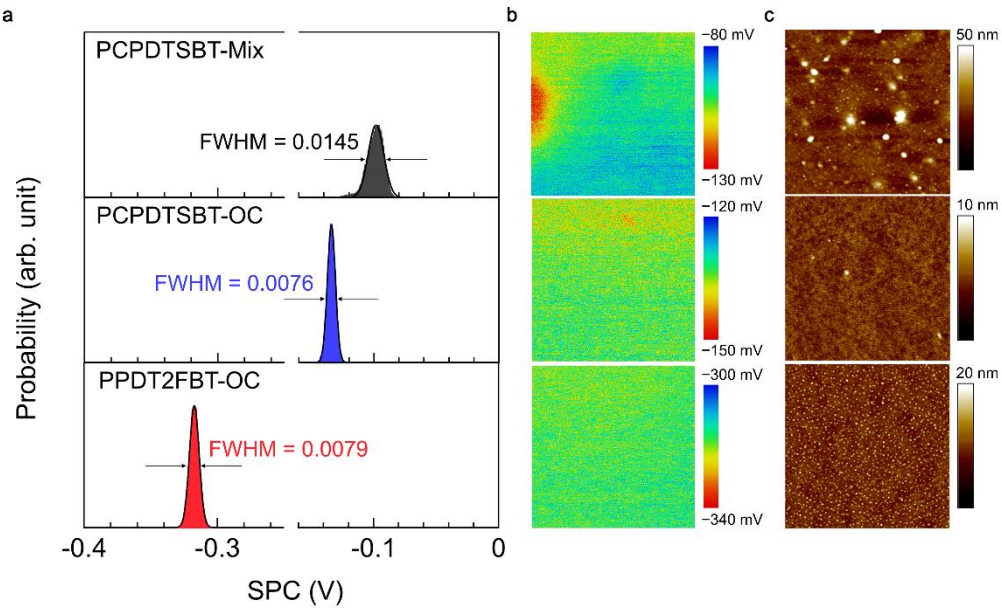

Figure 4.11 Spatial distribution of dopants in doped films. (a) SPC histograms, (b) SPC maps, and (c) height images of PCPDTSBT-Mix, PCPDTSBT-OC, and PPDT2FBT-OC at the maximum dopant concentration. The size of all the AFM images is 5 μm × 5 μm.

The reasons for the differences in the transport parameter s were further studied by examining the spatial distribution of dopants as a function of the doping method. Because Seebeck coefficients are proportional to the slope of the DOS, $g(E)$, according to the Mott formula, $\alpha \propto \mathrm{d}(\ln[g(E)])/\mathrm{d}E$, I can infer that the distinct shape of the α–σ relationship in the PCPDTSBT-OC and PPDT2FBT-OC films correlates with the DOS[44, 68]. A recent study reported by Boyle et al. suggested that the clustering of dopants in doped polymer films can significantly affect the DOS, which changes the transport parameter s[95]. In detail, homogeneous doping reduces the energetic disorder and lowers s, leading to higher TE performance. To investigate the $FeCl_3$ distribution in the degenerately doped films as a function of the doping

method, I compared the surface potential contrast (SPC) of PCPDTSBT-Mix, PCPDTSBT-OC, and PPDT2FBT-OC using KPFM, as shown in **Figure 4.11**, which provides the surface potential difference in a spatial regime. The SPC distributions (**Figure 4.11a**) are plotted from the SPC map shown in **Figure 4.11b** and are fitted to a Gaussian function to estimate the full width at half maximum (FWHM) of the distribution. The result clearly shows that the SPC distribution in PCPDTSBT-OC is much narrower than that in PCPDTSBT-Mix. The FWHM of PCPDTSBT-Mix is 1.45×10^{-2}, whereas that in PCPDTSBT-OC is 7.6×10^{-3}. In addition, the surface topology at the same position in the SPC image is shown in **Figure 4.11c**, displaying that the mixed film has a much rougher surface than the sequentially doped film. Similar to the PCPDTSBT-OC film, the PPDT2FBT-OC film has a sharp SPC distribution with an FWHM of 7.9×10^{-3} and a smooth surface. The results indicate that the dopant homogeneity and the film morphology can be improved by the overcoating method. Also, considering the SPC distribution, I anticipate that *s* is highly correlated to the DOS.

4.6 The *PF* maximum in the *s* = 1 system

Figure 4.12a shows the *PF*–σ relationship of all the films. The data points of all the doped films agree well with the simulation curves based on the Kang–Snyder model. Here, I can observe that the relationship between *PF* and σ also varies with the parameter *s*. The *PF* curve with *s* = 3 steadily increases in proportion to σ. As seen in the plot, both the higher σ_{E0} (*i.e.*, the higher carrier mobility) and the higher η (*i.e.*, the higher doping level) lead to a higher *PF* for a given σ[69, 82]. In contrast, the *PF*–σ relationship following *s* = 1 shows a *PF* maximum at a certain σ, which decreases after that point; this trend is typically found in degenerate semiconductors with a narrow parabolic band[69, 79]. The *s* = 1 system also has a higher *PF* when σ_{E0} is higher similar to the *s* = 3 system, but there is an optimal η corresponding to the maximum *PF*. By comparing the *PF*–σ relationships with two different parameter *s* values, it is suggested that the *s* = 3 system is better than the *s* = 1 system because the *PF* progressively increases as σ increases; thus, an extremely high *PF* can be obtained. However, reaching a high *PF* is not achievable in practice; for example, the PCPDTSBT-Mix may reach the *PF* of PCPDTSBT-OC (49.80 μW m^{-1} K^{-2}) if I increase σ from 41.9 S cm^{-1} to 2705.3 S cm^{-1} (where η = 62.60) in the *s* = 3 system. At that time, the corresponding *n* should be ~10^{22} cm^{-3} when I assume that the mobility is not changing. However, in general, it would be impracticable to increase *n* to such a high value by mixing dopant molecules due to the limitation of the solid solubility[45, 93]. As shown above, maintaining the film morphology is also difficult. Thus, the *PF* of a doped polymer system following *s* = 3 can be theoretically higher than that following *s* = 1, but it cannot be realized. On the other hand, the polymers following *s* = 1 are likely to attain an optimal *PF* at a relatively low dopant concentration. The PCPDTSBT-OC and PPDT2FBT-OC films follow

this trend, showing maximum *PF*s (49.80 μW m^{-1} K^{-2} and 112.01 μW m^{-1} K^{-2}) at a feasibly low σ of 11.9 S cm^{-1} and 57.3 S cm^{-1}, respectively.

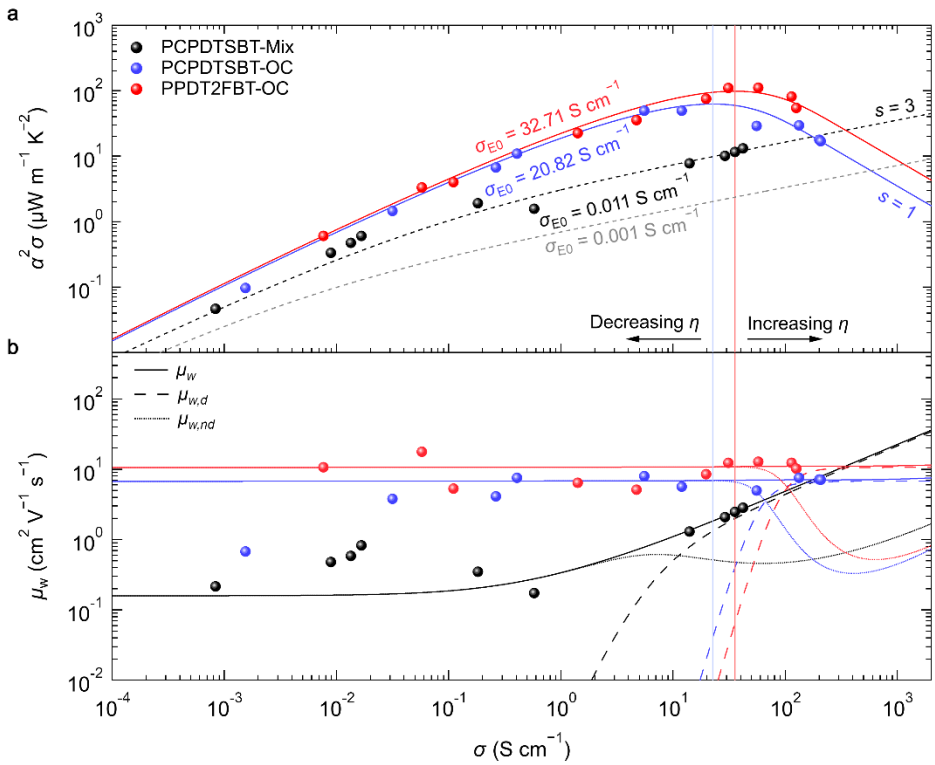

Figure 4.12 Effect of the transport parameter *s* on *PF*. (a) The markers are the *PF*s of PCPTDTSBT-Mix, PCPDTSBT-OC, and PPDT2FBT-OC. The solid and dashed lines present the simulated PFs from the Kang–Snyder model with s = 1 and s = 3, respectively. (b) The weighted mobility from the experimental data is marked with circles. The curves are the calculated weighted mobility values (solid lines) consisting of the degenerate limit (dashed lines) and the non-degenerate limit components (dotted lines). The vertical lines across the graphs, light blue for PCPDTSBT-OC and light red for PPDT2FBT-OC, show that the *PF* maximum coincides with the area of transition from the non-degenerate regime to the degenerate regime.

It is important to determine when the maximum *PF* appears for s = 1 systems to establish a strategy to improve the performance of TE devices. I utilized

the weighted mobility μ_w, which enables the identification of the electronic structure and charge transport mechanisms, as recently reported by the Snyder group using α and σ, as follows[48]:

$$\mu_w = \frac{3h^3\sigma}{8\pi q(2m_e k_B T)^{3/2}}\left[\frac{\frac{3}{\pi^2}\frac{|\alpha|}{k_B/q}}{1+\exp\left[5\left(\frac{|\alpha|}{k_B/q}+1\right)\right]}+\frac{\exp\left[\frac{|\alpha|}{k_B/q}-2\right]}{1+\exp\left[-5\left(\frac{|\alpha|}{k_B/q}+1\right)\right]}\right] \quad (9)$$

where h is Planck's constant and m_e is the electron mass. Experimental (markers) and simulated μ_w–σ (solid lines) plots are shown in **Figure 4.12b**, showing noticeable differences depending on the value of s in the α–σ relation. In detail, μ_w for s = 3 consistently increases with respect to σ, whereas μ_w for s = 1 is almost constant over the entire σ region. The large change in μ_w for s = 3 is known as a sign of the deviation from the free electron model because of the presence of grain boundaries and/or impurity scattering[105, 106]. The calculated μ_w values of PCPDTSBT-OC and PPDT2FBT-OC are 6.7–7.5 cm^2 V^{-1} s^{-1} and 10.6–11.5 cm^2 V^{-1} s^{-1}, respectively. Meanwhile, the PCPDTSBT-Mix film exhibits a μ_w of ~0.2 cm^2 V^{-1} s^{-1} at a low σ range and ~2.9 cm^2 V^{-1} s^{-1} at the maximum σ. Although the theoretical value of μ_w of PCPDTSBT-Mix can increase continuously, a higher μ_w is unachievable due to the restrictions explained above.

Furthermore, I rewrite μ_w by dividing it into two components, $\mu_w = \mu_{w,d} + \mu_{w,nd}$, where $\mu_{w,d}$ (corresponding to the first term in **Equation (5)** and $\mu_{w,nd}$ (corresponding to the second term in **Equation (5)**) are the analytical results for the degenerate limit and for the non-degenerate limit, respectively; then, μ_w, $\mu_{w,d}$ and $\mu_{w,nd}$ curves are drawn in **Figure 4.12b** using the α and σ values obtained from the best fits with different s values. A significant finding in this graph is that the *PF* maxima in the overcoated films (following s = 1) appear at a σ where $\mu_{w,d}$ starts to contribute to μ_w, as indicated by the vertical lines in **Figure 4.12a**,**b**. In other words, the *PF* maximum is obtained when the doping state switches from non-degenerate to degenerate. This result is also highly consistent with the recent literature reporting

that the maximum *PF* is shown with the insulator-to-metal transition[79]. Based on these results, I can conclude that the $s = 1$ system is more favourable than the $s = 3$ system to achieve high TE performance. Additionally, the theoretical PF maximum point can be enhanced by increasing σ_{E0} (*i.e.*, intrinsic mobility of polymers).

4.7 Charge transport in heavily doped polymers

For a deeper understanding of the charge transport properties of the films, I measured the temperature-dependent electrical conductivity of each film with maximum σ at temperatures from 20 K to 330 K. As shown in **Figure 4.13a**, I can observe that σ increases as the temperature increases above a certain temperature. Interestingly, the ratio of σ(20 K)/σ(330 K) in PCPDTSBT-Mix (5.1) is higher than those of the other samples with the overcoating method, with values of 2.0 for PCPDTSBT-OC and 2.9 for PPDT2FBT-OC. This means that the mixed film possesses a higher level of disorder[84], which corresponds to the GIWAXS and KPFM data. It is also notable that the σ values of all the films become constant as the temperature decreases below a certain temperature, implying insulator-to-metal transition in low-temperature regions. These characteristics originate from the improved coupling between the polymer chains with reduced vibrational amplitudes at low temperatures, which is generally found in films with a highly ordered structure[15, 57]. This finding can also be supported by the reduced activation energy $W(T)$ *vs*. T (the Zabrodskii plot), which is expressed as $W(T) = d\ln[\sigma(T)]/d\ln(T)$. As shown in **Figure 4.13b**, all films in this study exhibit a positive slope, indicating that the transport regime of the films has a metallic nature, as reported previously[57, 84]. I also extracted the activation energy E_a using the Arrhenius equation $\sigma = \sigma_0 \exp(E_a/k_B T)$, where σ_0 is a temperature-independent prefactor, as shown in **Figure 4.13c**. In the low-temperature region, an extremely

low E_a of 0.3–0.6 meV was obtained for all films, which also supports the electrical properties close to metal. Meanwhile, the E_a extracted at the high T region was 28.2 meV, 10.7 meV, and 14.8 meV for PCPDTSBT-Mix, PCPDTSBT-OC, and PPDT2FBT-OC, respectively. Although these values are higher than those in the low T region, they are still much lower than those of typical doped organic materials[17, 107]. This result indicates that the electron charges were efficiently transferred from the polymer chains to the dopant molecules, and thus, the tail states of the DOS were filled with a larger number of charge carriers in the doped films[108]. In addition, it is notable that the E_a of the PCPDTSBT-OC film was evidently lower than that of the PCPDTSBT-Mix film, which can be attributed to the high n and low structural disorder originating from the well-maintained crystallinity under heavily doped conditions, as shown in the GIWAXS patterns.

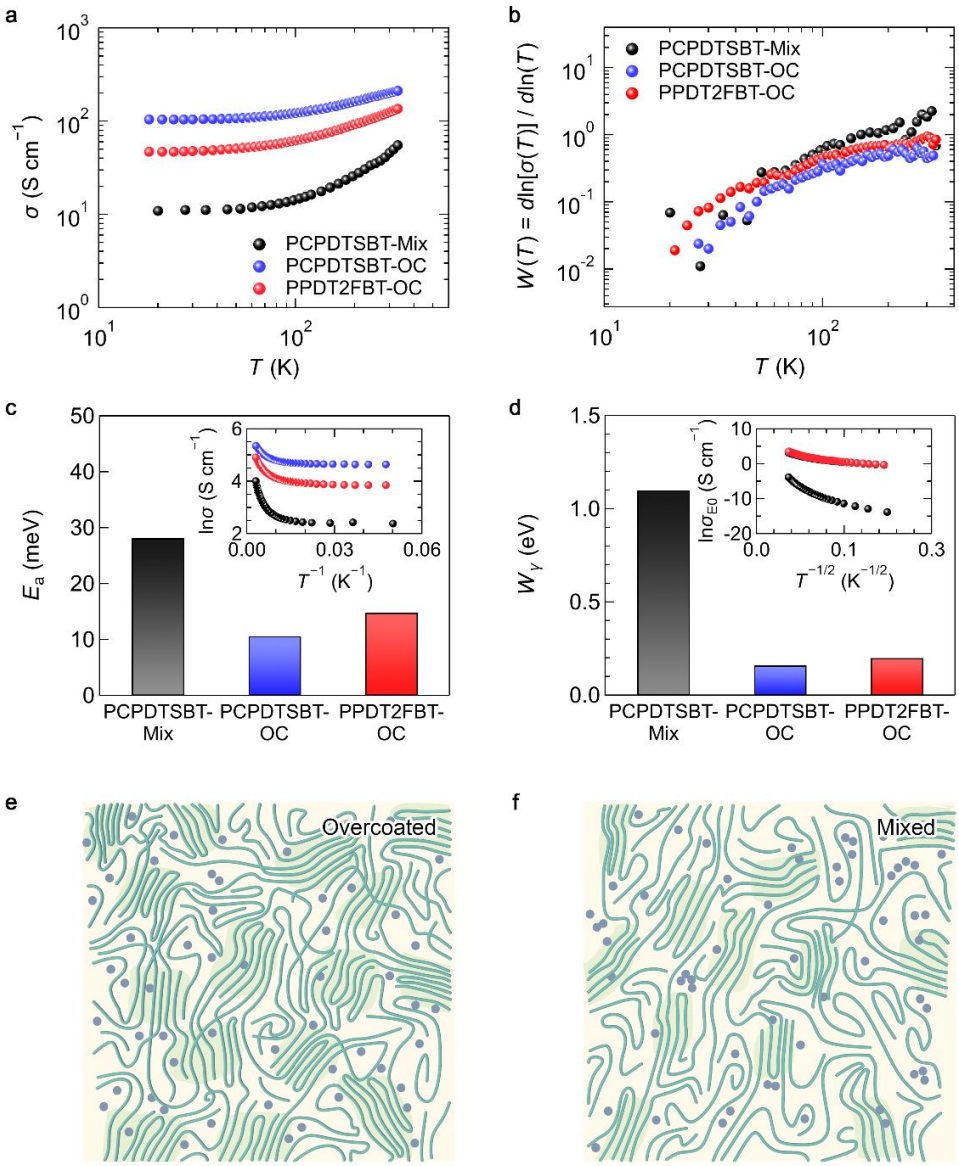

Figure 4.13 Charge transport properties of doped polymers. (a) Temperature dependence of the electrical conductivity σ and (b) the reduced activation energy $W(T)$ of the samples at the maximum dopant concentration, and their (c) activation energy E_a and (d) the transport barrier W_γ. Inset images show the lnσ vs T^{-1} and lnσ_{E0} vs $T^{-1/2}$ plots, respectively. (e,f) Schematic images of film morphology of (e) the overcoated films and (f) the mixed films.

One peculiar phenomenon is that the PCPDTSBT-Mix film, with a positive slope in the Zabrodskii plot (**Figure 4.13b**), has $s = 3$ in the α–σ relationship. In general, charge transport is highly related to the size of the ordered regions and their connectivity by tie molecules[61, 76, 79]. As shown in the GIWAXS, the PCPDTSBT-Mix film had smaller crystalline domains; however, it is not significant to show lower σ than PCPDTSBT-OC. Therefore, based on the SPC and AFM data, it is expected that the PCPDTSBT-Mix film has structural disorder (accompanying energetic disorder) mainly originating from inhomogeneous dopant distribution that can hinder charge transport between conductive domains. To verify this hypothesis, I calculated the transport barrier W_γ from the relationship $\sigma_{E0}(T) \propto \exp(-W_\gamma/k_B T)^\gamma$ (where $\gamma = 0.5$ for most conducting polymers) (for details, see the Supporting Information), as shown in **Figure 4.13d**[53, 57, 76]. It is known that W_γ, the activation energy between intercrystallite domains, increases as the structural disorder increases. The PCPDTSBT-Mix film exhibits a W_γ of 1.10 eV, which is considerably higher than that of the overcoated films. Thus, I can infer that the mixed films possess larger structural disorder (due to dopant aggregation) as well as slightly smaller crystalline domains than the overcoated films, as illustrated in **Figure 4.13e** and **4.13f**. For this reason, the $s = 3$ relationship in the mixed film is attributed to the extended percolation length due to structural disorder. On the other hands, the PCPDTSBT-OC and PPDT2FBT-OC films exhibit W_γ values of 0.16 eV and 0.20 eV, respectively, which are comparable to that of chemical vapor deposition (CVD)-grown PEDOT (< 0.18 eV) showing metallic behaviour[57]. This result is meaningful because a low energy barrier with a highly ordered structure can be achieved even in molecular doped polymer films using semi-crystalline polymers, a strong acceptor, and a sequential doping method.

4.8 Summary

In this work, I introduce two new polymeric systems using the semi-crystalline polymers PCPDTSBT and PPDT2FBT, which were doped by sequentially overcoating the strong electron-acceptor, and a high thermoelectric performance was demonstrated. With elaborate studies on α and PF as a function of σ based on the Kang−Snyder model, I show that the $\alpha - \sigma$ relationship follows a unique $s = 1$ curve, which is the first report among molecular doped semiconducting polymers. Moreover, through a cryogenic electrical conductivity experiment, it is confirmed that the systems with $s = 1$ exhibit charge transport close to the onset of metallicity owing to the significantly low transport barriers. In addition, I show that the PF maxima is achieved in this system when the doping state changes from non-degenerate to degenerate. Based on these results, I can suggest that the degenerately doped polymer system ($s = 1$) helps obtain a better TE performance.

Chapter 5. High TE performance in PEDOT:PSS films with improved structural connectivity

5.1 Introduction

Recently, there has been a growing interest in energy harvesting as one of environmentally sustainable energy sources to meet the world-wide demands for coping with climate change[1]. Among various energy harvesting technologies, thermoelectric generation, which can directly convert thermal energy into electricity, has been regarded as a promising energy conversion system based on semiconductors, leading to extensive research and commercial production of TE generators (TEGs) based on inorganic semiconductors[8, 13, 109]. However, their low heat-to-electricity conversion efficiency from low-temperature thermal energy that occupies about 60% of the total waste heat restricts the practical application of TEGs in our daily life. Efficient harvesting of low-temperature heat resources, such as a human body, would be a promising way of supplying electricity to low-power wearable devices and Internet of Things sensors[6, 110, 111].

For this purpose, conducting polymers are one of the most suitable materials for low-temperature TEGs owing to their inherent nature of lightweight, flexibility, low-toxicity, as well as cost-effective synthesis and solution processability[15, 43, 91]. Also, gradual development of material design and doping methods have led to the improvement of polymer film-based TE performance which is typically expressed as a power factor $PF = \alpha^2\sigma$, where α and σ are the Seebeck coefficient and electrical conductivity, respectively[20, 44, 47, 59, 62, 65]. To maximize the PF, fine-tuning of charge carrier concentration n through doping and/or de-doping with an additive is known as the key strategy because of the interplay between σ and α with respect to n[46]. However, it is not always a

straightforward proposition, because a typical doping/de-doping process can induce a structural perturbation of the polymer backbones causing an energetic disorder[58, 66, 70, 71]. This dopant-induced disorder strongly affects the charge transport in polymer films with complicating the inter-relationship among n, charge carrier mobility μ, and the other TE parameters, which makes it difficult to predict the maximum PF as a function of n[63]. Thus, as a new guiding principle to find out the optimum PF of polymer TE devices, the importance of unraveling the relation between α and σ continues to grow[68, 74, 76]. So far, a power law of $\alpha \propto \sigma^{-1/s}$ has been widely used for describing the empirical α–σ relationship in conjugated polymers, where s is determined by the degree of disorder[69, 79]. Several researchers have shown that doped semiconducting polymers empirically exhibit a power law with $s = 4$ due to the intrinsic- and/or dopant-induced disorders[24, 93]. However, this $\alpha \propto \sigma^{-1/4}$ relation is ineffective in optimizing the PF, because the PF in this case is roughly proportional to $\sigma^{1/2}$ and thus unceasingly increases with no local maximum, though it cannot be realized.

A few recent studies have suggested that the s value can be decreased more by reducing the disorder of doped polymer films[94, 95]. In particular, it is demonstrated that heavily doped semicrystalline polymeric systems follow the $\alpha \propto \sigma^{-1}$ relation with metal-like charge transport characteristics[48, 55, 56]. For instance, Takenobu et al. tuned the doping level of the doped PBTTT thin film to the degenerate state by electrolyte gating, and showed that $s = 1$ in the high-conductivity region[79]. I also previously reported two degenerately doped semi-crystalline polymer films exhibiting the empirical relation of $\alpha \propto \sigma^{-1}$, and proved that they necessarily have a higher PF than non-degenerately doped polymer films with higher s values[55]. In both research, the films possess high crystallinity and long-range connectivity that can facilitate delocalized charge transport. One figure that deserve to be highlighted from previous works is that a polymer system exhibiting the $\alpha \propto$

σ^{-1} relation obviously presents a maximum *PF* point that can be readily predicted from the α–σ relationship[55, 79]. It implies that the highest *PF* in such a polymer system (*i.e.*, $s = 1$) can be more easily obtained with less endeavors for optimization of experimental conditions.

Among a few polymers with high crystallinity, PEDOT:PSS has been investigated the most, because of its high tunability in its electronic state and microstructure through various treatment methods using organic solvents, surfactants, salts and acids[30, 40, 84]. The σ of a PEDOT:PSS film reaching ~4000 S cm^{-1} is incomparably higher than other solution-processable polymers, and its metal-like charge transport behavior enables the development of high-performance TE devices with low output impedance[112, 113]. To enhance the *PF* of PEDOT:PSS films, there have been several attempts that can increase α by adjusting the electronic state of PEDOT:PSS using a reducing agent, such as sodium hydroxide[29, 33], sodium borohydride[36], and hydrazine[41]. However, these reducing agents not only disturb the microstructure during permeation but also remain oxidized counterions in between the PEDOT chains which can act as a scattering center[29, 36, 41]. Thus, until now, only a few of PEDOT:PSS-based TE devices have shown a high *PF* accompanied by the $s = 1$ feature[74, 76], meaning that the TE performance of PEDOT:PSS films can be further improved.

Here I demonstrate a solution-processed, high-performance TE device based on a PEDOT:PSS thin film, which exhibits the $\alpha \propto \sigma^{-1}$ relation. I first fabricated a highly conductive PEDOT:PSS films using a strong acid, trifluoromethanesulfonic acid (TFSA), in which the σ values increased up to ~3600 S cm^{-1} owing to the highly ordered microstructure with PSS removal. Because the residual triflate anion from TFSA stably interacted as an electrostatic counterion to positively charged PEDOT, the PEDOT:PSS–TFSA film presented no significant deterioration of crystallinity during a consecutive reduction process for *PF*

optimization. As a result, a solution-processed PEDOT:PSS film exhibited a high *PF* of 534 μW $m^{-1}K^{-2}$ and a delocalized metal-like charge transport property. However, this empirical maximum *PF* was lower than our theoretic expectation, implying the existence of additional limiting factors. The fundamental cause of the *PF* limitation was found to originate from the increased conformational disorder by analyzing the temperature-dependent σ, Hall effects, and magnetoconductance of the films. I believe that our strategies to improve the TE performance and the findings on the origin of the *PF* limitation would contribute to the development of an advanced polymer systems for high-performance TEGs as well as the fundamental understanding on polymer-based TE devices.

5.2 Optimization of the TE performance

To enhance σ of the pristine PEDOT:PSS film, I introduced TFSA (CF_3SO_3H) as a post-treatment agent, which can more effectively protonate PSS (R-$SO3^-$) and remove excess PSSH owing to its relatively strong acidity ($pK_a = -14.7$) in comparison with other acids[37, 38]. Also, the triflate anion ($CF_3SO_3^-$, as a conjugate base of TFSA) can form stable electrostatic interaction with positively charged PEDOT, partially resulting in a complex form of $PEDOT^+$ and $CF_3SO_3^-$[38]. This is analogous to the molecular structure of PEDOT:trifluoromethanesulfonate (PEDOT:OTf) which is known to have an excellent TE performance and a metallic behavior with high crystallinity[32, 42, 114]. Contrary to the solution-processible PEDOT:PSS, however, insoluble PEDOT:OTf needs to be synthesized to a solid state via in situ polymerization of 3,4-ethylenedioxythiophene (EDOT) with $Fe(OTf)_3$, limiting the processibility (e.g., substrate, patterning) and scalability for its practical use. Meanwhile, our PEDOT:PSS–TFSA can be easily formed in a series of solution processes, which potentially enables the fabrication on any substrates in a variety of shapes and sizes suitable for its application. Also, I can expect the

PEDOT:PSS–TFSA film to have superb thermoelectric and charge transport properties by taking advantages of the triflate anions.

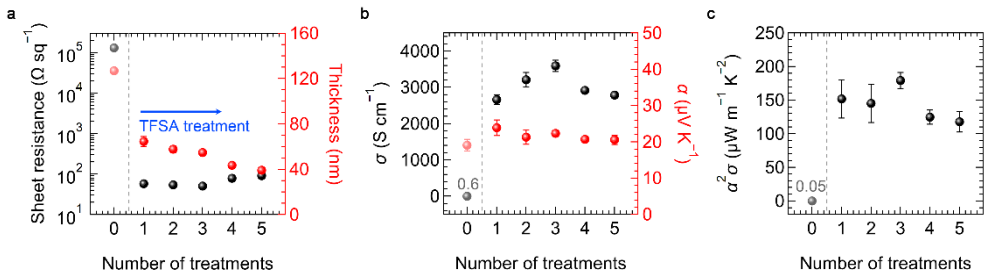

Figure 5.1 Optimization of TE performance through super-acid treatments. (a) sheet resistance and thickness, b) σ and α, and c) $\alpha^2\sigma$ of PEDOT:PSS-TFSA films according to the number of treatments.

The PEDOT:PSS–TFSA films were prepared through the TFSA immersion treatment, as described in the experimental section. Based upon optimization of the treatment conditions (**Figure 5.1**), σ was dramatically improved from 0.6 S cm^{-1} in the pristine PEDOT:PSS film to 3595 S cm^{-1} in the PEDOT:PSS–TFSA film. Such a high σ in PEDOT:PSS can be achieved by the increment of the polaron (~900 nm) and bipolaron states (over 1300 nm) confirmed in UV-vis-NIR absorption spectra (**Figure 5.2**) and morphological rearrangement of the core–shell-like PEDOT:PSS structure into the well-aligned fiber-like PEDOT chains with partial removal of PSS[39], as illustrated in **Figure 5.3a**.

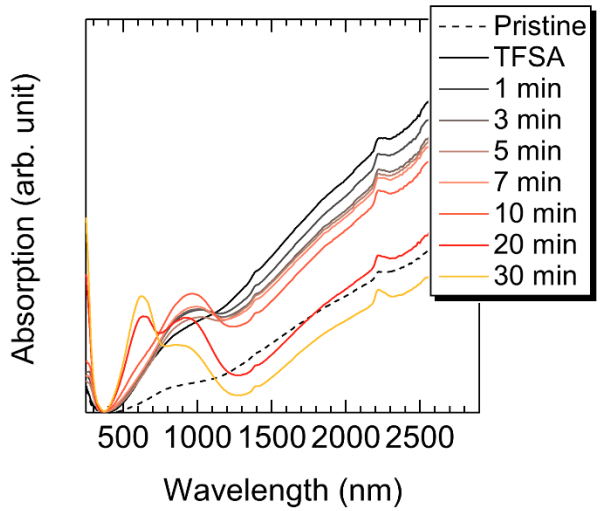

Figure 5.2 Effects of the acid-base treatments on the electronic structure of the films. UV–Vis–NIR absorption spectra of the pristine and PEDOT:PSS–TFSA films with different TDAE treatment time. The spectral intensity around at 620 nm, 900 nm, and 1300 nm indicates the neutral, polaron and bipolaron states in the PEDOT chains, respectively.

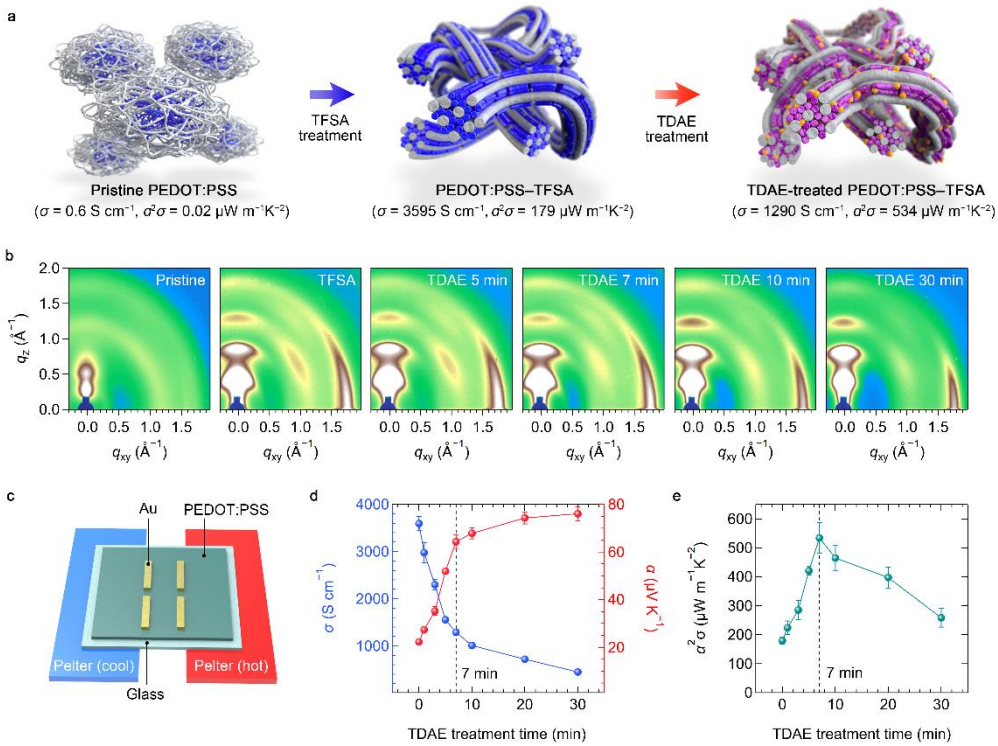

Figure 5.3 Thermoelectric and structural properties of TDAE-treated PEDOT:PSS–TFSA films. (a) Schematic illustrations of PEDOT and PSS networks in the pristine, PEDOT:PSS–TFSA, and TDAE-treated PEDOT:PSS–TFSA films. (b) Two-dimensional GIWAXS patterns of the films along with the TDAE-treatment time. (c) Illustrative structure of the TE devices and measurement. Thermoelectric performance of the PEDOT:PSS–TFSA films in terms of (d) σ, α, and (e) *PF* as a function of the TDAE-treatment time.

To verify the formation of the fibrous crystalline PEDOT network in the PEDOT:PSS–TFSA film, I investigated the 2D grazing incident wide angle X-ray scattering (GIWAXS) pattern, as shown in **Figure 5.3b**. Contrary to the pristine film, strong consecutive (*l*00) diffraction peaks are appeared in the PEDOT:PSS–TFSA films, which is attributed to the alternating lamellar spacing between PEDOT and PSS chains along the out-of-plain direction (q_z = 0.47, 0.91, and 1.34 Å, respectively)[81]. In addition, a strong (020) diffraction peak can be also observed

along the in-plain direction (q_{xy} = 1.82 Å), which corresponds to the edge-on oriented π–π stacking between PEDOT chains. This alignment of the PEDOT chains is beneficial for achieving high TE performance by facilitating the intra- and/or inter-chain charge transport. The TE properties of the films were characterized with a customized setup illustrated in the **Figure 5.3c**. The PEDOT:PSS–TFSA film with the highest conductivity (3595 S cm^{-1}) exhibited α of 22.3 μV K^{-1}, and the resultant *PF* of 179.5 μW m^{-1} K^{-2} (**Figure 5.1c**).

To further increase the *PF* by modulating the doping level of the PEDOT:PSS–TFSA film, I adopted tetrakis(dimethylamino)ethylene (TDAE) as a reducing agent which has a high reducing potential[28, 31]. Here, I used TDAE-vapor treatment to minimize the deterioration of the film morphology. The oxidation level of the PEDOT:PSS-TFSA films was successfully controlled by varying the TDAE treatment time, which was confirmed by the consistent reduction of the bipolaron states (over ~1300 nm) and decrease of the work functions observed by UV–vis absorption spectra (**Figure 5.2**) and Kelvin probe force microscopy (KPFM), respectively (**Figure 5.4a, and 5.4b**). This was further supported by observation of the XPS spectra as shown in **Figure 5.5**. The PEDOT peaks (162–166 eV) consistently shifted to lower binding energy as a function of the TDAE treatment time, indicating that the sulfur atoms of the PEDOT accepted electron from TDAE (**Figure 5.5**).

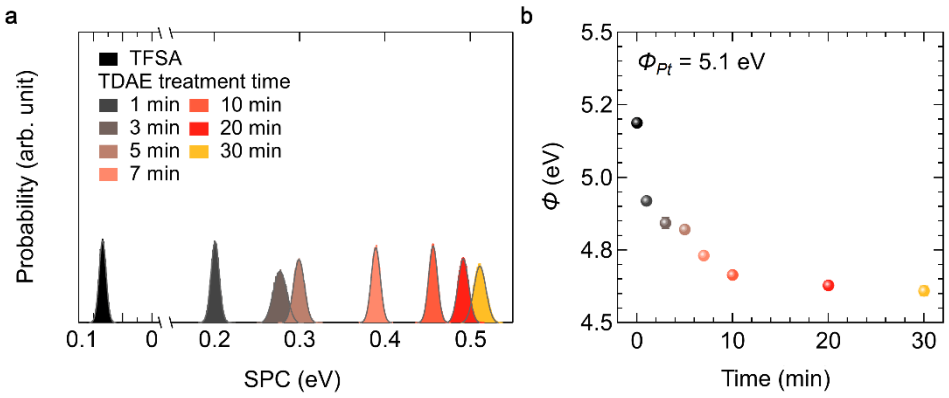

Figure 5.4 Effects of the acid-base treatments on the electronic structure of the films. (a) The SPC histogram and (b) work functions of the pristine and PEDOT:PSS–TFSA films with different TDAE treatment time. The work functions were extracted by fitting the SPC spectra using Gaussian function.

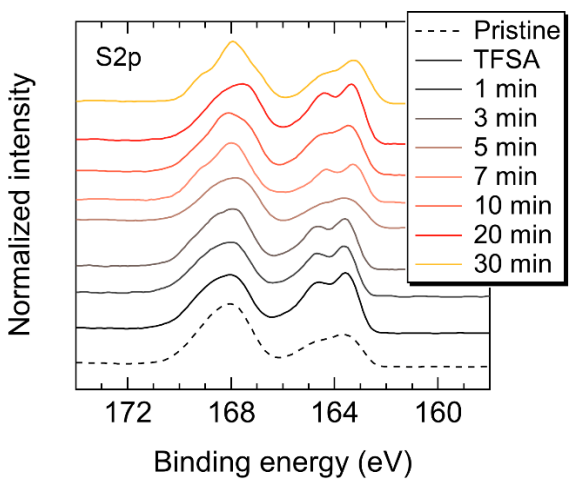

Figure 5.5 Effects of the acid-base treatments on the chemical structure of the films. S2p XPS spectra of the pristine and PEDOT:PSS–TFSA films with different TDAE treatment time. Two S2p peaks were observed in the regions of 162–166 eV and 167–172 eV, which are corresponding to thiophene of PEDOT and sulfonic acid of PSS [43]. After TFSA immersion treatment, the relative peak intensity of PEDOT to PSS noticeably increase, indicating the removal of PSS from PEDOT:PSS film.

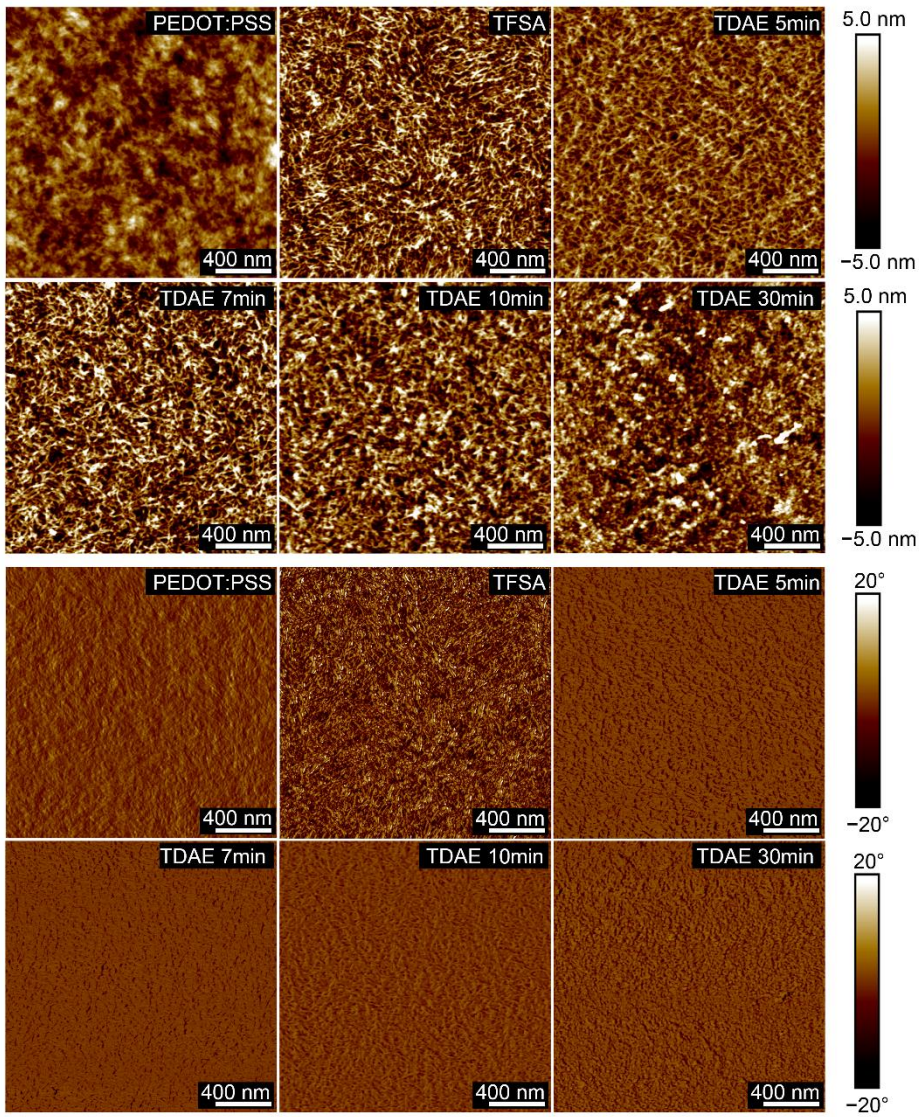

Figure 5.6 Morphological characteristics of the PEDOT:PSS films. 2 μm by 2 μm AFM topography and phase images of the PEDOT:PSS films.

Notably, the morphology of fibrous PEDOT:PSS networks and the structural order of PEDOT chains were well preserved after the de-doping process, verified with the atomic force microscopy (AFM, see **Figure 5.6**) and the GIWAXS data (**Figure 5.3** and **Figure 5.7**). When the TDAE treatment time was increased, the lamellar stacking distance consistently increased from 13.3 Å (q_z = 0.47 Å^{-1} for 0

min) to 14.5 Å (q_z = 0.43 Å^{-1} for 30 min), while the π–π stacking distance almost unchanged (~3.4 Å) as a function of treatment time (**Table 5.1**). These results suggest that the TDAE molecules mainly locate between PEDOT and counterions, only expanding the lamellar spacing while keeping the π–π stacking of PEDOT chains (**Figure 5.8**, See packing illustration of PEDOT:PSS–TFSA in the section S3). This arrangements of the cation state of TDAE (TDAE$^+$) could be attributed to the relative higher affinity of the TDAE$^+$ to PSS than PEDOT[80]. I found that there is no peak splitting or significant broadening in both the in-plain and the out-of-plain directions, indicating that the original lamellar structure and the molecular arrangement in the edge-on orientation are strongly maintained over the entire de-doping range. This can be also supported by the fact that the calculated crystal coherence length (CCL), particularly for the *π–π* stacking, exhibits little change after de-doping (~1.3 Å). Overall, I could conclude that the TDAE treatment was beneficial for controlling the electronic state of the PEDOT:PSS–TFSA films without significantly changing the morphological and structural characteristics. As plotted in **Figure 5.3d** and **5.3e**, an optimized TDAE treatment (7 min) resulted in a decrease of σ from 3595 S cm^{-1} to 447 S cm^{-1} and an increase of α from 22.3 μV K^{-1} to 76.1 μV K^{-1}, leading to achieve a superb *PF* of 534.5 μW m^{-1} K^{-2}, which is one of the highest performances of the conjugated polymers.

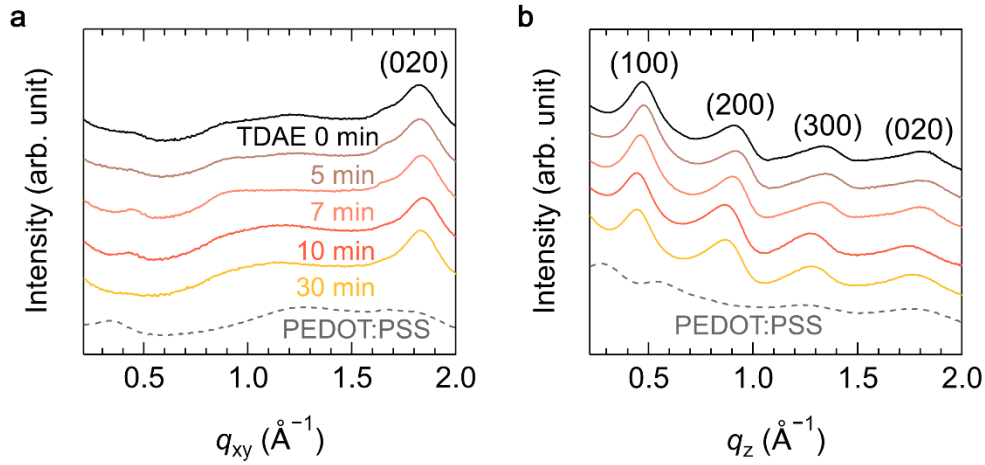

Figure 5.7 Line-cut profiles obtained from 2D GIWAXS patterns of (a) q_{xy} and (b) q_z direction of the PEDOT:PSS and PEDOT:PSS–TFSA films as function of TDAE treatment time. The pristine PEDOT:PSS film showed characteristic peaks at $q \approx 0.27$ Å^{-1}, 0.51 Å^{-1}, 1.19 Å^{-1}, and 1.80 Å^{-1} at q_z direction, which are corresponding to lamellar stacking of PEDOT and PSS, amorphous halo of PSS, and π-π stacking of PEDOT [(020) planes of PEDOT], respectively.

Table 5.1 Information on the diffraction peak parameters derived from GIWAXS data. The values of crystal coherence length were calculated using the Scherrer formula.

Films	De-doping time	q_z(100)			q_{xy}(010)		
		q ($Å^{-1}$)	d-spacing (Å)	CCL (Å)	q ($Å^{-1}$)	d-spacing (Å)	CCL (Å)
Pristine	-	0.27	22.50	35.56	1.75	3.59	16.44
PEDOT:PSS –TFSA	0 min	0.47	13.34	52.35	1.82	3.44	38.98
	5 min	0.48	13.21	49.38	1.83	3.43	39.22
	7 min	0.46	13.66	49.61	1.84	3.42	37.49
	10 min	0.45	14.07	44.19	1.84	3.42	37.23
	30 min	0.43	14.46	41.44	1.82	3.44	37.66

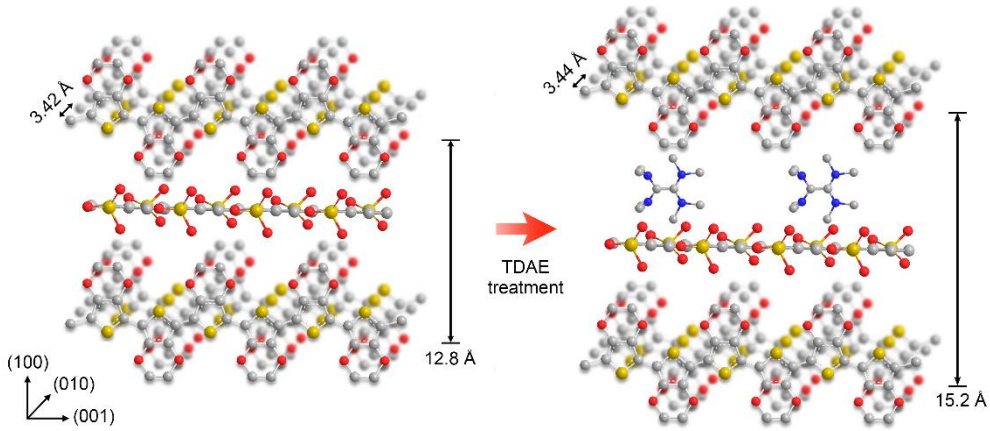

Figure 5.8 Illustration of packing arrangement. Lamellar stacking of PEDOT:PSS-TFSA (left image) and of TDAE treated PEDOT:PSS-TFSA where TDAE is located between PEDOT and PSS (right image).

5.3 Analysis of the TE relationships using transport model

To find the origin of outstanding TE performance of our films, I investigated the α–σ and PF–σ relationships using the Kang–Snyder (K-S) model. Among various transport models[74, 76, 94, 95], this model was adopted because it allows to not only understand the charge transport behaviors but also predict a theoretical PF maximum simply from the experimental data of α and σ. The pairs of σ and α can be fitted through the transport coefficient σ_{E0} and transport parameter s, both of which are the essential fitting parameters constituting the transport function of this model (see the section S4)[76, 83]. The σ_{E0} represents the intrinsic carrier mobility, which is determined by the structural connectivity of the polymer. This value is known to be independent of the chemical potential of the polymer and reflects the degree of percolation between conductive domains. The s is a component that determines the energy dependency of the transport function, representing the charge transport mechanism of the system. It has been known that the value of s is affected by the microscopic transport properties (*i.e.*, scattering mechanism, local density of states, and relaxation time) of carriers within an individual crystalline polymer domain[21, 75].

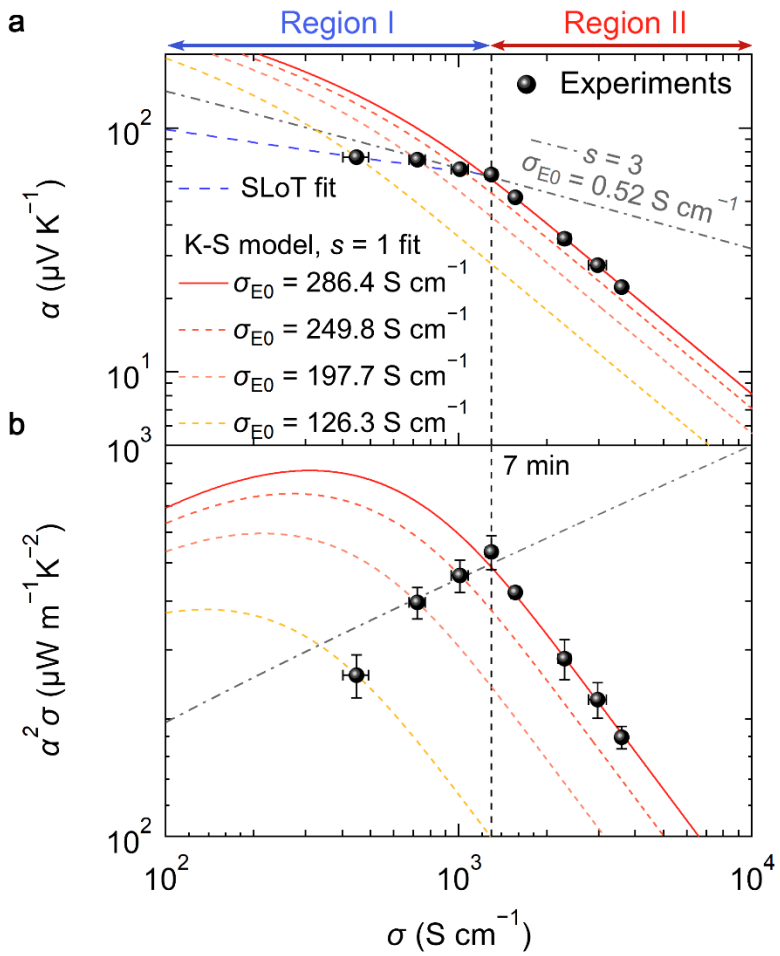

Figure 5.9 Seebeck coefficient and power factor of the TDAE-treated PEDOT:PSS–TFSA films as a function of electrical conductivity. (a) The α–σ and (b) $\alpha^2\sigma$–σ relations of the films are obtained by fitting experimental data to the SLoT and K–S models with various σ_{E0} and s. The vertical line represents the transition point at which the power law of the α–σ changes.

As shown in **Figure 5.9a**, the s = 1 (σ_{E0} = 286.4 S cm^{-1}) line well fits the experimental data in the high conductivity regime, specifically, when σ > 1289.6 S cm^{-1} (Region II) as indicated by a vertical dashed line. The good fit for s = 1 indicates that the transport function is linearly proportional to the energy of the carrier (see the section S2), which has recently been regarded as the signature for the delocalized

charge transport[79]. Most doped semiconducting polymers showing thermally activated hopping transport exhibits the stronger energy dependency of the transport function (*i.e.*, $s = 3$ or 4) with much lower σ_{E0} (0.001 S cm^{-1} to 0.01 S cm^{-1})[53, 68, 76]. The much higher value of σ_{E0} reaching 286.4 S cm^{-1} reflects the outstanding intrinsic carrier mobility of our PEDOT:PSS systems, which may be resulting from the superb interdomain charge transport between PEDOT domains[57]. These unique behaviors, which has not been reported for the solution-processed PEDOT:PSS systems, well maintained with the TDAE-treated films for 7 min, resulting in the high *PF* (534.5 μW m^{-1} K^{-2}).

On the other hand, the samples at lower σ regime (< 1289.6 S cm^{-1}) (Region I) deviates from the $s = 1$ relation with $\sigma_{E0} = 286.4$ S cm^{-1}. This deviation suggests a change in charge transport for our system as it cannot be described with unique transport function (σ_{E0} and s). To support the transition in transport behavior as a function of σ, I applied the Semi-localized transport model[74] to our data (blue dashed line in **Figure 5.9a**) and investigated the value of the localization energy W_H which is an essential parameter that constitutes the transport function of the SLoT model (See the section S3, **Figure 5.10**, and **Table 5.2**). It is notable that the localization energy W_H, which shows almost constant value of zero, abruptly increases when the de-doping time exceeds 7 min. The increase in W_H indicates that the Arrhenius-like hopping contribution of charge carriers increases, which well supports the transition transport behavior as a function of σ. Additionally, this transition prevents from reaching the theoretic maximum *PF* of 863.5 μW m^{-1} K^{-2}, as shown in **Figure 5.9b**. To explain the origin of the *PF* limitation, I can suggest two possibilities using the K–S model—one is the occurrence of the metal-to-insulator transition—and the other is the decrease in the degree of percolation. Either of which is reflected by the change in s value from $s = 1$ to $s = 3$ (grey dash-dotted line in **Figure 5.9a**), or gradual left shift of the $s = 1$ curve accompanying decrease

in σ_{E0} (dashed lines in **Figure 5.9a**), respectively. The former, metal-to-insulator transition has been reported in ion-gel gated PBTTT films[79], which well explains the origin of change in *s*. The latter, the decrease in degree of percolation between PEDOT domains, is also reasonable speculation in our case, because the de-doped films still exhibit high σ (447.3–1289.6 S cm^{-1}) and there were no significant structural changes in GIWAXS. In the following section, I intend to systemically investigate which factors (*i.e.*, insulator to metal transition and/or decrease in percolation) acted dominantly on the *PF* limitation by analyzing the temperature-dependent σ ($\sigma(T)$) and Hall effect measurements that enable to observe the electronic states of the films.

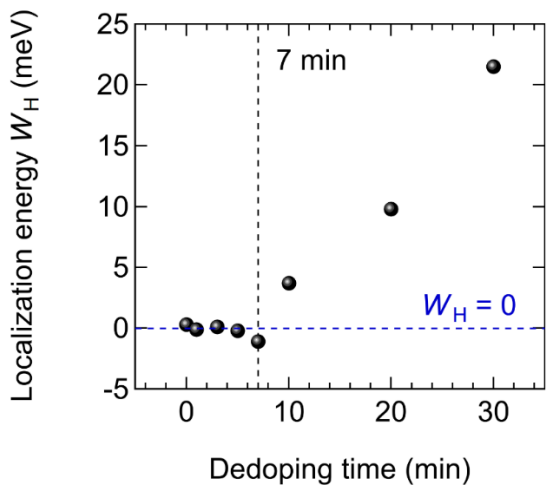

Figure 5.10 Change in localization energy W_H as a function of TDAE de-doping time. The values of W_H of the PEDOT:PSS films were extracted by the SLoT model. When the W_H converges to zero, the transport function of SLoT model equals to the s = 1 case of the K–S model.

Table 5.2 SLoT modelling and material parameters for the $\eta(c)$ and $W_H(c)$ relationships.

Films	c_{max}	A_0	A_1	$W_{H,max}$ **(meV)**	$W_{H,slope}$ **(meV)**	M_0 **(gmol^{-1})**	N	ρ **(gcm^{-1})**	k_BT **(meV)**
PEDOT:PSS –TFSA	0.5	0.2	6	710	1200	142	1.0	1.0	25.88

5.4 Temperature-dependent electrical characterizaions

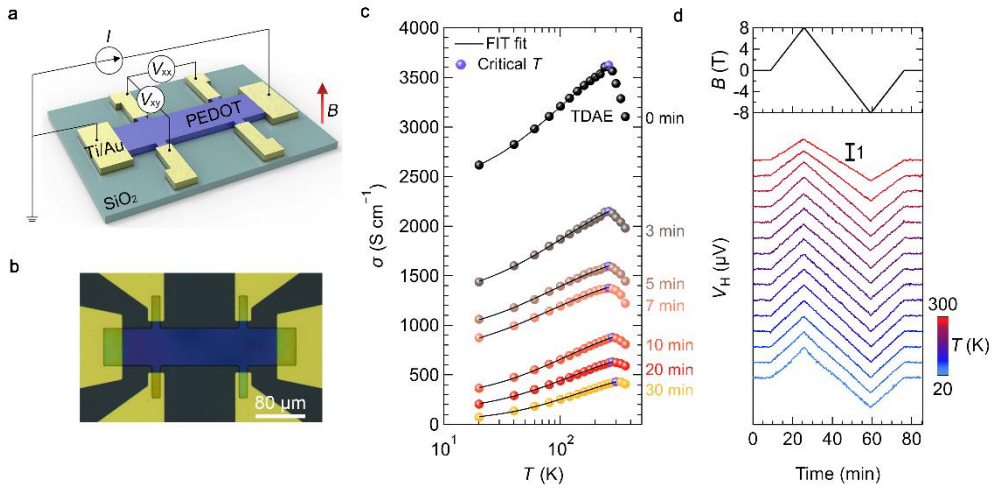

Figure 5.11 Characterization of charge transport properties of PEDOT:PSS–TFSA films depending on TDAE treatment. (a) Schematic illustration of the Hall bar measurement and (b) its optical micrograph image of the device. The longitudinal (V_{xx}) and transverse voltages (V_{xy}) were recorded simultaneously by applying a constant dc current (I). (c) The temperature-dependent σ as a function of de-doping time. The FIT model well fits the experimental data at T below the critical temperature. (d) The Hall voltage when the B field was ramped up to 8 T and then down to −8 T at various temperatures from 20 K to 300 K. The scale bar represents 1 μV.

Figure 5.11a and **5.11b** shows the PEDOT:PSS films fabricated with Hall bar geometry, which allows for the simultaneous analysis on the $\sigma(T)$ and magnetotransport measurements (see the section S4). I can observe the negative temperature coefficient of σ ($d\sigma/dT < 0$), which indicates the presence of metallic states[70, 78, 79], for the PEDOT:PSS–TFSA film above the critical temperature, as shown in **Figure 5.11c**. Interestingly, this metallic behavior ($d\sigma/dT < 0$) is still observable near room temperature even after de-doping for 30 min. Additionally, our

$\sigma(T)$ data below the critical temperature exhibit a good fit with fluctuation induced tunneling (FIT) model (**Figure 5.11c** and section S4), which is commonly used to describe the $\sigma(T)$ of highly conductive organic materials such as carbon nanotubes[88] and PEDOT derivatives[84]. The variable range hopping model that has been adopted to describe the insulating behaviors of the polymers fails to fit our $\sigma(T)$ data in any dimensions, which can be confirmed by the slope of $-1/m$ of the Zabrodskii plot (**Figure 5.12**, section S4). The delocalized charge transport of the PEDOT:PSS films is further confirmed by Hall effect measurement. As shown in **Figure 5.11d**, the PEDOT:PSS–TFSA film shows clear Hall voltage signal in a wide range of temperatures from 20 K to 300 K, indicating the metallic behavior of delocalized charge carriers. Although the sample was de-doped, a clear Hall voltage still appears, and no sign anomalies was observed (**Figure 5.13**) [73, 115]. These findings suggest that the metallic behaviors are well-maintained even after de-doping, indicating the *PF* limitation does not originate from the metal-to-insulator transition. Then, I consider the effects of the decrease in percolation on *PF* limitation by simultaneous comparison on the value of σ_{E0}, transport barrier between PEDOT domains and the charge carrier mobility μ upon de-doping.

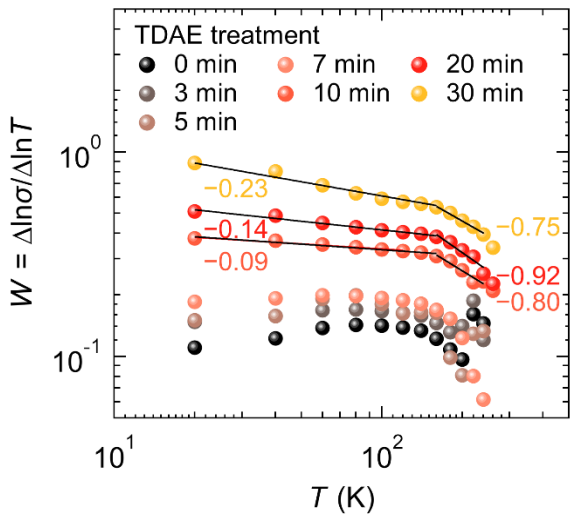

Figure 5.12 Zabrodskii plot of the PEDOT:PSS films. The slope of the fit line equals to the value of $-1/m$, which gives the information of the dimension m of the VRH mechanism.

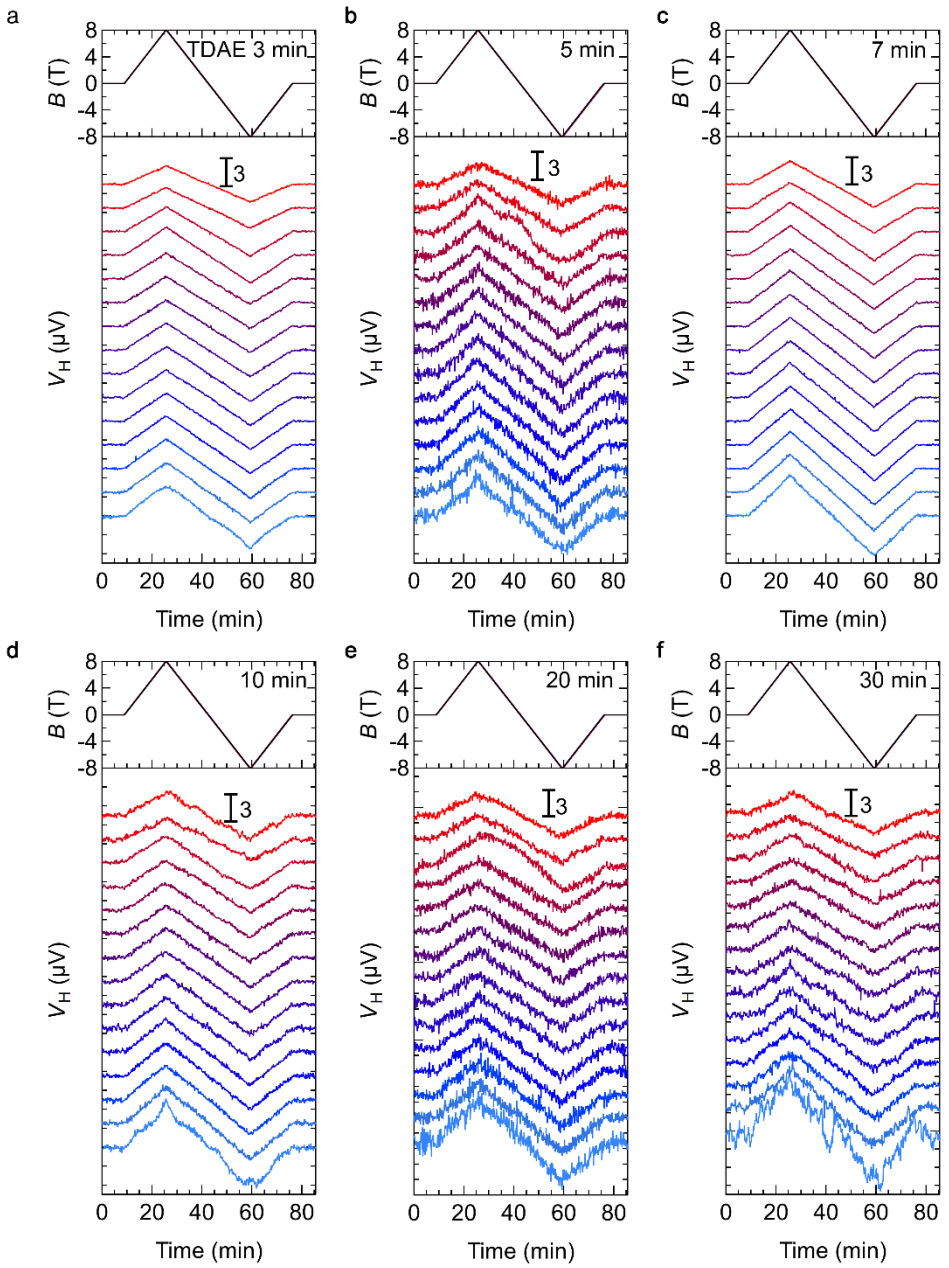

Figure 5.13 Hall effect measurements for the PEDOT:PSS films. (a-f) The extracted Hall voltages of the TDAE-dedoped PEDOT:PSS–TFSA films for 3, 5, 7, 10, 20, and 30 min, respectively, when *B* field was ramped up to 8 T and down to −8 T at various temperatures from 20 K to 300 K.

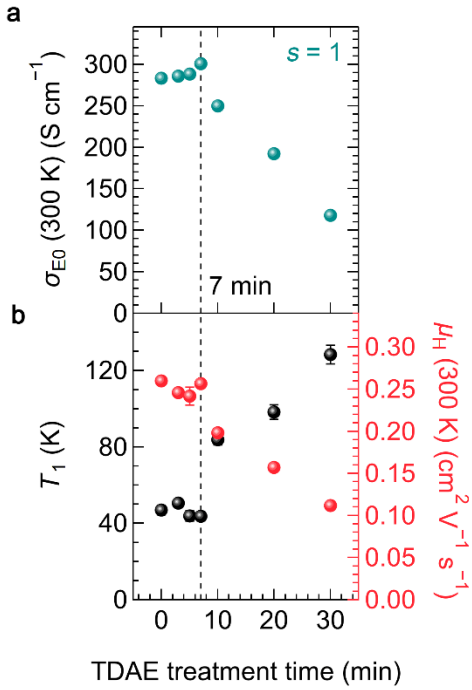

Figure 5.14 Characterization of charge transport properties of PEDOT:PSS–TFSA films depending on TDAE treatment. (a) The transport coefficient σ_{E0} of the films when s = 1. (b) The tunneling barrier T_1 and Hall carrier mobility μ_H as a function of the TDAE de-doping time.

Figure 5.14a shows the extracted σ_{E0} of each sample when the value of s is fixed to 1. I can observe that σ_{E0} is maintained by 7 min, and then decreases significantly from 300.8 to 118.3 S cm^{-1} when de-doping time exceeds 7 min. Since the decrease in σ_{E0} indicates that the charge transport between PEDOT domains becomes poorer, the transport barrier between PEDOT domains and/or charge carrier mobility could be significantly changed. To observe this, I first obtained the tunneling barrier between conductive domains (T_1) by extracting the fitting parameters from the FIT model: $\sigma = \sigma_0 \exp[-T_1/(T+T_0)]$, where σ_0, T, and T_0 are the σ at infinite T, absolute temperature, and the characteristic temperature, respectively (**Table 5.3**) [17, 22, 84]. **Figure 5.14b** shows T_1 and μ_H as a function of the de-doping

time.Furthermore, I also calculated the carrier mobility μ_H and carrier concentration n of the PEDOT:PSS films using Hall effect measurement at room temperature (**Figure 5.15).** The simultaneous comparison of effect of de-doping on T_1 and μ_H enables to understand how the charge transport between conductive domains changes, which helps to explain the behavior of σ_{E0}. The value of T_1 and μ_H, which maintained almost the same values, significantly changes when the de-doping time exceeded 7 min; the T_1 increases from 43.7 to 128.4 K, and μ_H decreases from 0.26 to 0.11 $cm^2\ V^{-1}\ s^{-1}$. It is particularly striking that the turn-over points of them is the same as those of σ_{E0}. This is a strong indication that the percolation between PEDOT domains is suppressed as the de-doping time exceeds 7 min, which prevents to achieve higher *PF* predicted theoretically. In the following section, I further verify and elaborate our suggestions on the origins of *PF* limitation by probing the charge carrier scattering in a local area via longitudinal magnetoconductance (MC) measurements.

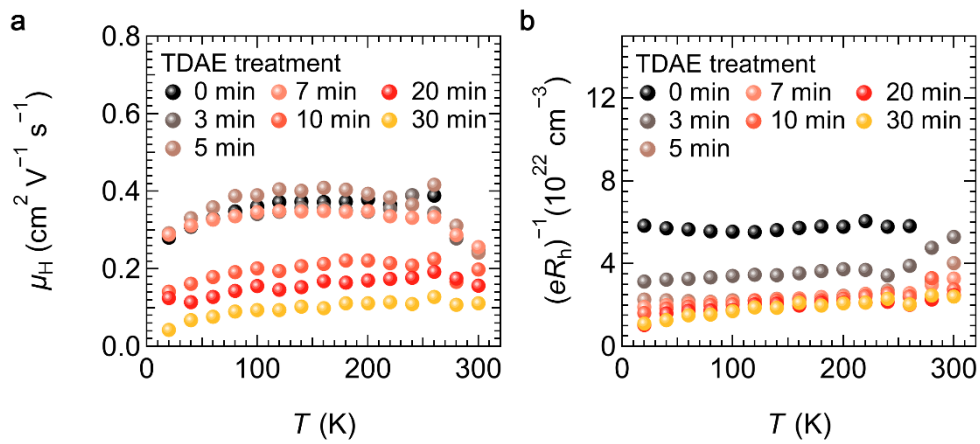

Figure 5.15 Electrical parameters of PEDOT:PSS films extracted from Hall effect measurement. (a) Temperature-dependent electrical mobility μ_H and (b) carrier concentration $(eR_H)^{-1}$.

Table 5.3 Calculated σ_0, T_0, and T_1 of PEDOT:PSS–TFSA films as a function of TDAE de-doping time.

Films	De-doping time (min)	σ_0 (S cm^{-1})	T_0 (K)	T_1 (K)
PEDOT:PSS–TFSA	0	4150.5 (± 27.6)	81.8 (± 4.4)	46.9 (± 2.5)
	3	2503.3 (± 16.0)	72.3 (± 3.5)	50.6 (± 2.3)
	5	1836.3 (± 15.8)	59.4 (± 4.3)	43.9 (± 2.8)
	7	1593.3 (± 12.2)	52.7 (± 3.4)	43.7 (± 2.3)
	10	1130.1 (± 9.4)	55.3 (± 2.4)	83.8 (± 2.8)
	20	852.4 (± 9.7)	50.4 (± 2.7)	98.3 (± 3.8)
	30	629.3 (± 9.1)	42.4 (± 2.7)	128.4 (± 4.9)

5.5 Analysis of the magnetoconductance

As shown in **Figure 5.16a**, the PEDOT:PSS–TFSA film exhibits a positive MC—the conductance increases when a magnetic field B is applied perpendicular to the samples. The positive MC can be explained by the magnetic-field-induced suppression of the weak localization effect which is originating from the quantum interference of coherently backscattered electron waves[34, 71, 116]. I can observe that the magnitude of MC gradually decreased as the T increased, and becomes almost independent on the B-field as the T approaches to 300 K. This result may be attributed to the crossover of the conduction mechanism from FIT to the effective metallic regime as discussed with $\sigma(T)$. The similar phenomena can be observed from all de-doped films (**Figure 5.16b, 5.16c** and **Figure 5.17**), and there is no sign of magnetic-field-induced localization (*i.e.*, negative MC)[70], which allows to conclude that there is no change in conduction mechanism upon de-doping.

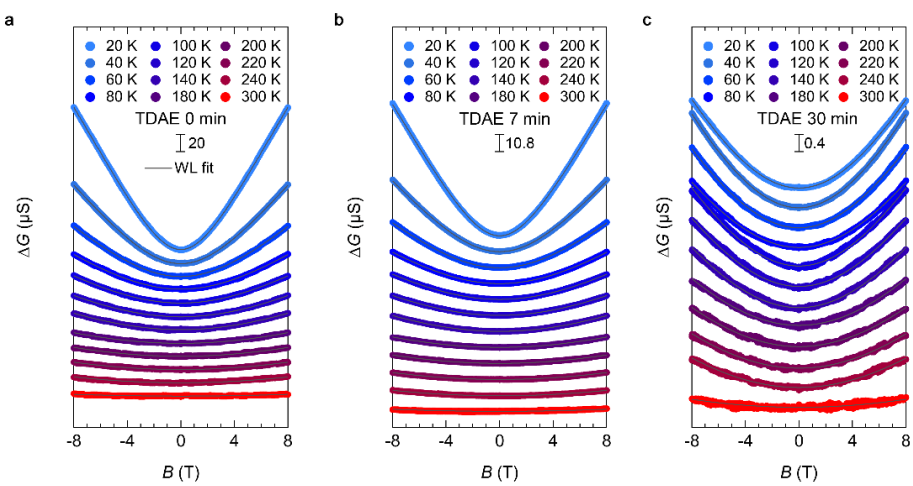

Figure 5.16 Weak localization in the magnetoconductance of the PEDOT:PSS–TFSA films as a function of the TDAE treatment time. Effect of B field applied perpendicular to the substrate on differential conductance ($\Delta G = G(B) - G(0)$) of the TDAE-treated PEDOT:PSS–TFSA films at a various temperature; (a) 0 min, (b) 7 min, and (c) 30 min, respectively.

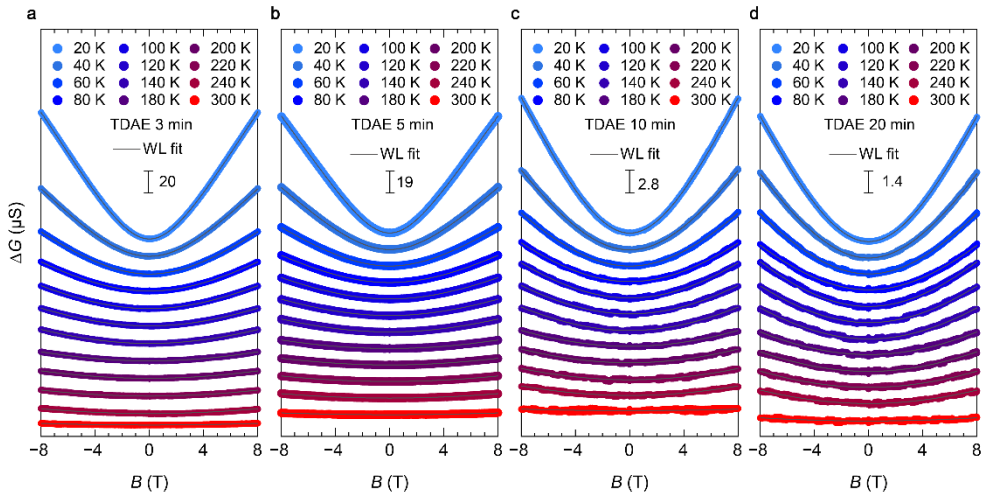

Figure 5.17 Weak localization in the magnetoconductance of the TDAE-treated PEDOT:PSS–TFSA films. Effect of *B* field applied perpendicular to the substrate on differential conductance ($\Delta G = G(B) - G(0)$) of the TDAE-treated PEDOT:PSS–TFSA films at a various temperature; (a) 3 min, (b) 5 min, (c) 10 min, and (d) 20 min, respectively.

I further analyze the MC data with 2D Hikami–Larkin–Nagaoka model[117] to confirm the local carrier scattering mechanism which is directly related to the transport parameter *s* (see section S7)[76, 82, 85]. It has been known that the acoustic phonon scattering corresponds to the $s = 1$, while the impurity scattering corresponds to the $s = 3$[76, 85]. Proving that the scattering mechanism remains constant can serve as compelling evidence for supporting our argument by showing the constancy of *s*. The *B* dependence of the conductance increment $\Delta G(B) = G(B) - G(0)$ can be written as,

$$\Delta G(B) \propto -\frac{e^2}{2\pi^2\hbar}\left[\ln\frac{B_\varphi}{B} - \Psi\left(\frac{1}{2}+\frac{B_\varphi}{B}\right)\right] \quad (10)$$

where $\hbar$ is the plank constant, B_φ is the characteristic magnetic field required to destroy phase coherence, and Ψ is the digamma function. This model well fits the magnitude and curvature of our MC data, which enables to determine the fitting parameter $B\varphi$ (**Figure 5.18**). The phase-breaking time τ_φ and phase coherence length $\lambda\varphi$ were calculated using, $B_\varphi = \hbar/4qD\tau\varphi$, and $\lambda_\varphi = (D\tau_\varphi)^{1/2}$, respectively, where *D*, k_B, and *q* are the diffusion coefficient ($D = \mu_H k_B T/q$), Boltzmann constant and unit charge, respectively. The physical meaning of τ_φ and λ_φ is the time and distance at which a charge can propagate between inelastic collision by scattering centers while maintaining phase coherence, respectively. I can understand the scattering mechanism of the PEDOT:PSS films by interpreting the value of *p*, which is an index determining the *T* dependence of τ_φ as $\tau_\varphi \propto T^{-p}$ (**Figure 5.19**)[118]. For electron-phonon scattering, $p = 3$, and for electron-electron scattering, $p = 1.5$ (dirty limit) or $p = 2$ (clean limit) is expected. As shown in **Figure 5.19a**, all the samples show *p* values between 1.6 and 1.8, indicating that the electron-electron scattering is dominant. As the de-doping level increases, the carrier scattering mechanism is maintained, which firmly reconfirmed our suggestion that the value of *s* remains constant.

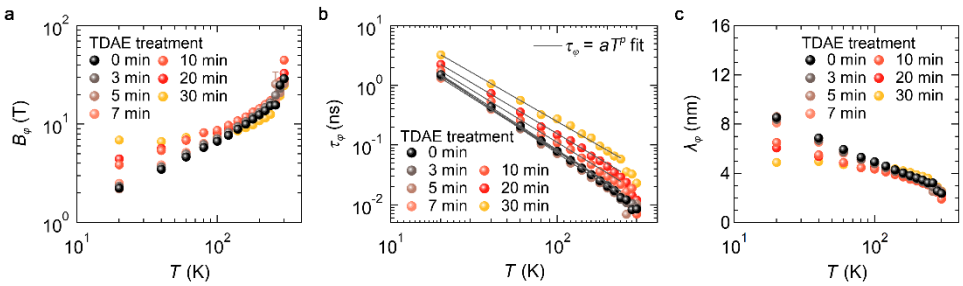

Figure 5.18 Inelastic scattering characteristics of the PEDOT:PSS–TFSA films as a function of TDAE treatment time. Temperature-dependent (a) characteristic field B_φ, (b) phase-breaking time τ_φ, and (c) inelastic scattering length λ_φ. The values of B_φ were extracted by fitting the differential conductance ΔG versus B of the PEDOT:PSS films using 2D HLN model. The scattering parameter p was determined by interpreting the T dependency of the phase-breaking time τ_φ.

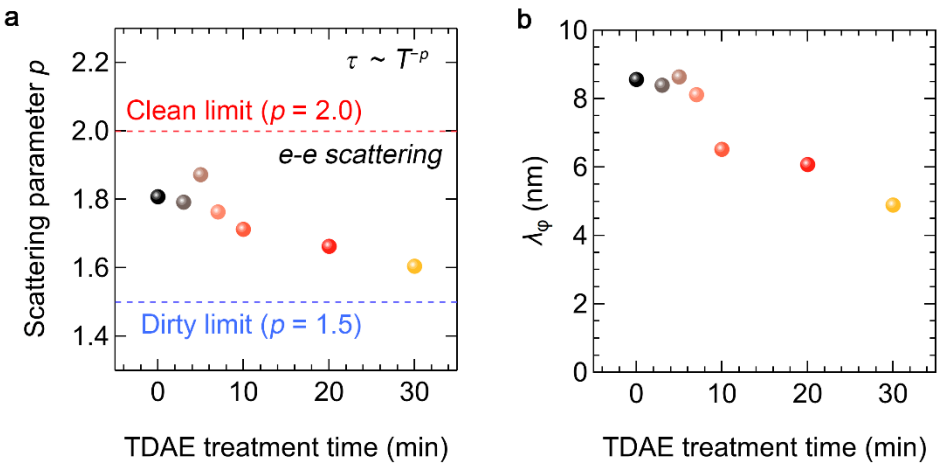

Figure 5.19 Scattering parameter of the PEDOT:PSS–TFSA films as a function of TDAE treatment time. (a) Scattering parameter p extracted by fitting the τ–T relationship. The electron-electron scattering mechanism was observed for all the films. (b) inelastic coherence length λ_φ as a function of de-doping time.

Our assertion that the *PF* limitation originates from the degradation of percolation between the PEDOT domains can be elucidated by examining the behavior of phase coherence length λ_φ, which refers to the maximum physical distance that charges can travel while maintaining phase coherence[78]. The crystallinity that can be estimated through GIWAXS gives an information of structural ordering, but it is difficult to know how the charge propagates inside the crystallite. Indeed, I can observe that the crystalline coherence length estimated by GIWAXS is hardly changed (less than one π stack ~ 2 Å), whereas the λ_φ decreases on a much larger scale from 8 to 5 nm (~ 3 nm), which as shown in **Figure 5.19b**. The tendency of λ_φ is particularly striking, because like μ_H and T_1, it also maintained a similar value, but abruptly decreased after the de-doping time exceeds 7 min. The decrease in λ_φ indicates that the electron delocalization in individual PEDOT domains becomes weakened, leading to the degradation of macroscopic electrical connections (*i.e.*, percolation) between PEDOT domains which is reflected by the decrease in μ and the increase in T_1. The consistency in the physical significance and trends obtained from independent analyses demonstrates the clarity of our claim on *PF* limitation.

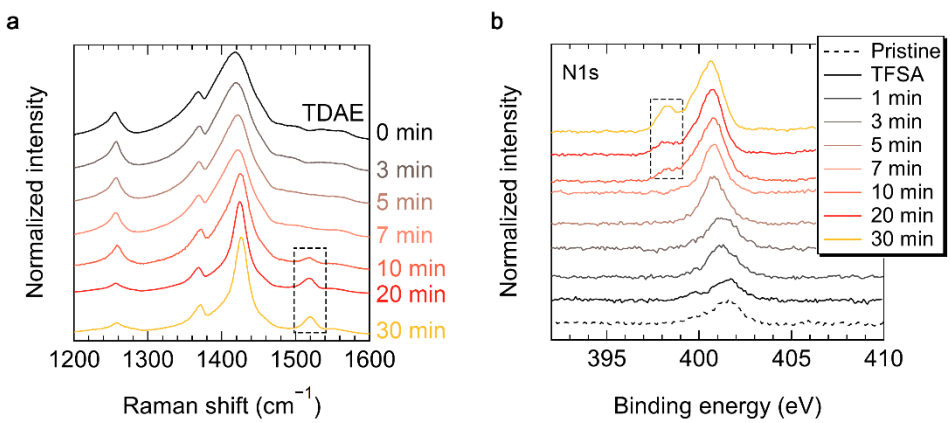

Figure 5.20 Sources for the increased density of scattering centers. (a) Normalized Raman spectra, and (b) N1s XPS spectra of the PEDOT:PSS–TFSA

films with different TDAE treatment time. The peaks corresponds to the protonated amines (401.6 eV) were observed for the pristine and PEDOT:PSS–TFSA film. As the TDAE treatment time increases, the peaks shifted to lower binding energy. When the TDAE treatment time exceeds 7 min, the peaks at 398.3 eV, which corresponds to the neutral amines, abruptly increases (marked by dotted rectangular).

The aforementioned findings prompt us to uncover the cause of the decline in λ_{φ}, which may be the fundamental origin of the *PF* limitation. The decrease in λ_{φ} suggests the increase in density of scattering centers in individual PEDOT domains that hinder the efficient long-range charge transport. Since the π-π stacking of the PEDOT chains almost unchanged as shown in the GIWAXS, I can expect that the intramolecular structure of the PEDOT altered upon de-doping. To observe this, I detected the Raman spectra of the films as shown in **Figure 5.20a**. As the de-doping time exceeds 7 min, the peak at 1500 cm^{-1} appears and becomes more pronounced after the treatment time exceeds 7 min (marked by the dotted rectangular), indicating the transformation of PEDOT chain from planar and rigid quinoid structure to less planar and flexible benzoid structure[41, 52]. This structural transformation can increase the conformational disorders, including imperfections, distortions, and stacking faults, which could function as scattering centers[78]. The remained TDAE molecules that do not participate in electron transfer may also act as scattering centers. To investigate this, I examined the N1s XPS spectra of the films as shown in **Figure 5.20b**. Notably, a peak corresponding to neutral amine (398.3 eV), which was absent, exhibits a sudden increase after the treatment times exceeds 7 min. As a result, the π-electron delocalization in both intra- and inter- PEDOT chains was degraded by these scattering centers, ultimately leading to a decline in λ_{φ}. The limitation of charge transport within the PEDOT domain (which might be corresponding to λ_{φ}) inevitably affects the macroscopic charge transport, which can be observed from the conductive AFM (C-AFM) images as shown in **Figure 5.21**.

As the de-doping time increases, not only the size of individual conductive domains (bright color) but also the contact area between them gradually decreases. Moreover, this behavior becomes prominent when the de-doping time exceeds 7 min. These results show that the electrical connection between conductive domains decreases, which is well corresponding to the analysis I conducted above. Consequently, I found that the increased scattering centers in the PEDOT domains is the fundamental origin of the PF limitation that degrades the λ_{φ}, ultimately hindering long-range charge transport.

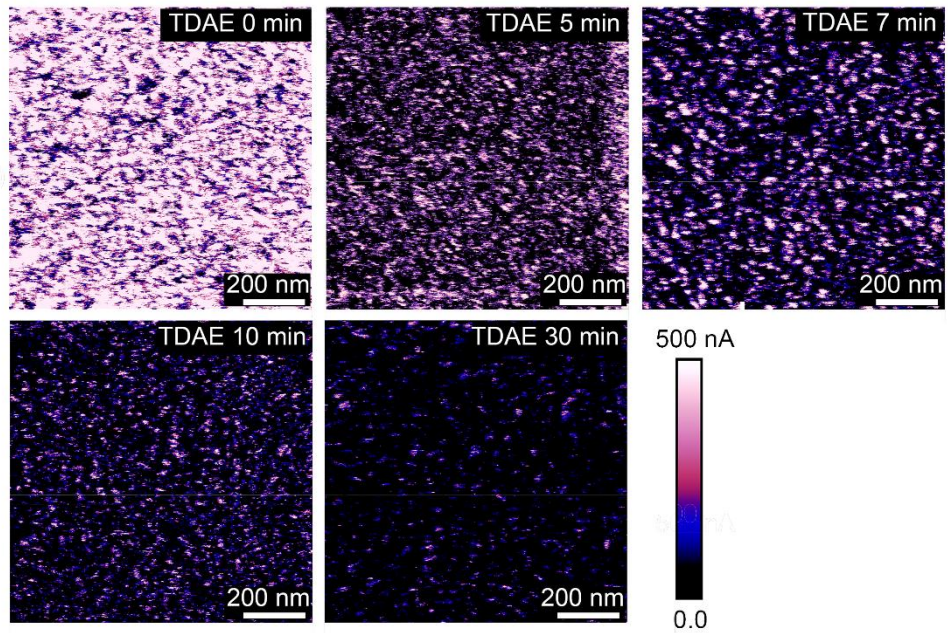

Figure 5.21 C-AFM images of the PEDOT:PSS–TFSA films as a function of TDAE treatment time. The electrical concentration between PEDOT domains abruptly degrades as the TDAE treatment time exceeds 7 min.

5.6 Summary

The present work demonstrates the solution-processable, high performance TE devices based on PEDOT:PSS thin films. Our optimized sequential treatment using super-acid and base has enabled the films have highly ordered microstructure even after the de-doping process, leading to the efficient long-range delocalized charge transport with high *PF* accompanied by the $s = 1$ relation. Theoretical analysis using K–S model shows that the *PF* did not reach the theoretical value but saturated to limited value. Through a comprehensive analysis on the structure-property relationships using non-trivial techniques including magnetotransport measurements, Raman spectroscopy and XPS, I revealed that the increase in carrier scattering within individual PEDOT domains, which originates from conformational disorders and impurities, degrades the electrical connection between PEDOT domains, preventing to achieve the theoretical *PF* maxima.

Considering the above results, I propose several key strategies to overcome the above limitations and ultimately achieve the theoretical maximum *PF*. First, high crystallinity and their structural connectivity are essential for enabling long-range delocalized charge transport. Second, reducing the density of scattering centers, such as conformational disorders or residual dopants can play a decisive role to overcome the *PF* limitation by mitigating the decrease in λ_{φ}. This can be accomplished through multilateral efforts, including removing remaining PSS and/or residual dopants, enhancing the intrachain rigidity and crystallinity of the PEDOT:PSS films, and developing a novel n-type dopant with excellent doping efficiency—capable of significantly adjusting the doping level of a polymer with even minimal quantities. Our approaches not only offer insights into the structural-property relationship of the PEDOT:PSS, but also paves the way for development of TE devices that can contribute to the future advancement of energy harvesting technologies.

Chapter 6. Conclusion

In summary, this thesis addresses the challenge of enhancing thermoelectric performance in conjugated polymer-based devices through sequential doping. This method effectively modulates the electronic structure to degenerate states without causing structural perturbations in the highly ordered microstructure of the polymer films. Consequently, it overcomes the power-law relationship between Seebeck coefficient and electrical conductivity, achieving local *PF* maxima. Various techniques including have been employed to investigate the structure-property relationships of these degenerately doped polymer systems thoroughly, providing valuable insighted into the physical origins of their unique TE behaviors.

The research presented in this thesis has far-reaching implications. It lays a solid groundwork for the development of high-performance TE devices capable of converting low-grade waste heat into electricity more efficiently. This development is critical for addressing environmental pollution and energy crises, leading to significant energy savings and reduced overall energy consumption. Additionally, the innovative methodologies used in this thesis contribute to a deeper understanding of the intricate structure-property relationships in conducting polymers. This knowledge is crucial for further advancements in the field of organic electronic and has the potential to guide the development of novel materials with improved properties.

Bibliography

[1] S. Chu, A. Majumdar, Opportunities and challenges for a sustainable energy future. *Nature* **488**, 294-303 (2012).

[2] B.-J. Lee, S.-M. Jung, J. Kwon, J. Lee, K.-S. Kim, Y.-T. Kim, Harvesting Low-Grade Waste Heat to Electrical Power Using a Thermoelectrochemical Cell Based on a Titanium Carbide Electrode. *ACS Appl. Energy Mater.* **5**, 2130-2137 (2022).

[3] Z. Bu, X. Zhang, Y. Hu, Z. Chen, S. Lin, W. Li, C. Xiao, Y. Pei, A record thermoelectric efficiency in tellurium-free modules for low-grade waste heat recovery. *Nat. Commun.* **13**, 237 (2022).

[4] P. Ziółkowski, T. Kowalczyk, S. Kornet, J. Badur, On low-grade waste heat utilization from a supercritical steam power plant using an ORC-bottoming cycle coupled with two sources of heat. *Energy Convers. Manag.* **146**, 158-173 (2017).

[5] U. Larsen, L. Pierobon, F. Haglind, C. Gabrielii, Design and optimisation of organic Rankine cycles for waste heat recovery in marine applications using the principles of natural selection. *Energy* **55**, 803-812 (2013).

[6] Y. Zhou, X. Liu, B. Jia, T. Ding, D. Mao, T. Wang, G. W. Ho, J. He, Physics-guided co-designing flexible thermoelectrics with techno-economic sustainability for low-grade heat harvesting. *Sci. Adv.* **9**, eadf5701 (2023).

[7] M. Hyland, H. Hunter, J. Liu, E. Veety, D. Vashaee, Wearable thermoelectric generators for human body heat harvesting. *Appl. Energy* **182**, 518-524 (2016).

[8] G. J. Snyder, E. S. Toberer, Complex thermoelectric materials. *Nat. Mater.* **7**, 105-114 (2008).

[9] C. Xu, Y. Song, M. Han, H. Zhang, Portable and wearable self-powered systems based on emerging energy harvesting technology. *Microsyst. Nanoeng.* **7**, 25 (2021).

[10] W. Ren, Y. Sun, D. Zhao, A. Aili, S. Zhang, C. Shi, J. Zhang, H. Geng, J. Zhang, L. Zhang, J. Xiao, R. Yang, High-performance wearable thermoelectric generator with self-healing, recycling, and Lego-like reconfiguring capabilities. *Sci. Adv.* **7**, eabe0586 (2021).

[11] Q. Zhang, K. Deng, L. Wilkens, H. Reith, K. Nielsch, Micro-thermoelectric devices. *Nat. Electron.* **5**, 333-347 (2022).

[12] F. Meng, L. Chen, Y. Feng, B. Xiong, Thermoelectric generator for industrial gas phase waste heat recovery. *Energy* **135**, 83-90 (2017).

[13] Z.-H. Zheng, X.-L. Shi, D.-W. Ao, W.-D. Liu, M. Li, L.-Z. Kou, Y.-X. Chen, F. Li, M. Wei, G.-X. Liang, P. Fan, G. Q. Lu, Z.-G. Chen, Harvesting waste heat with flexible Bi2Te3 thermoelectric thin film. *Nat. Sustain.* **6**, 180-191 (2023).

[14] F. Hao, P. Qiu, Y. Tang, S. Bai, T. Xing, H.-S. Chu, Q. Zhang, P. Lu, T. Zhang, D. Ren, J. Chen, X. Shi, L. Chen, High efficiency Bi2Te3-based materials and devices for thermoelectric power generation between 100 and 300 °C. *Energy Environ. Sci.* **9**, 3120-3127 (2016).

[15] O. Bubnova, X. Crispin, Towards polymer-based organic thermoelectric generators. *Energy Environ. Sci.* **5**, 9345-9362 (2012).

[16] J. He, T. M. Tritt, Advances in thermoelectric materials research: Looking back and moving forward. *Science* **357**, eaak9997 (2017).

[17] J. L. Blackburn, S. D. Kang, M. J. Roos, B. Norton-Baker, E. M. Miller, A. J. Ferguson, Intrinsic and Extrinsically Limited Thermoelectric Transport within Semiconducting Single-Walled Carbon Nanotube Networks. *Adv. Electron. Mater.* **5**, 1800910 (2019).

[18] J. L. Blackburn, A. J. Ferguson, C. Cho, J. C. Grunlan, Carbon-Nanotube-Based Thermoelectric Materials and Devices. *Adv. Mater.* **30**, 1704386 (2018).

[19] Q. Hu, Z. Lu, Y. Wang, J. Wang, H. Wang, Z. Wu, G. Lu, H.-L. Zhang, C. Yu, Double doping approach for unusually stable and large n-type thermoelectric voltage from p-type multi-walled carbon nanotube mats. *J. Mater. Chem. A* **8**, 13095-13105 (2020).

[20] O. Bubnova, Z. U. Khan, A. Malti, S. Braun, M. Fahlman, M. Berggren, X. Crispin, Optimization of the thermoelectric figure of merit in the conducting polymer poly(3,4-ethylenedioxythiophene). *Nat. Mater.* **10**, 429-433 (2011).

[21] L. Yang, M. P. Gordon, A. K. Menon, A. Bruefach, K. Haas, M. C. Scott, R. S. Prasher, J. J. Urban, Decoupling electron and phonon transport in single-nanowire hybrid materials for high-performance thermoelectrics. *Sci. Adv.* **7**, eabe6000 (2021).

[22] D. Kim, Y. Park, D. Ju, G. Lee, W. Kwon, K. Cho, Energy-Filtered Acceleration of Charge-Carrier Transport in Organic Thermoelectric Nanocomposites. *Chem. Mater.* **33**, 4853-4862 (2021).

[23] S. Lee, S. Kim, A. Pathak, A. Tripathi, T. Qiao, Y. Lee, H. Lee, H. Y. Woo, Recent Progress in Organic Thermoelectric Materials and Devices. *Macromol. Res.* **28**, 531-552 (2020).

[24] B. Russ, A. Glaudell, J. J. Urban, M. L. Chabinyc, R. A. Segalman, Organic thermoelectric materials for energy harvesting and temperature control. *Nat. Rev. Mater.* **1**, 16050 (2016).

[25] D. Huang, H. Yao, Y. Cui, Y. Zou, F. Zhang, C. Wang, H. Shen, W. Jin, J. Zhu, Y. Diao, W. Xu, C.-a. Di, D. Zhu, Conjugated-Backbone Effect of Organic Small Molecules for n-Type Thermoelectric Materials with ZT over 0.2. *J. Am. Chem. Soc.* **139**, 13013-13023 (2017).

[26] X. Guo, A. Facchetti, The journey of conducting polymers from discovery to application. *Nat. Mater.* **19**, 922-928 (2020).

[27] S. Wang, G. Zuo, J. Kim, H. Sirringhaus, Progress of Conjugated Polymers as Emerging Thermoelectric Materials. *Prog. Polym. Sci.* **129**, 101548 (2022).

[28] N. Massonnet, A. Carella, O. Jaudouin, P. Rannou, G. Laval, C. Celle, J.-P. Simonato, Improvement of the Seebeck coefficient of PEDOT:PSS by chemical reduction combined with a novel method for its transfer using free-standing thin films. *J. Mater. Chem. C* **2**, 1278-1283 (2014).

[29] T.-C. Tsai, H.-C. Chang, C.-H. Chen, Y.-C. Huang, W.-T. Whang, A facile dedoping approach for effectively tuning thermoelectricity and acidity of PEDOT:PSS films. *Org. Electron.* **15**, 641-645 (2014).

[30] H. Shi, C. Liu, Q. Jiang, J. Xu, Effective Approaches to Improve the Electrical Conductivity of PEDOT:PSS: A Review. *Adv. Electron. Mater.* **1**, 1500017 (2015).

[31] E. Yang, J. Kim, B. J. Jung, J. Kwak, Enhanced thermoelectric properties of sorbitol-mixed PEDOT:PSS thin films by chemical reduction. *J. Mater. Sci. Mater. Electron.* **26**, 2838-2843 (2015).

[32] M. N. Gueye, A. Carella, N. Massonnet, E. Yvenou, S. Brenet, J. Faure-Vincent, S. Pouget, F. Rieutord, H. Okuno, A. Benayad, R. Demadrille, J.-P. Simonato, Structure and Dopant Engineering in PEDOT Thin Films: Practical

Tools for a Dramatic Conductivity Enhancement. *Chem. Mater.* **28**, 3462-3468 (2016).

[33] Z. Fan, P. Li, D. Du, J. Ouyang, Significantly Enhanced Thermoelectric Properties of PEDOT:PSS Films through Sequential Post-Treatments with Common Acids and Bases. *Adv. Energy Mater.* **7**, 1602116 (2017).

[34] Y. Honma, K. Itoh, H. Masunaga, A. Fujiwara, T. Nishizaki, S. Iguchi, T. Sasaki, Mesoscopic 2D Charge Transport in Commonplace PEDOT:PSS Films. *Adv. Electron. Mater.* **4**, 1700490 (2018).

[35] Z. Li, H. Sun, C.-L. Hsiao, Y. Yao, Y. Xiao, M. Shahi, Y. Jin, A. Cruce, X. Liu, Y. Jiang, W. Meng, F. Qin, T. Ederth, S. Fabiano, W. M. Chen, X. Lu, J. Birch, J. W. Brill, Y. Zhou, X. Crispin, F. Zhang, A Free-Standing High-Output Power Density Thermoelectric Device Based on Structure-Ordered PEDOT:PSS. *Adv. Electron. Mater.* **4**, 1700496 (2018).

[36] N. Saxena, J. Keilhofer, A. K. Maurya, G. Fortunato, J. Overbeck, P. Müller-Buschbaum, Facile Optimization of Thermoelectric Properties in PEDOT:PSS Thin Films through Acido-Base and Redox Dedoping Using Readily Available Salts. *ACS Appl. Energy Mater.* **1**, 336-342 (2018).

[37] C. Wang, K. Sun, J. Fu, R. Chen, M. Li, Z. Zang, X. Liu, B. Li, H. Gong, J. Ouyang, Enhancement of Conductivity and Thermoelectric Property of PEDOT:PSS via Acid Doping and Single Post-Treatment for Flexible Power Generator. *Adv. Sustain. Syst.* **2**, 1800085 (2018).

[38] X. Wang, A. K. K. Kyaw, C. Yin, F. Wang, Q. Zhu, T. Tang, P. I. Yee, J. Xu, Enhancement of thermoelectric performance of PEDOT:PSS films by post-treatment with a superacid. *RSC Adv.* **8**, 18334-18340 (2018).

[39] X. Wang, X. Zhang, L. Sun, D. Lee, S. Lee, M. Wang, J. Zhao, Y. Shao-Horn, M. Dincă, T. Palacios, K. K. Gleason, High electrical conductivity and carrier mobility in oCVD PEDOT thin films by engineered crystallization and acid treatment. *Sci. Adv.* **4**, eaat5780 (2018).

[40] Z. Fan, J. Ouyang, Thermoelectric Properties of PEDOT:PSS. *Adv. Electron. Mater.* **5**, 1800769 (2019).

[41] T. A. Yemata, Y. Zheng, A. K. K. Kyaw, X. Wang, J. Song, W. S. Chin, J. Xu, Modulation of the doping level of PEDOT:PSS film by treatment with hydrazine to improve the Seebeck coefficient. *RSC Adv.* **10**, 1786-1792 (2020).

[42] E. Yvenou, M. Sandroni, A. Carella, M. N. Gueye, J. Faure-Vincent, S. Pouget, R. Demadrille, J.-P. Simonato, Spray-coated PEDOT:OTf films: thermoelectric properties and integration into a printed thermoelectric generator. *Mater. Chem. Front.* **4**, 2054-2063 (2020).

[43] J. H. Song, J. Park, S. H. Kim, J. Kwak, Vitamin C-Induced Enhanced Performance of PEDOT:PSS Thin Films for Eco-Friendly Transient Thermoelectrics. *ACS Appl. Mater. Interfaces* **15**, 2852-2860 (2023).

[44] O. Bubnova, Z. U. Khan, H. Wang, S. Braun, D. R. Evans, M. Fabretto, P. Hojati-Talemi, D. Dagnelund, J.-B. Arlin, Y. H. Geerts, S. Desbief, D. W. Breiby, J. W. Andreasen, R. Lazzaroni, W. M. Chen, I. Zozoulenko, M. Fahlman, P. J. Murphy, M. Berggren, X. Crispin, Semi-metallic polymers. *Nat. Mater.* **13**, 190-194 (2014).

[45] I. E. Jacobs, E. W. Aasen, J. L. Oliveira, T. N. Fonseca, J. D. Roehling, J. Li, G. Zhang, M. P. Augustine, M. Mascal, A. J. Moulé, Comparison of solution-mixed and sequentially processed P3HT:F4TCNQ films: effect of doping-induced aggregation on film morphology. *J. Mater. Chem. C* **4**, 3454-3466 (2016).

[46] E. Lim, K. A. Peterson, G. M. Su, M. L. Chabinyc, Thermoelectric Properties of Poly(3-hexylthiophene) (P3HT) Doped with 2,3,5,6-Tetrafluoro-7,7,8,8-tetracyanoquinodimethane (F4TCNQ) by Vapor-Phase Infiltration. *Chem. Mater.* **30**, 998-1010 (2018).

[47] E. H. Suh, J. G. Oh, J. Jung, S. H. Noh, T. S. Lee, J. Jang, Brønsted Acid Doping of P3HT with Largely Soluble Tris(pentafluorophenyl)borane for Highly Conductive and Stable Organic Thermoelectrics Via One-Step Solution Mixing. *Adv. Energy Mater.* **10**, 2002521 (2020).

[48] C. Chen, I. E. Jacobs, K. Kang, Y. Lin, C. Jellett, B. Kang, S. B. Lee, Y. Huang, M. BaloochQarai, R. Ghosh, M. Statz, W. Wood, X. Ren, D. Tjhe, Y. Sun, X. She, Y. Hu, L. Jiang, F. C. Spano, I. McCulloch, H. Sirringhaus, Observation of Weak Counterion Size Dependence of Thermoelectric Transport in Ion Exchange Doped Conducting Polymers Across a Wide Range of Conductivities. *Adv. Energy Mater.* **13**, 2202797 (2023).

[49] R. B. Aïch, N. Blouin, A. Bouchard, M. Leclerc, Electrical and Thermoelectric Properties of Poly(2,7-Carbazole) Derivatives. *Chem. Mater.* **21**, 751-757

(2009).

[50] I. H. Jung, C. T. Hong, U.-H. Lee, Y. H. Kang, K.-S. Jang, S. Y. Cho, High Thermoelectric Power Factor of a Diketopyrrolopyrrole-Based Low Bandgap Polymer via Finely Tuned Doping Engineering. *Sci. Rep.* **7**, 44704 (2017).

[51] S. Hwang, I. Jeong, J. Park, J.-K. Kim, H. Kim, T. Lee, J. Kwak, S. Chung, Enhanced Output Performance of All-Solution-Processed Organic Thermoelectrics: Spray Printing and Interface Engineering. *ACS Appl. Mater. Interfaces* **12**, 26250-26257 (2020).

[52] S. Xu, M. Hong, X. Shi, M. Li, Q. Sun, Q. Chen, M. Dargusch, J. Zou, Z.-G. Chen, Computation-guided design of high-performance flexible thermoelectric modules for sunlight-to-electricity conversion. *Energy Environ. Sci.* **13**, 3480-3488 (2020).

[53] J. Park, Y. Lee, M. Kim, Y. Kim, A. Tripathi, Y.-W. Kwon, J. Kwak, H. Y. Woo, Closely Packed Polypyrroles via Ionic Cross-Linking: Correlation of Molecular Structure–Morphology–Thermoelectric Properties. *ACS Appl. Mater. Interfaces* **12**, 1110-1119 (2020).

[54] H. M. Elmoughni, A. K. Menon, R. M. W. Wolfe, S. K. Yee, A Textile-Integrated Polymer Thermoelectric Generator for Body Heat Harvesting. *Adv. Mater. Technol.* **4**, 1800708 (2019).

[55] Y. Lee, J. Park, J. Son, H. Y. Woo, J. Kwak, Degenerately Doped Semi-Crystalline Polymers for High Performance Thermoelectrics. *Adv. Funct. Mater.* **31**, 2006900 (2021).

[56] H. J. Cheon, T. S. Lee, J. E. Lee, S. B. Kim, E. H. Suh, S.-K. Kwon, Y. J. Jeong, J. Jang, Y.-H. Kim, Design of Donor–Acceptor Polymer Semiconductors for Optimizing Combinations with Dopants to Maximize Thermoelectric Performance. *Chem. Mater.* **35**, 1796-1805 (2023).

[57] J. Lee, J. Kim, T. L. Nguyen, M. Kim, J. Park, Y. Lee, S. Hwang, Y.-W. Kwon, J. Kwak, H. Y. Woo, A Planar Cyclopentadithiophene–Benzothiadiazole-Based Copolymer with sp2-Hybridized Bis(alkylsulfanyl)methylene Substituents for Organic Thermoelectric Devices. *Macromolecules* **51**, 3360-3368 (2018).

[58] T. H. Kim, J. H. Kim, K. Kang, Molecular doping principles in organic electronics: fundamentals and recent progress. *Jpn. J. Appl. Phys.* **62**, SE0803

(2023).

[59] S. E. Yoon, Y. Kang, G. G. Jeon, D. Jeon, S. Y. Lee, S.-J. Ko, T. Kim, H. Seo, B.-G. Kim, J. H. Kim, Exploring Wholly Doped Conjugated Polymer Films Based on Hybrid Doping: Strategic Approach for Optimizing Electrical Conductivity and Related Thermoelectric Properties. *Adv. Funct. Mater.* **30**, 2004598 (2020).

[60] W. Xing, S. Wu, Y. Liang, Y. Sun, Y. Zou, L. Liu, W. Xu, D. Zhu, Engineering the Doping Efficiency in Pentacene Thin Films for High Thermoelectric Performance. *ACS Appl. Mater. Interfaces* **12**, 29540-29548 (2020).

[61] R. Noriega, J. Rivnay, K. Vandewal, F. P. V. Koch, N. Stingelin, P. Smith, M. F. Toney, A. Salleo, A general relationship between disorder, aggregation and charge transport in conjugated polymers. *Nat. Mater.* **12**, 1038-1044 (2013).

[62] K. A. Peterson, E. M. Thomas, M. L. Chabinyc, Thermoelectric Properties of Semiconducting Polymers. *Annu. Rev. Mater. Res.* **50**, 551-574 (2020).

[63] E. Lim, A. M. Glaudell, R. Miller, M. L. Chabinyc, The Role of Ordering on the Thermoelectric Properties of Blends of Regioregular and Regiorandom Poly(3-hexylthiophene). *Adv. Electron. Mater.* **5**, 1800915 (2019).

[64] E. M. Thomas, B. C. Popere, H. Fang, M. L. Chabinyc, R. A. Segalman, Role of Disorder Induced by Doping on the Thermoelectric Properties of Semiconducting Polymers. *Chem. Mater.* **30**, 2965-2972 (2018).

[65] S. N. Patel, A. M. Glaudell, K. A. Peterson, E. M. Thomas, K. A. O'Hara, E. Lim, M. L. Chabinyc, Morphology controls the thermoelectric power factor of a doped semiconducting polymer. *Sci. Adv.* **3**, e1700434 (2017).

[66] S. N. Patel, A. M. Glaudell, D. Kiefer, M. L. Chabinyc, Increasing the Thermoelectric Power Factor of a Semiconducting Polymer by Doping from the Vapor Phase. *ACS Macro Lett.* **5**, 268-272 (2016).

[67] C.-K. Mai, T. Arai, X. Liu, S. L. Fronk, G. M. Su, R. A. Segalman, M. L. Chabinyc, G. C. Bazan, Electrical properties of doped conjugated polyelectrolytes with modulated density of the ionic functionalities. *Chem. Commun.* **51**, 17607-17610 (2015).

[68] A. M. Glaudell, J. E. Cochran, S. N. Patel, M. L. Chabinyc, Impact of the Doping Method on Conductivity and Thermopower in Semiconducting Polythiophenes. *Adv. Energy Mater.* **5**, 1401072 (2015).

[69] K. Kang, S. Schott, D. Venkateshvaran, K. Broch, G. Schweicher, D. Harkin, C. Jellett, C. B. Nielsen, I. McCulloch, H. Sirringhaus, Investigation of the thermoelectric response in conducting polymers doped by solid-state diffusion. *Mater. Today Phys.* **8**, 112-122 (2019).

[70] K. Kang, S. Watanabe, K. Broch, A. Sepe, A. Brown, I. Nasrallah, M. Nikolka, Z. Fei, M. Heeney, D. Matsumoto, K. Marumoto, H. Tanaka, S.-i. Kuroda, H. Sirringhaus, 2D coherent charge transport in highly ordered conducting polymers doped by solid state diffusion. *Nat. Mater.* **15**, 896-902 (2016).

[71] Y. Yamashita, J. Tsurumi, M. Ohno, R. Fujimoto, S. Kumagai, T. Kurosawa, T. Okamoto, J. Takeya, S. Watanabe, Efficient molecular doping of polymeric semiconductors driven by anion exchange. *Nature* **572**, 634-638 (2019).

[72] D. Kiefer, R. Kroon, A. I. Hofmann, H. Sun, X. Liu, A. Giovannitti, D. Stegerer, A. Cano, J. Hynynen, L. Yu, Y. Zhang, D. Nai, T. F. Harrelson, M. Sommer, A. J. Moulé, M. Kemerink, S. R. Marder, I. McCulloch, M. Fahlman, S. Fabiano, C. Müller, Double doping of conjugated polymers with monomer molecular dopants. *Nat. Mater.* **18**, 149-155 (2019).

[73] R. S. Klein, Investigation of the Hall effect in impurity-hopping conduction. *Phys. Rev. B* **31**, 2014-2021 (1985).

[74] S. A. Gregory, R. Hanus, A. Atassi, J. M. Rinehart, J. P. Wooding, A. K. Menon, M. D. Losego, G. J. Snyder, S. K. Yee, Quantifying charge carrier localization in chemically doped semiconducting polymers. *Nat. Mater.* **20**, 1414-1421 (2021).

[75] J. J. Urban, One model to rule them all. *Nat. Mater.* **16**, 157-159 (2017).

[76] S. D. Kang, G. J. Snyder, Charge-transport model for conducting polymers. *Nat. Mater.* **16**, 252-257 (2017).

[77] H. Abdalla, G. Zuo, M. Kemerink, Range and energetics of charge hopping in organic semiconductors. *Phys. Rev. B* **96**, 241202 (2017).

[78] H. Ito, H. Mada, K. Watanabe, H. Tanaka, T. Takenobu, Charge transport and thermoelectric conversion in solution-processed semicrystalline polymer films under electrochemical doping. *Commun. Phys.* **4**, 8 (2021).

[79] H. Tanaka, K. Kanahashi, N. Takekoshi, H. Mada, H. Ito, Y. Shimoi, H. Ohta, T. Takenobu, Thermoelectric properties of a semicrystalline polymer doped beyond the insulator-to-metal transition by electrolyte gating. *Sci. Adv.* **6**,

eaay8065 (2020).

[80] C. Choi, A. de Izarra, I. Han, W. Jeon, Y. Lansac, Y. H. Jang, Hard-Cation-Soft-Anion Ionic Liquids for PEDOT:PSS Treatment. *J. Phys. Chem. B* **126**, 1615-1624 (2022).

[81] S.-M. Kim, C.-H. Kim, Y. Kim, N. Kim, W.-J. Lee, E.-H. Lee, D. Kim, S. Park, K. Lee, J. Rivnay, M.-H. Yoon, Influence of PEDOT:PSS crystallinity and composition on electrochemical transistor performance and long-term stability. *Nat. Commun.* **9**, 3858 (2018).

[82] P. Kumar, E. W. Zaia, E. Yildirim, D. V. M. Repaka, S.-W. Yang, J. J. Urban, K. Hippalgaonkar, Polymer morphology and interfacial charge transfer dominate over energy-dependent scattering in organic-inorganic thermoelectrics. *Nat. Commun.* **9**, 5347 (2018).

[83] H. Fritzsche, A general expression for the thermoelectric power. *Solid State Commun.* **9**, 1813-1815 (1971).

[84] N. Kim, B. H. Lee, D. Choi, G. Kim, H. Kim, J.-R. Kim, J. Lee, Y. H. Kahng, K. Lee, Role of Interchain Coupling in the Metallic State of Conducting Polymers. *Phys. Rev. Lett.* **109**, 106405 (2012).

[85] S. D. Kang, M. Dylla, G. J. Snyder, Thermopower-conductivity relation for distinguishing transport mechanisms: Polaron hopping in CeO2 and band conduction in SrTiO3. *Phys. Rev. B* **97**, 235201 (2018).

[86] R. M. Hill, Variable-range hopping. *Phys. Status Solidi A* **34**, 601-613 (1976).

[87] P. Sheng, Fluctuation-induced tunneling conduction in disordered materials. *Phys. Rev. B* **21**, 2180-2195 (1980).

[88] A. B. Kaiser, Systematic Conductivity Behavior in Conducting Polymers: Effects of Heterogeneous Disorder. *Adv. Mater.* **13**, 927-941 (2001).

[89] H. Wang, C. Yu, Organic Thermoelectrics: Materials Preparation, Performance Optimization, and Device Integration. *Joule* **3**, 53-80 (2019).

[90] M. Bharti, A. Singh, S. Samanta, D. K. Aswal, Conductive polymers for thermoelectric power generation. *Prog. Mater. Sci.* **93**, 270-310 (2018).

[91] R. Kroon, D. A. Mengistie, D. Kiefer, J. Hynynen, J. D. Ryan, L. Yu, C. Müller, Thermoelectric plastics: from design to synthesis, processing and structure–property relationships. *Chem. Soc. Rev.* **45**, 6147-6164 (2016).

[92] D. Yuan, D. Huang, C. Zhang, Y. Zou, C.-a. Di, X. Zhu, D. Zhu, Efficient

Solution-Processed n-Type Small-Molecule Thermoelectric Materials Achieved by Precisely Regulating Energy Level of Organic Dopants. *ACS Appl. Mater. Interfaces* **9**, 28795-28801 (2017).

[93] E. H. Suh, Y. J. Jeong, J. G. Oh, K. Lee, J. Jung, Y. S. Kang, J. Jang, Doping of donor-acceptor polymers with long side chains via solution mixing for advancing thermoelectric properties. *Nano Energy* **58**, 585-595 (2019).

[94] A. Abutaha, P. Kumar, E. Yildirim, W. Shi, S.-W. Yang, G. Wu, K. Hippalgaonkar, Correlating charge and thermoelectric transport to paracrystallinity in conducting polymers. *Nat. Commun.* **11**, 1737 (2020).

[95] C. J. Boyle, M. Upadhyaya, P. Wang, L. A. Renna, M. Lu-Díaz, S. Pyo Jeong, N. Hight-Huf, L. Korugic-Karasz, M. D. Barnes, Z. Aksamija, D. Venkataraman, Tuning charge transport dynamics via clustering of doping in organic semiconductor thin films. *Nat. Commun.* **10**, 2827 (2019).

[96] T. L. Nguyen, H. Choi, S. J. Ko, M. A. Uddin, B. Walker, S. Yum, J. E. Jeong, M. H. Yun, T. J. Shin, S. Hwang, J. Y. Kim, H. Y. Woo, Semi-crystalline photovoltaic polymers with efficiency exceeding 9% in a ～300 nm thick conventional single-cell device. *Energy Environ. Sci.* **7**, 3040-3051 (2014).

[97] Y. Zou, D. Huang, Q. Meng, C.-a. Di, D. Zhu, Correlation between Seebeck coefficient and transport energy level in poly(3-hexylthiophene). *Org. Electron.* **56**, 125-128 (2018).

[98] Y. Pei, H. Wang, G. J. Snyder, Band Engineering of Thermoelectric Materials. *Adv. Mater.* **24**, 6125-6135 (2012).

[99] Z. Liang, Y. Zhang, M. Souri, X. Luo, Alex M. Boehm, R. Li, Y. Zhang, T. Wang, D.-Y. Kim, J. Mei, S. R. Marder, K. R. Graham, Influence of dopant size and electron affinity on the electrical conductivity and thermoelectric properties of a series of conjugated polymers. *J. Mater. Chem. A* **6**, 16495-16505 (2018).

[100] J. Ding, Z. Liu, W. Zhao, W. Jin, L. Xiang, Z. Wang, Y. Zeng, Y. Zou, F. Zhang, Y. Yi, Y. Diao, C. R. McNeill, C.-a. Di, D. Zhang, D. Zhu, Selenium-Substituted Diketopyrrolopyrrole Polymer for High-Performance p-Type Organic Thermoelectric Materials. *Angew. Chem. Int. Ed.* **58**, 18994-18999 (2019).

[101] J. Liu, Y. Shi, J. Dong, M. I. Nugraha, X. Qiu, M. Su, R. C. Chiechi, D. Baran,

G. Portale, X. Guo, L. J. A. Koster, Overcoming Coulomb Interaction Improves Free-Charge Generation and Thermoelectric Properties for n-Doped Conjugated Polymers. *ACS Energy Lett.* **4**, 1556-1564 (2019).

[102] P. Pingel, R. Schwarzl, D. Neher, Effect of molecular p-doping on hole density and mobility in poly(3-hexylthiophene). *Appl. Phys. Lett.* **100**, 143303 (2012).

[103] J. Liu, L. Qiu, R. Alessandri, X. Qiu, G. Portale, J. Dong, W. Talsma, G. Ye, A. A. Sengrian, P. C. T. Souza, M. A. Loi, R. C. Chiechi, S. J. Marrink, J. C. Hummelen, L. J. A. Koster, Enhancing Molecular n-Type Doping of Donor–Acceptor Copolymers by Tailoring Side Chains. *Adv. Mater.* **30**, 1704630 (2018).

[104] S. Lee, D. C. Paine, K. K. Gleason, Heavily Doped poly(3,4-ethylenedioxythiophene) Thin Films with High Carrier Mobility Deposited Using Oxidative CVD: Conductivity Stability and Carrier Transport. *Adv. Funct. Mater.* **24**, 7187-7196 (2014).

[105] B. Qin, W. He, L.-D. Zhao, Estimation of the potential performance in p-type SnSe crystals through evaluating weighted mobility and effective mass. *J. Materiomics* **6**, 671-676 (2020).

[106] G. J. Snyder, A. H. Snyder, M. Wood, R. Gurunathan, B. H. Snyder, C. Niu, Weighted Mobility. *Adv. Mater.* **32**, 2001537 (2020).

[107] M. Schwarze, C. Gaul, R. Scholz, F. Bussolotti, A. Hofacker, K. S. Schellhammer, B. Nell, B. D. Naab, Z. Bao, D. Spoltore, K. Vandewal, J. Widmer, S. Kera, N. Ueno, F. Ortmann, K. Leo, Molecular parameters responsible for thermally activated transport in doped organic semiconductors. *Nat. Mater.* **18**, 242-248 (2019).

[108] L. Qiu, J. Liu, R. Alessandri, X. Qiu, M. Koopmans, Remco W. A. Havenith, S. J. Marrink, R. C. Chiechi, L. J. Anton Koster, J. C. Hummelen, Enhancing doping efficiency by improving host-dopant miscibility for fullerene-based n-type thermoelectrics. *J. Mater. Chem. A* **5**, 21234-21241 (2017).

[109] Z. Bu, X. Zhang, B. Shan, J. Tang, H. Liu, Z. Chen, S. Lin, W. Li, Y. Pei, Realizing a 14% single-leg thermoelectric efficiency in GeTe alloys. *Sci. Adv.* **7**, eabf2738 (2021).

[110] S. Hong, Y. Gu, J. K. Seo, J. Wang, P. Liu, Y. S. Meng, S. Xu, R. Chen, Wearable thermoelectrics for personalized thermoregulation. *Sci. Adv.* **5**,

eaaw0536 (2019).

[111] K. Nan, S. D. Kang, K. Li, K. J. Yu, F. Zhu, J. Wang, A. C. Dunn, C. Zhou, Z. Xie, M. T. Agne, H. Wang, H. Luan, Y. Zhang, Y. Huang, G. J. Snyder, J. A. Rogers, Compliant and stretchable thermoelectric coils for energy harvesting in miniature flexible devices. *Sci. Adv.* **4**, eaau5849 (2018).

[112] N. Kim, H. Kang, J.-H. Lee, S. Kee, S. H. Lee, K. Lee, Highly Conductive All-Plastic Electrodes Fabricated Using a Novel Chemically Controlled Transfer-Printing Method. *Adv. Mater.* **27**, 2317-2323 (2015).

[113] Y. Xia, K. Sun, J. Ouyang, Solution-Processed Metallic Conducting Polymer Films as Transparent Electrode of Optoelectronic Devices. *Adv. Mater.* **24**, 2436-2440 (2012).

[114] N. Massonnet, A. Carella, A. de Geyer, J. Faure-Vincent, J.-P. Simonato, Metallic behaviour of acid doped highly conductive polymers. *Chem. Sci.* **6**, 412-417 (2015).

[115] L. Friedman, Hall conductivity of amorphous semiconductors in the random phase model. *J. Non. Cryst. Solids* **6**, 329-341 (1971).

[116] R. Fujimoto, S. Watanabe, Y. Yamashita, J. Tsurumi, H. Matsui, T. Kushida, C. Mitsui, H. T. Yi, V. Podzorov, J. Takeya, Control of molecular doping in conjugated polymers by thermal annealing. *Org. Electron.* **47**, 139-146 (2017).

[117] S. Hikami, A. I. Larkin, Y. Nagaoka, Spin-Orbit Interaction and Magnetoresistance in the Two Dimensional Random System. *Prog. Theor. Phys.* **63**, 707-710 (1980).

[118] A. Yildiz, M. Kasap, The temperature dependence of the inelastic scattering time in InGaN grown by MOVPE. *Low. Temp. Phys.* **36**, 320-324 (2010).

Publications

[1] Journal papers

1. **J. Park**†, Y. Lee†, M. Kim†, Y. Kim, A. Tripathi, Y.-W. K, J. Kwak, H. Y. Woo, "Closely Packed Polypyrroles via Ionic Cross-Linking: Correlation of Molecular Structure–Morphology–Thermoelectric Properties", *ACS Appl. Mater. Interfaces* **12**, 1110–1119 (2020).
2. S. Hwang, I. Jeong, **J. Park**, J. -K. Kim, H. Kim, T. Lee, J. Kwak, S. Chung, "Enhanced Output Performance of All-Solution-Processed Organic Thermoelectrics:Spray Printing and Interface Engineering", *ACS Appl. Mater. Interfaces* **12**, 26250–26257 (2020).
3. A. Tripathi, Y. Ko, M. Kim, Y. Lee, S. Lee, **J. Park**, Y. -W. Kwon, J. Kwak, H. Y. Woo, "Optimization of Thermoelectric Properties of Polymers by Incorporating Oligoethylene Glycol Side Chains and Sequential Solution Doping with Preannealing Treatment", *Macromolecules* **53**, 7063–7072 (2020).
4. Y. Lee†, **J. Park**†, J. Son, H. Y. Woo, J. Kwak, "Degenerately Doped Semi-Crystalline Polymers for High Performance Thermoelectrics", *Adv. Funct. Mater.* **31**, 2006900 (2021).
5. M. Lee, J. Yang, H. Lee, J. I. Kee, A. R. Koirala, **J. Park**, H. Jo, S. Kim, H. Park, J. Kwak, H. Yoo, W. Huh, and M. S. Kang, "Stoichiometric Doping of Highly Coupled $Cu_{2-x}S$ Nanocrystal Assemblies", *ACS Appl. Mater. Interfaces* **13**, 26330–26338 (2021).
6. J. H. Song, J. Park, S. H. Kim, and J. Kwak, "Vitamin C-Induced Enhanced Performance of PEDOT:PSS Thin films for Eco-Friendly Transient Thermoelectrics", *ACS Appl. Mater. Interfaces*, **15**, 2852-2860 (2023).
7. **J. Park**, Y. Ko, J. Jeong, J. H. Song, J. S. Park, J. Kwak, "Effects of Interfacial Area and Energetic Barrier on Thermoelectric Performance of PEDOT:PSS–

MXene Composite Films", *Mater. Res. Express*, (In press).

[2] International conferences

1. **J. Park**, Y. Lee, H. Y. Woo, J. Kwak, "Enhanced Thermoelectric Performance of $FeCl_3$ Doped Cyclopentadithiophene-Benzothiazole Based Copolymer Films", 2019 Materials Research Society Fall Meeting & Exhibit, Boston, USA (2019)
2. **J. Park**, Y. Lee, H. Y. Woo, J. Kwak, "Investigation of Thermoelectric Response in Semi-Crystalline Polymer Doped Beyond the Insulator to Metal Transition", The 48th World Polymer Congress (IUPAC-MACRO2020+), Seoul, Korea (2021)
3. **J. Park**, J. Jeong, J. H. Song, J.Kwak, "Effects of Microstructure on the Charge Transport and Thermoelectric Performance of the Polymer-inorganic Hybrid films", ICOT 2022, Kitakyushu, Japan, (2022).
4. **J. Park**, J. G. Jang, S. H. Kim, J. Kwak, "Effects of PEDOT:PSS Microstructure on the Charge Transport and Thermoelectric Properties", 2022 Materials Research Society Fall Meeting & Exhibit, Boston, USA (2022)

한글 초록

다양한 산업 및 에너지 전환 과정에서 발생하는 저등급 폐열을 활용하는 것은 환경 오염과 에너지 위기에 대한 우려가 커지고 있는 상황에서 중요한 과제가 되어왔다. 공액 고분자 기반 열전소자는 저급 폐열을 직접 전기로 변환하여 지속 가능하고 친환경적인 접근 방식을 제공함으로써 이 문제에 대한 유망한 해결책을 제시할 수 있다. 그러나 이러한 소재의 본질적인 구조적 및 에너지적 장애로 인해 제백 계수(α)와 전기 전도도(σ) 사이의 전력 법칙 관계 (power-law) 가 유도되어 열전 성능을 향상시키는 것은 여전히 어려운 과제로 남아 있다.

본 학위논문에서는 순차적 도핑 (doping) 을 통해 축퇴 (heavily) 도핑 된 반-결정성 고분자가 α와 σ 사이의 power-law를 극복하여 국부적 역률(PF) 최대값에 도달할 수 있음을 보여주었다. 첫째로, 두 종류의 전자 주개-전자 받개 유형(donor-acceptor) 반결정질 고분자 (semi-crystalline polymers)를 순차적 도핑 방법을 사용하여 도핑 하였고, 이를 통해 α가 σ에 반비례하는 이상적인 α-σ 관계를 나타내는 시스템을 구현하였다. 순차적 도핑 방법은 고도로 정렬된 미세 구조를 보존하거나 심지어 향상시키면서 폴리머의 전자 구조를 효과적으로 조절하는 것을 가능하게 하였고, 이론적 최대치에 근접한 PF를 달성하고 금속 거동을 관찰할 수 있도록 하였다. 또한, 구조-특성 관계를 면밀히 연구하여 고분자의 전자 구조가 비축퇴 (non-degenerate) 에서 축퇴 degenerate 상태로

전환되는 지점에서 필름의 *PF* 최대값이 나타난다는 사실을 밝혀내었다.

둘째로, 공액 고분자 중 열전 소재로서 가장 유망한 PEDOT:PSS 필름의 전자 구조를 순차적 산-염기 처리를 도입하여 고도로 정렬된 미세구조를 유지하면서 성공적으로 조절하였다. 이 방법은 제백 계수 α와 전기 전도도 σ 간의 역관계 (inverse relation)을 동반한 열전 성능이 우수한 용액 공정 가능한 열전 소자를 제작할 수 있게 해주었고, 534.5 μW m^{-1} K^{-2}에 달하는 높은 *PF*를 얻는 것을 가능하게 하였다. 제작된 필름으로부터 Hall 효과, σ의 온도 음존효과 ($d\sigma/dT < 0$) 및 약한 국부화 (weak localization)와 같은 일관된 (coherent) 전하 전달 특성을 관찰할 수 있었다. 더 나아가, 다양한 기법을 활용한 구조-특성 관계에 대한 종합적인 분석을 통해, 도핑제에 의해 유도된 형태 변화 (conformational disorder)를 완화함으로써 *PF*를 더욱 개선할 수 있음을 입증하였다.

이 논문에서 사용된 혁신적인 방법론은 고성능 열전 소자 개발을 촉진하고 공액 고분자의 복잡한 구조-특성 관계에 대한 이해를 깊게 하는데 견고한 기반이 될 것이며, 저등급 폐열을 효과적으로 활용할 수 있는 대안을 제시함으로써 에너지 절약과 환경 문제에 대한 우려를 줄여서, 궁극적으로 산업과 사회를 더욱 녹색적이고 지속 가능한 미래로 이끌어 갈 것이라고 생각된다.

주요어: 저등급 폐열, 고분자 열전, 구조-특성 관계, 전하 수송, 무질서

학번: 2019-37962

감사의 글

2019년, 박사 과정을 시작했을 때부터 지금까지, 4년이라는 긴 시간이 흘렀습니다. 이제 저는 졸업을 앞두고 있고, 박사학위 취득을 지원해 주신 모든 분들께 감사의 말씀을 전하고자 합니다.

먼저, 학부 연구생 시절부터 저를 지도해주신 곽정훈 교수님께 진심으로 감사드립니다. 교수님께서는 학부 연구생으로 저를 받아주시고, 학문의 길을 열어주시면서 저의 연구가 어려운 고비를 맞았을 때 함께 그 어려움을 해결하는 동반자로 저를 지원해주셨습니다. 그 덕분에 저는 연구의 방향성을 잡고 이를 구체화하는데 도움을 받았고, 연구 외적으로도 많은 조언을 해주셔서 정신적으로 큰 성장을 이룰 수 있었습니다. 또한, 학위심사 과정에서 저에게 귀중한 조언을 해주신 홍용택 교수님, 이수연 교수님, 강기훈 교수님, 정승준 박사님께도 감사의 인사를 드립니다. 교수님들의 조언 덕분에 박사 과정을 성공적으로 마칠 수 있었습니다.

이어서, 대학원 기간 동안 저와 함께 연구의 길을 걸어온 연구실 동료, 선배님들, 그리고 후배님들에게 감사드립니다. 여러분의 도움으로 4년 동안의 대학원 생활에 빠르게 적응하고 어려운 시기를 극복하며 언제나 즐거운 마음으로 연구를 수행할 수 있었습니다. AONE 연구실 구성원들 모두가 성공적인 결과를 이룰 수 있기를 바라며, 졸업 후에도 좋은 관계가 계속 될 수 있기를 희망합니다.

마지막으로, 항상 저를 응원하고 지지해주신 사랑하는 가족, 아

버지, 어머니, 그리고 형에게 감사드립니다. 여러분의 지지와 응원이 저의 가장 큰 버팀목이었습니다. 항상 더 나은 아들이 되기 위해서 최선을 다하겠습니다.

이제 졸업을 앞두고 있는 저에게는 새로운 시작점이 주어졌습니다. 이 기회를 바탕으로 더 깊은 연구와 지식을 탐구하며, 그 동안 배운 것들을 바탕으로 더 나은 연구자로 성장하겠습니다. 앞으로의 도전과 기회에 대한 열정을 잃지 않고 계속해서 발전해 나가겠습니다.